

# Wavelength selective devices in silicon-on-insulator and silicon nitride

*Bruno Taglietti*



Department of Electrical & Computer Engineering

McGill University, Montreal

April 2023

---

A thesis submitted to McGill University in partial fulfillment of the requirements of the  
degree of Doctor of Philosophy.

©Bruno Taglietti 2022

# Abstract

Wavelength-selective photonic devices are important in several fields. Moreover, fabrication variations are often responsible for the decreased experimental performance of photonic devices compared to simulations, and identifying the ones that have the most impact can help us build better photonic devices. Subwavelength Grating (SWG) structures offer versatility and flexibility, such as in controlling dispersion and birefringence. Therefore, this thesis focuses on (1) using SWGs/metamaterials for developing waveguide devices, including Bragg Gratings (BGs) and a Wavelength Division Multiplexing (WDM) diplexer, and (2) characterizing BGs in order to understand more about the fabrication variations imposed in the structures.

Silicon Nitride (SiN) is particularly and inherently prone to fabrication variations which can significantly impact the characterized response of devices. We have included in the Transfer-Matrix Method (TMM) simulation model several of these variations, such as waveguide sidewall angle, cross-section dimension variations, and longitudinal shrinkage, and analyzed their likelihood. The variations that best fit the results go against the expectation of material shrinkage of SiN, suggesting possible inaccuracy in the refractive index curve. The inclusion of longitudinal shrinkage as a simulation parameter can help to accurately simulate the bandwidth by modulating the grating strength. The characterized reflection curves show higher bandwidth for the Transverse Magnetic (TM) mode than Transverse Electric (TE),

which our modified simulation model could not reproduce. This suggests that the fabrication variations make the geometry of the actual fabricated structures deviate more from the ideal designed structure, resulting in a greater difference between the simulated and measured responses.

Another type of structure we have designed is the Sampled SWG-Waveguide Bragg Grating (WBG) in both uniform and random versions. The uniform sampled SWG-WBG shows three reflection bands, and their wavelength spacing shows very good accuracy between simulation and characterization. The device can be used for spectral slicing of broadband sources and for building multi-wavelength lasers. The feasibility of random WBG using SWG is also demonstrated. We have compared the simulated results without any randomizations, including them (evidencing its impact), and between measured responses of several fabricated devices. The correlation between characterized reflection curves of different versions of the device can be as low as 27%, suggesting effective randomization.

We have also designed an SWG-based WDM diplexer for the 1310 nm and 1550 nm channels. Our device shows a measured extinction ratio of more than 20 dB for both ports and a good wavelength range of operation. We were able to mitigate fabrication variations by varying design parameters. The device shows a comparable footprint and performance with the state-of-the-art, and the use of SWG waveguides as a building block may offer increased flexibility in future versions.

These devices can find several applications in areas such as optical communications and Microwave Photonics (MWP). They also illustrate the versatility and flexibility provided by SWG structures. Innovative approaches using SWG structures can stem from our development, and our fabrication variation analyses can also be used for problem mitigation in future devices.

# Abrégée

Les dispositifs photoniques sélectifs en longueur d'onde sont importants dans plusieurs domaines. De plus, les variations de fabrication sont souvent responsables de la diminution des performances expérimentales des dispositifs photoniques par rapport aux simulations, et l'identification de celles qui ont le plus d'impact peut nous aider à construire de meilleurs dispositifs photoniques. Les structures de réseaux sub-longueur d'onde (SWG) offrent une polyvalence et flexibilité, notamment pour le contrôle de la dispersion et de la biréfringence. Par conséquent, cette thèse se concentre sur (1) l'utilisation de SWGs/métamatériaux pour développer des dispositifs de guides d'ondes, y compris des réseaux de Bragg (BGs) et un diplexeur de multiplexage par répartition en longueur d'onde (WDM), et (2) la caractérisation des BGs afin de mieux comprendre les variations de fabrication imposées dans les dispositifs de guide d'onde.

Le nitrure de silicium (SiN) est particulièrement et intrinsèquement sujet à des variations de fabrication qui peuvent avoir un impact significatif sur la réponse caractérisée des dispositifs. Nous avons inclus dans le modèle de simulation de la méthode Transfer-Matrix (TMM) plusieurs de ces variations, telles que l'angle de la paroi latérale du guide d'ondes, les variations des dimensions de la section transversale et le retrait longitudinal, et nous avons analysé leur probabilité. Les variations qui s'adaptent le mieux aux résultats vont à l'encontre de l'attente du retrait du matériau Silicon Nitride (SiN), suggérant une possible

imprécision de la courbe d'indice de réfraction. L'inclusion du retrait longitudinal comme paramètre de simulation peut aider à simuler avec précision la bande passante en modulant la force du réseau. Les courbes de réflexion caractérisées montrent une largeur de bande plus élevée pour le mode Transverse Magnetic (TM) que Transverse Electric (TE), ce que notre modèle de simulation modifié n'a pas pu reproduire. Cela suggère que les variations de fabrication font que la géométrie des structures réellement fabriquées s'écarte davantage de la structure idéale conçue, ce qui entraîne une plus grande différence entre les réponses simulées et mesurées.

Un autre type de structure que nous avons conçu est le SWG-réseau de Bragg à guide d'ondes (WBG) échantillonné, en versions uniforme et aléatoire. Le Subwavelength Grating (SWG)-Waveguide Bragg Grating (WBG) échantillonné uniforme présente trois bandes de réflexion, et leur espacement en longueur d'onde montre une très bonne précision entre la simulation et la caractérisation. Ce dispositif peut être utilisé pour le découpage spectral de sources à large bande et pour la construction de lasers à longueurs d'onde multiples. La faisabilité d'un WBG aléatoire utilisant un SWG est également démontrée. Nous avons comparé les résultats simulés sans aucune randomisation, en les incluant (mettant en évidence son impact), et entre les réponses mesurées de plusieurs dispositifs fabriqués. La corrélation entre les courbes de réflexion caractérisées de différentes versions du dispositif peut être aussi faible que 27%, ce qui suggère une randomisation efficace.

Nous avons également conçu un diplexeur SWG basé sur un Wavelength Division Multiplexing (WDM) pour les canaux 1310 nm et 1550 nm. Notre dispositif présente un rapport d'extinction mesuré de plus de 20 dB pour les deux ports et une bonne gamme de longueurs d'onde de fonctionnement. Nous avons pu atténuer les variations de fabrication en faisant varier les paramètres de conception. Le dispositif présente un encombrement et des performances comparables à ceux de l'état de l'art, et l'utilisation de guides d'ondes SWG comme

bloc de construction pourrait offrir une flexibilité accrue dans les versions futures.

Ces dispositifs peuvent trouver plusieurs applications dans des domaines tels que les communications optiques et la Photonique par micro-ondes (MWP). Ils illustrent également la polyvalence et la flexibilité offertes par les structures SWG. Des approches innovantes utilisant des structures SWG peuvent découler de notre développement, et nos analyses des variations de fabrication peuvent également être utilisées pour atténuer les problèmes dans les dispositifs futurs.

# Acknowledgements

First and foremost, I would like to express my deepest gratitude to my supervisor, Lawrence R. Chen. The relationship between a Ph.D. student and a supervisor is a strong and years-long commitment. Doing so while also coming from a faraway country can be a gamble. Mine hit a jackpot. Lawrence's professionalism, charisma, and ability to give truly constructive criticism and didactic lessons have earned not only my appreciation but my deepest admiration. I am grateful to have had his mentorship, and that I could always count on his rigorous reviews and feedback. I would also like to thank all professors who have been part of my Ph.D. committee, professors David V. Plant, Fabrice Labeau, and Songrui Zhao. Their feedback in each milestone of my Ph.D. program was invaluable and provided me with confidence that I was on the right track. I also feel indebted to professor Victor Torres Company, from Chalmers University, and his student Zhichao Ye, who fabricated some of the devices reported in this thesis and also provided rich feedback in our analyses. I could not have undertaken this journey without the support of my former supervisor professor Evandro Conforti and co-supervisor Rafael Ferrari. I would also like to acknowledge CMC for providing tools and for subsidizing the fabrication of some of the devices reported in this thesis.

One of the richest experiences that I had during my Ph.D. was becoming a Teaching Assistant. I have to thank again my supervisor, Lawrence R. Chen, but also professor

Narges Armanfard for giving me so many opportunities for teaching experiences. Many thanks also to my TA colleagues, especially Nima and Sara, with whom I had the pleasure of collaborating more closely.

It has been an enormous privilege to be a part of such a renowned research group. It would have been more than enough to have the chance to share immense technical knowledge with such a competent and diverse set of colleagues. On top of that, they have been the most delightful people to spend time with. I have to especially thank Hao for his help with the experiments, simulations, and discussions, his collaboration made Chapter 4 possible. Zifei, for her patience, while instructing us on coupling light into the photonic chips. Dr. Reza Maram, for his help with the theoretical background and sharing his knowledge about the simulation tools. Mostafa, for his help with characterizations and our discussions. I would also like to express my gratitude for the pleasant time I have spent with other colleagues, Parisa, Dr. Xian Jin, Maria, Behnam, Daniel, Adrian, Ling, Yue, Xi, Joel, Sai, Yuxuan, Luyao, and Dr. Nitika Vaish. Colleagues from other research groups have also made a difference in my Ph.D. experience and I would like to express my gratitude, especially to Samiul, Maxime, Mohsen, Yannick, Eslam, and Kaveh. My former lab colleagues from Unicamp deserve my thanks for their support and friendship, Tiago and Rafael.

Coming to Canada to pursue a Ph.D. was a dream come true. This was only possible because of the support my family has provided me, and so I can only express my endless gratitude. I was given a healthy childhood in a small rural community, full of freedom, safety, friendships, and caring love, and later in life, the opportunity to pursue an engineering degree. These are immense privileges anywhere, but even more so in Brazil. I owe all of this to my family. I know the distance has caused a lot of sadness, especially for my mother, Leonor, and my father, Argemiro, but also for my brother Mauro and sister Sheila. However, all the achievements I have earned, and will, are as much theirs as they are mine.

Lastly, I would like to express my gratefulness to my wife Gio. She makes me a better person, and she has been the greatest support that made this possible. We have faced many challenges together and we have always had each other's back – from the most boring tasks, like proofreading code and manuscripts, to the scariest/most exciting goals, such as moving to another country together. Her love, care and support were essential to get through these difficult years, and so I am happy I get to share this accomplishment with her.

# Associated Publications

## Journal Articles

The original contributions of the research works presented in this thesis have resulted in the following journal articles.

1. H. Sun, **B. Taglietti**, Y. Wang, and L. R. Chen, "Integrated subwavelength grating waveguide Bragg gratings for microwave photonics," **invited** paper in *Journal of Lightwave Technology*, 40(20):6636-6649, 2022.
  - H. Sun: was responsible for writing, simulations, design, characterizations and analysis in sections II-IV, and VI. He was co-responsible for simulation and design in section V and editing the manuscript.
  - **B. Taglietti**: was responsible for design, simulations, characterizations, analysis, and writing of section V about sampled SWG-WBGs. Co-responsible for editing the manuscript.
  - Y. Wang: contributed with characterizations of devices in section III.
  - L. R. Chen: was responsible for the Introduction, co-writing, and editing of the manuscript.

2. **B. Taglietti**, and L. R. Chen, "WDM diplexer based on subwavelength gratings for 1310 nm and 1550 nm," submitted for publication.
  - **B. Taglietti**: was responsible for the design, simulation, characterization, and analysis of the devices, as well as writing and editing the manuscript.
  - L. R. Chen: was responsible for editing the manuscript.

## Conference Papers

The original contributions of the research works presented in this thesis have resulted in the following conference papers.

1. **B. Taglietti**, H. Sun, and L. R. Chen, "Sampled subwavelength grating waveguide Bragg grating structures," in *Advanced Photonics Congress (APC) 2022*, session ITh2B.7.
  - **B. Taglietti**: Was responsible for simulations, characterizations, and analysis of the devices, as well as writing and editing the manuscript.
  - H. Sun: Was responsible for laying out the devices, helping with simulations, and editing the manuscript.
  - L. R. Chen: was responsible for editing the manuscript.
2. **B. Taglietti**, H. Sun, S. Moosabhoy, and L. R. Chen, "Random subwavelength grating waveguide Bragg gratings," in *IEEE Photonics Conference (IPC) 2022*, session ME2.2.
  - **B. Taglietti**: was responsible for simulations, characterizations, and analysis of the devices, as well as writing and editing the manuscript.

- H. Sun: Was responsible for laying out the devices, helping with simulations, and editing the manuscript.
  - S. Moosabhoy: was responsible for calculating the correlation between the characterized reflection curves.
  - L. R. Chen: was responsible for editing the manuscript.
3. **B. Taglietti** and L. R. Chen, "Subwavelength grating waveguide-based 1310/1550 nm diplexer," in *IEEE Photonics Conference (IPC) 2022*, session ME2.4.
- **B. Taglietti**: was responsible for the design, simulation, characterization, and analysis of the devices, as well as writing and editing the manuscript.
  - L. R. Chen: was responsible for editing the manuscript.

## Original Contributions

In this thesis, three new photonic devices are presented. Namely, (1) an SWG-based sampled WBG, which is reported in Section V of the journal article 1 and the conference paper 1; (2) a random SWG-based WBG, which is reported in the conference paper 2; and (3) a SWG-based WDM Diplexer for the 1310 nm and 1550 nm channels, which is reported in the journal article 2 and conference paper 3.

Moreover, the fabrication variation analyses of all the devices presented in this thesis are original contributions that will help identify the types of variations that have the biggest impact on performance. This might also help to focus attention in the fabrication process on the most impactful types of variations.

---

# Contents

Abstract	ii
Abrégée	iv
Acknowledgements	vii
Acronyms	xxiii
<b>1 Introduction</b>	<b>1</b>
1.1 Silicon Photonics . . . . .	1
1.1.1 Microwave Photonics . . . . .	3
1.1.2 Computing . . . . .	3
1.1.3 Photonic Sensors . . . . .	4
1.2 Silicon Nitride . . . . .	5
1.2.1 Transparency Range . . . . .	6
1.2.2 Index Contrast . . . . .	6
1.2.3 Losses . . . . .	7
1.3 Other Integration Platforms . . . . .	9
1.3.1 Chalcogenide Glasses . . . . .	10

---

1.3.2	III-Vs . . . . .	10
1.3.3	Others . . . . .	11
1.4	Motivation . . . . .	11
1.4.1	Estimation of Fabrication Variation . . . . .	11
1.4.2	Control of Wavelength Response . . . . .	13
1.4.3	Control of Effective index . . . . .	16
1.5	Organization of this Thesis . . . . .	17
<b>2</b>	<b>Fundamental Background</b>	<b>18</b>
2.1	Waveguide Propagation . . . . .	19
2.1.1	Normalized Parameters . . . . .	22
2.1.2	Effective Index Method . . . . .	23
2.1.3	Width vs. Effective Index . . . . .	24
2.2	Bragg Gratings . . . . .	25
2.2.1	Transfer-Matrix Method . . . . .	27
2.2.2	Squared Profile . . . . .	28
2.2.3	Sinusoidal Profile . . . . .	29
2.2.4	Sampled Bragg Gratings . . . . .	32
2.3	Subwavelength Gratings . . . . .	33
2.3.1	Subwavelength Grating Waveguide Bragg Gratings . . . . .	37
2.4	Summary and Conclusion . . . . .	39
<b>3</b>	<b>Fabrication Variation Estimations for Silicon Nitride Bragg Gratings</b>	<b>40</b>
3.1	Introduction . . . . .	41
3.2	Characterization Setup . . . . .	42
3.3	Design . . . . .	43

---

3.4	Characterized Results . . . . .	45
3.5	Analysis . . . . .	45
3.5.1	Analysis Presumptions . . . . .	49
3.5.2	Simulated Results . . . . .	51
3.5.3	Bragg Wavelength . . . . .	55
3.5.4	Bandwidth . . . . .	60
3.6	Conclusion . . . . .	65
<b>4</b>	<b>Sampled Subwavelength Grating Waveguide Bragg Gratings</b>	<b>69</b>
4.1	Introduction . . . . .	69
4.2	Uniform Sampled SWG-WBG . . . . .	71
4.2.1	Design and Layout . . . . .	71
4.2.2	Design and Layout . . . . .	72
4.2.3	Results . . . . .	76
4.3	Random Sampled SWG-WBG . . . . .	81
4.3.1	Design and Layout . . . . .	81
4.3.2	Results . . . . .	83
4.4	Summary and Conclusion . . . . .	86
<b>5</b>	<b>Subwavelength Grating WDM Mux/Demux for 1310 nm and 1550 nm</b>	<b>88</b>
5.1	Introduction . . . . .	88
5.2	Layout and Design . . . . .	90
5.2.1	Design . . . . .	90
5.2.2	Tolerance Analysis . . . . .	96
5.2.3	Fabrication Variations . . . . .	98
5.3	Results . . . . .	100

---

5.3.1	Device with Simulated Optimized Parameters . . . . .	101
5.3.2	Footprint Focused Design . . . . .	104
5.4	Summary and Conclusion . . . . .	106
<b>6</b>	<b>Conclusion</b>	<b>109</b>
6.1	Summary . . . . .	109
6.1.1	SiN WBG Model Improvements . . . . .	110
6.1.2	Sampled Subwavelength Grating Waveguide Bragg Gratings . . . . .	111
6.1.3	SWG-Based WDM Diplexer for 1310 nm and 1550 nm . . . . .	112
6.2	Future Works . . . . .	113
6.2.1	Fabrication Variation Mitigation . . . . .	113
6.2.2	Sampled Subwavelength Grating Waveguide Bragg Gratings . . . . .	114
6.2.3	WDM Diplexer for 1310 nm and 1550 nm Channels . . . . .	114
	<b>References</b>	<b>117</b>
	<b>Appendix A Bragg Gratings TMM Simulations</b>	<b>139</b>
A.1	Measured Refractive Indexes . . . . .	139
A.2	Silicon Nitride Bragg Gratings Simulation Script . . . . .	140

# List of Figures

1.1	Standard design and fabrication workflow. . . . .	12
1.2	Two types of wavelength-controlling devices. . . . .	14
1.3	The Waveguide Bragg Grating. . . . .	15
2.1	Example of a slab waveguide. The direction of propagation is $z$ , the thickness $h$ is in the $x$ direction and the waveguide width is in the $y$ direction. . . . .	19
2.2	Solutions of the eigenvalue equations for a 1550 nm Transverse Electric (TE) polarized signal propagating in a 500 nm thick SiN slab waveguide in (a), and a Silicon (Si) slab waveguide of same size in (b). . . . .	21
2.3	Normalized parameters curves comparing Silicon waveguides to Silicon Nitride.	23
2.4	Cross-section of typical SiN and Silicon-on-Insulator (SOI) strip waveguides.	23
2.5	Effective index as a function of waveguide width in each material. . . . .	25
2.6	Principle of operation of the Bragg grating. Subfigure (a) shows the effective index change throughout the longitudinal position $z$ , while (b) shows the top view of the structure built in SOI with changing width from $w_1$ to $w_2$ , and $\Delta w = w_2 - w_1$ . $E_{\text{in}}$ is the input signal, $r$ is the reflected field and $t$ is the transmitted field. . . . .	26
2.7	Illustration of the Transfer-Matrix Method. . . . .	27

2.8	Top view of a WBG in which the sidewall corrugations have sinusoidal profile.	29
2.9	Simulation and design process of the Bragg grating. . . . .	32
2.10	The Sampled Bragg Grating. . . . .	33
2.11	Top view comparison between the solid core waveguide in (a) and the Sub-wavelength grating waveguide in (b). . . . .	34
2.12	Example of the $f$ - $ k_z $ spectrum of an SWG waveguide. . . . .	36
2.13	Effective index with varying width $w$ at different wavelength channels. . . . .	36
2.14	The effective index curve of the SWG-WBG in (a), and the layout using two pairs of loading segments in (b). . . . .	38
2.15	Effective index as a function of wavelength and gap distance of an SWG-based waveguide that uses loading segments, in which $w = 400$ nm, $\Lambda_{\text{SWG}} = 254$ nm, $a = 127$ nm, and $l_{\text{SWG}} = 127$ nm. . . . .	38
3.1	Experimental setup. . . . .	43
3.2	Reflection $R$ and transmission $T$ spectra of SiN Bragg gratings. . . . .	46
3.3	Characteristic shrinkage of deposited SiN. (A) shows the longitudinal shrinkage, and (B) and (C) show the transversal types of shrinkage over $w_1$ and $w_2$ , respectively. . . . .	47
3.4	Longitudinal shrink adaptations to the simulation model of the SiN WBG. . . . .	50
3.5	Iterative process of improving the Bragg Grating (BG) simulation model. . . . .	51
3.6	Comparison between simulation and characterization results in the reflection spectrum for both polarizations. . . . .	53
3.7	Power profiles of the SiN WBG from a top view perspective and cross-section for both polarization modes. . . . .	54
3.8	Profile comparison of simulated results. . . . .	55

3.9	Bragg wavelength $\lambda_B$ as function of corrugation depth $\Delta w$ . . . . .	56
3.10	Average Bragg wavelengths for TE and TM modes. . . . .	57
3.11	Bandwidth as a function of corrugation depth. . . . .	60
3.12	Effect of Duty-cycle on Bandwidth (BW). Captions show the amount of longitudinal shrinkage. . . . .	61
3.13	Bandwidth as a function of corrugation depth for different types of fabrication variations. . . . .	63
4.1	Layout and schematics of the device. . . . .	73
4.2	Order of results of the sampled SWG-WBGs. . . . .	74
4.3	Uniform SWG-WBG (no sampling). Total length $\approx 5\text{mm}$ . . . . .	77
4.4	Sampled SWG-BG with 10 sampling sections of $N_{BG} = 500$ and $N_{SWG} = 1000$ . The sampling duty cycle is 50%. . . . .	78
4.5	Sampled SWG-WBG with 10 sampling sections of $N_{BG} = 500$ and $N_{SWG} = 2000$ . The sampling duty cycle is 33%. . . . .	79
4.6	Comparison between simulated results with higher propagation losses and random variations to the loading segments position. Reflection curves are shown in (a) and Transmission curves are shown in (b). . . . .	80
4.7	Layout of the Random Sampled SWG-WBG. . . . .	81
4.8	Reflection curves. Row (a) shows results of simulated non-randomized structures; row (b) shows the simulated results of randomized structures, and row (c) shows the characterized results of two randomized fabricated structures in blue and orange. Column (1) structures have $\bar{D}_{\text{Sample}} = 99.8\%$ ; column (2) structures have $\bar{D}_{\text{Sample}} \approx 50\%$ ; and column (3) structures have $\bar{D}_{\text{Sample}} \approx 33\%$ . . . . .	84

5.1	The top-view of the full schematic of the device is shown in (a), the cross-section of the 220 nm thick waveguide is shown in (b), and the full device layout is shown in (c), including the VGCs. . . . .	91
5.2	Extinction ratio of both ports as a function of the coupler length $L_c$ . . . . .	93
5.3	Particle Swarm Optimization (PSO) algorithm flowchart. . . . .	95
5.4	Simulated power profile for 1310 nm in (a) and 1550 nm in (b) of Design 1. . . . .	96
5.5	Transmission as function of gap length $g$ and SWG segment length $a$ for each port and each channel. . . . .	97
5.6	Extinction ratio as function of gap length $g$ and SWG segment length $a$ for each port. . . . .	97
5.7	Insertion Loss as function of gap length $g$ and SWG segment length $a$ for each port/channel. . . . .	98
5.8	Simulated fabrication variations on the SWG segments. . . . .	99
5.9	Simulated relative transmission for the Cross port in red and the Bar port in blue, considering random SWG segment size reductions for Design 1. Solid line shows the ideal case, dashed for $\mathcal{U}(0, 1)$ , and dotted for $\mathcal{U}(0, 10)$ . . . . .	99
5.10	Simulated relative transmission for the Cross port in red and the Bar port in blue considering sidewall angles in the SWG segments. Solid line shows the ideal case ( $\alpha = 0^\circ$ ), dashed for $\alpha = 1^\circ$ , and dotted for $\alpha = 5^\circ$ . . . . .	100
5.11	Simulated relative transmission for the Cross port in red and the Bar port in blue are shown in (a) and the characterized relative transmission curves are shown in (b) and (c) for the O-band and C-band, respectively, with a vertical scale of 10 dB/div. $DC_{\text{SWG}} = 0.41$ . The vertical dashed lines indicate the characterization range, 1260 nm to 1330 nm and 1500 nm to 1584 nm in the O and C bands, respectively. . . . .	102

5.12	Simulated relative transmission for the Cross port in red and the Bar port in blue in (a) and characterized in the O-band in (b) and C-band in (c) for the device with a 10 nm increase in SWG segment length, <i>i.e.</i> , $DC_{\text{SWG}} = 0.46$ . . . . .	103
5.13	Simulated relative transmission for the Cross port in red and the Bar port in blue in (a) and characterized at the O-band in (b) and C-band in (c) for the device with a 20 nm increase in SWG segment length, <i>i.e.</i> , $DC_{\text{SWG}} = 0.51$ . . . . .	103
5.14	Simulated relative transmission for the Cross port in red and the Bar port in blue in (a) and characterized at the O-band in (b) and C-band in (c) for Design 5. . . . .	105
5.15	Transmission curves of the Cross port in red and Bar in blue for Design 5 with random SWG segments size variations. Solid line shows the ideal case, and dotted for $\mathcal{U}(0, 10)$ . . . . .	105
5.16	Sidewall angle impact on the transmission of the Cross port in red and Bar in blue for Design 5. Solid line shows the ideal case ( $\alpha = 0^\circ$ ), dashed for $\alpha = 1^\circ$ , and dotted for $\alpha = 5^\circ$ . . . . .	106

# List of Tables

1.1	Refractive index at 1550 nm of some of the materials used for photonic applications. . . . .	7
1.2	Kerr nonlinearity coefficient of the materials [1–3]. . . . .	9
3.1	Common parameters of the fabricated SiN WBGs. . . . .	44
4.1	Common parameters between all sampled SWG-WBG versions. . . . .	75
4.2	Common parameters between all random sampled SWG-WBG versions. . . . .	83
4.3	Correlation-matrix of the reflection curves. . . . .	85
5.1	Parameter values of the optimized WDM diplexers. . . . .	95
5.2	Experimental performance comparison with similar devices in the literature. . . . .	107
A.1	Wavelength samples of the refractive index curves used in the simulations of Chapter 3 obtained from ellipsometry measurements. . . . .	139

# Acronyms

**ADC** Asymmetric Directional Coupler.

**ANT** Applied Nanotools NanoSOI Fabrication Process.

**ASE** Amplified Stimulated Emission.

**BG** Bragg Grating.

**BOX** Buried Oxide.

**BW** Bandwidth.

**ChGs** Chalcogenide Glasses.

**CMOS** Complementary Metal-Oxide-Semiconductor.

**CMT** Coupled-Mode Theory.

**CVD** Chemical Vapor Deposition.

**CZT** Chirped Z-Transform.

**EO** Electrical-to-Optical.

**ER** Extinction Ratio.

**FBG** Fiber Bragg Grating.

**FDE** Finite Difference Eigenmode.

**FDTD** Finite-Difference Time-Domain.

**FOM** Figure of Merit.

**FP** Fabry P erot.

**FRA** Fibre Ribbon Array.

**IL** Insertion Loss.

**LASER** Light Amplification by Stimulated Emission of Radiation.

**LPCVD** Low-Pressure Chemical Vapor Deposition.

**MMI** Multimode Interferometer.

**MPW** Multi-Project Wafer.

**MRR** Microring Resonator.

**MWP** Microwave Photonics.

**MZI** Mach-Zehnder Interferometer.

**NIR** Near Infrared.

**OPC** Optical Polarization Controller.

**OSA** Optical Spectrum Analyser.

**PBS** Polarization Beam Splitter.

**PDK** Process Design Kit.

**PECVD** Plasma-Enhanced Chemical Vapor Deposition.

**PIC** Photonic Integrated Circuit.

**PSO** Particle Swarm Optimization.

**RF** Radio Frequency.

**SDC** Symmetric Directional Coupler.

**Si** Silicon.

**SiN** Silicon Nitride.

**SiNOI** Silicon Nitride on Insulator.

**SiP** Silicon Photonics.

**SiRN** Silicon Rich Nitride.

**SMF** Single-Mode Fibers.

**SOA** Semiconductor Optical Amplifier.

**SOI** Silicon-on-Insulator.

**SWG** Subwavelength Grating.

**TE** Transverse Electric.

**TM** Transverse Magnetic.

**TMM** Transfer-Matrix Method.

**TPA** Two-Photon Absorption.

**VGC** Vertical Grating Coupler.

**WBG** Waveguide Bragg Grating.

**WDM** Wavelength Division Multiplexing.

# Chapter 1

## Introduction

The field of optical communications has substantially evolved during the last 30 years and has become one of the fundamental core of telecom and datacom systems. The increase in numbers and complexity of optical devices in data centers has created a massive demand for integrated photonics, resulting in such a rapid technology development that it is commonly compared to the twentieth-century microelectronic revolution [4]. Both microelectronics and Silicon Photonics rely on the Complementary Metal-Oxide-Semiconductor (CMOS) fabrication process, meaning that the infrastructure and technology previously installed for fabricating microelectronic devices could also be used for fabricating photonic devices on the same silicon wafers. Integrated photonic devices have not only been an essential development in communications but have also lead to applications in several other fields.

### 1.1 Silicon Photonics

The field of Silicon Photonics (SiP) is relatively new, even though waveguiding in silicon and, thus, Photonic Integrated Circuits (PICs), has been proposed as far back as the '80s [5].

It could be argued that 2004 was the beginning of SiP as a field since not only ramping investments were witnessed but also the first international conference took place [6]. It is also one of the fastest adopted technologies in history [7].

Despite the fast adoption, there have been numerous challenges to overcome. Propagation losses in silicon waveguides were a huge issue in the early 90s, but in the year 1992 waveguides built in a 7  $\mu\text{m}$  thick layer of Silicon (Si) were demonstrated to have propagation losses as low as 0.3 dB/cm [8]. This solved the issue of propagation loss, but a 7  $\mu\text{m}$  thick layer of Si can only allow for multimode propagation, which is hard to control, and it would take a decade before sub-micron waveguides would be viable. There were many more problems that the SiP platform had to overcome, such as coupling light from microns-wide fibres to nanometers-wide waveguides maintaining single-mode propagation, achieving active devices on the Silicon-on-Insulator (SOI) platform, manipulating the effective index rapidly and efficiently, among many others. However, the adoption of the technology has given rise to a vast range of applications.

The field of optical communications was, perhaps, one of the most obvious applications of SiP since the adoption of fibre optics had taken place a few decades before, and the demand for integration remains strong. In the mid-to-late 2000s, several integrated GHz modulators were demonstrated [9,10], also integrated lasers and photodetectors in Si [11,12]. Nowadays, we have access to over 100 GHz integrated modulators [13]. This paved the way for more comprehensive integrated optical systems in the following decades. 5G already relies heavily on photonics for handling such high-frequency information [14–16], but as we start planning for 6G, SiP will become a fundamental building block of the technology [17,18].

Another important aspect of the rise of SiP as a field is the range of options for Multi-Project Wafer (MPW) runs. In the last few decades, there has been a significant effort in commercialization and an increase in accessibility to these fabrication platforms [19]. Today,

---

we can have access to foundries that offer not only SOI, but also other materials including Silicon Nitride (SiN) (such as at Applied Nanotools NanoSOI Fabrication Process (ANT)), and Silicon-Germanium, III-Vs, and others (such as at GlobalFoundries). The access to fabrication allows for more exploration in the field, which will hopefully lead to further innovation.

### 1.1.1 Microwave Photonics

Microwave Photonics (MWP) is often characterized as the use of optical devices to carry Radio Frequency (RF) information [20]. The key is that optical signals are inherently faster than electrical and have significantly higher Bandwidth (BW). The use of optical signals for generating microwave signals allows the realization of a whole range of functionalities that would be either very complex to achieve with electronics, or even impossible in some cases. On top of that, the integration of the photonic components offers a smaller footprint and weight, cost reduction, robustness and energy efficiency [21].

The fact that these systems are built in the CMOS platform allows for easy integration with the microelectronic devices. Among the applications of this technology, a few currently stand out, such as the generation of arbitrary waveforms [22], photonic array radars for radar imaging [23], and filtering. The works presented in this thesis might find applications in this field.

### 1.1.2 Computing

There is a growing expectation that the field of quantum computing will bring new capabilities functions and services that would be otherwise impossible to achieve with traditional digital computing. It has been claimed that a revolution has already taken place and we are now under a second quantum computing revolution [24]. In this scenario, the control of

photons would be a crucial building block and, thus, photonics would become fundamental for the field.

However, silicon photonics does not depend on the development of quantum computers to find the demand for research and development in traditional digital computers. Most of the power consumption in computers is not due to signal processing, but in fact, due to the transmission of information between units, like from the CPU to memory or GPU [6], where the signal power is converted to heat. Although the Electrical-to-Optical (EO) conversion brings up a whole set of other challenges, the decrease in power consumption is enough to make a huge difference in data centers, where the issue becomes scalable.

Moreover, because of the ever-growing demand for faster and more efficient signal processing and communication, it is a cause of concern that microelectronics are reaching the limits of Moore's law. One of the main reasons for the slowing down in that increase is the quantum tunnelling effect of transistor gates smaller than 7 nm. Creative solutions to this problem have been proposed, many of which are based on surrounding the gate in a 3D manner, which is known as Gate-all-around [25], but there is some expectation for a paradigm shift, which brings us to another potential new application of the SiP platform. All-optical signal processing could open up many possibilities for new technologies [26,27].

### 1.1.3 Photonic Sensors

Photonic sensors possess several attributes that make them a viable and attractive alternative to electronic sensors. These attributes include non-contact sensing, the capability to disperse photonic nanoparticles directly into the sensing medium [28], and the availability of multiple measurement modes. In environments where electronic sensors face limitations due to high temperature, physical vibration, or exposure to interfering electromagnetic fields such as ionizing radiation and UV, photonic sensors may offer a solution to these issues. Moreover,

the bandwidth brought by the optical nature of photonic devices offers high speed and high-resolution operation [29]. The use of wavelength-filtering structures in these sensors is commonplace, which will be one of the focuses of this thesis.

There are many principles of operation for sensors. One possible configuration uses dual-wavelength laser sources, where one wavelength carries the information and the other serves as a reference [29]. Laser absorption spectroscopy has been used for explosive detection [30]. One of the most common methods of photonic sensing is the evaluation of spectral shifts/changes in photonic devices. As examples, they have been used for sensing the concentration of blood hemoglobin and detecting cancer cells [31, 32].

There are many parameters that photonic devices can be designed to probe/sense. They include, but are not limited to, gyros [29], humidity [33], temperature [34], acoustic vibrations [35], and electromagnetic field [29]. Moreover, there is a growing demand for LIDARs [36], which have been accredited for making self-driving car positioning systems more affordable, where SOI phased arrays allow the control of the light propagation direction, instead of using delicate and expensive mechanical structures [37].

## 1.2 Silicon Nitride

Photonic applications for both stoichiometric SiN ( $\text{Si}_3\text{N}_4$ ) and non-stoichiometric ( $\text{Si}_x\text{N}_y$ ) have been reported for decades, as long back as 1977 [38], however, challenges had to be overcome before there was interest in the platform, like the occurrence of cracks in the film after deposition due to the tensile stress of the crystal structure. There are many proposed solutions to this problem, such as a very low-rate (2 nm/min) Low-Pressure Chemical Vapor Deposition (LPCVD) [39, 40].

Silicon Nitride can differ significantly from SOI as propagating material. It is pertinent

to list and contextualize some of the most important parameters and their differences [41].

### 1.2.1 Transparency Range

One important characteristic of a platform is the transparency range because, usually, each application is somewhat bound to a specific spectral window. For example, bio-photonic applications often use light between the visible spectrum and mid-near infrared, between 0.4  $\mu\text{m}$  and 1  $\mu\text{m}$ . Tele/datacom applications are usually in the Near Infrared (NIR) because of the low attenuation in Single-Mode Fibers (SMF) in that range. Sensing applications have a fairly wide range, from short NIR up to long mid-infrared, around 1  $\mu\text{m}$  up to around 10  $\mu\text{m}$ . Few semiconductor-based platforms have such a wide transparency range as the Silicon Nitrides, even though wavelengths longer than 4  $\mu\text{m}$  are usually absorbed by silicon dioxide that surrounds the SiN waveguides. For applications in such long wavelengths, a combination of germanium and Silicon have been proposed [42]. The wide transparency range is one of the reasons that make SiN an appealing choice as a propagating material. Compared to Silicon, this is a considerable gain in BW, which may provide ground for innovation.

### 1.2.2 Index Contrast

The refractive index of a given material is a very important parameter in photonic applications since it governs everything involving the propagation of light into the material. The refractive index curves of the pertinent materials can be seen in Table 1.1. These curves come from ellipsometric measurements we have received from Dr. Victor Torres Company's team at Chalmers University, except the Si curve, which comes from the Lumerical suite software. Appendix A.1 shows the measured refractive indexes at a few wavelength points for stoichiometric SiN, thermally grown and Chemical Vapor Deposition (CVD) deposited

silicon dioxides.

**Table 1.1** Refractive index at 1550 nm of some of the materials used for photonic applications.

Si	Si <sub>3</sub> N <sub>9</sub>	Si <sub>3</sub> N <sub>4</sub>	SiO <sub>2</sub> (CVD)	SiO <sub>2</sub> (Thermal)
3.5	2.07	1.99	1.46	1.44

SiN waveguides are typically used in strip configuration, *i.e.*, surrounded by silica with a rectangular cross-section. As Table 1.1 shows, the refractive index of SiN is drastically lower than that of the SOI platform, resulting in a lower index contrast. As a consequence, the devices are generally much less compact. On the other hand, this makes the platform more robust to small deviations of the design due to lithographic errors or unwanted waveguide sidewall corrugations. These fabrication deviations can cause significant spectral shifts in resonating devices in SOI, such as Microring Resonators (MRRs) and Mach-Zehnder Interferometers (MZIs), up to several nanometers. They can also make the production of balanced transmitters and receiver circuits very difficult and costly, sometimes requiring heat tuning. Therefore, the reduced vulnerability of SiN to random corrugations due to the lower index contrast can be of interest in many applications.

### 1.2.3 Losses

Usually, in silicon photonics, propagation losses are mostly due to the aforementioned unwanted corrugations on the sidewalls of the waveguides. Because of the huge index contrast of Silicon to Silicon dioxide, even sub-nanometer corrugations make up around 2 to 3 dB/cm of losses. This is manageable for single devices, but can seriously compromise the platform's integration capacity of larger cascaded systems without the introduction of active amplification, which can bring challenges, and problems, such as distortion and noise.

SiN has much lower losses than Si due to the lower index contrast. Stoichiometric SiN

show typical propagation losses between 0.1 dB/cm to 2.25 dB/cm [42], although losses as low as 0.001 dB/cm have been demonstrated in 40 nm thick waveguides, in a collaboration between LioniX and UCSB [43,44].

### Manufacturing Flexibility

Although there have been a few methods of depositing SiN on the silicon wafer through Plasma-Enhanced Chemical Vapor Deposition (PECVD) [45, 46], LPCVD have been preferred because of the lower temperature required for the deposition [47]. LPCVD requires 400°, while PECVD requires at least 700°. Higher temperatures are a concern in the fabrication process in the presence of doping materials, such as Phosphorus and Boron. The deposition temperature will further diffuse the doping material, which can compromise the fabrication process.

In this work, we only consider passive devices fabricated using a single 600 nm thick layer of stoichiometric SiN over the insulator, so higher temperature deposition methods are not a concern.

### Nonlinearity

Table 1.2 shows the Kerr nonlinearity coefficient  $n_2$  for Silicon, stoichiometric SiN ( $\text{Si}_3\text{N}_4$ ), and for Silicon Rich Nitride (SiRN) ( $\text{Si}_3\text{N}_9$ ). It seems counter-intuitive that nonlinearity is an important aspect of SiN when the Kerr coefficient is smaller than that of Silicon. The reason why Silicon Nitride on Insulator (SiNOI) is a promising platform for nonlinear applications is because of the absence of Two-Photon Absorption (TPA), which is a severe problem in Silicon within the C-band for telecommunications. TPA is a nonlinear loss proportional to  $|E|^2$ . That means that it is very pronounced in the case of high-power signals, which is necessary to produce nonlinear behaviour, crippling the effective length of the structures and, thus, the potential of nonlinear applications in Silicon. In SiN, the absence of TPA means it is possible to introduce very large power signals into the chip practically without any

nonlinear losses. Moreover, the lower propagation losses make it possible to build effective lengths comparable to the nonlinear length, whereas in the SOI platform that is not possible.

**Table 1.2** Kerr nonlinearity coefficient of the materials [1–3].

Material	Si	Si <sub>3</sub> N <sub>4</sub>	Si <sub>3</sub> N <sub>9</sub>
$n_2[\text{m}^2/\text{W}]$	$5 \times 10^{-18}$	$2.4 \times 10^{-19}$	$2.4 \times 10^{-18}$

There are ways to mitigate this issue in the SOI, such as employing strip-slot waveguides, which have a much higher Kerr nonlinearity coefficient, allowing for much shorter waveguides for nonlinear applications, but the trade-off is high propagation losses and specific fabrication requirements [48], and some of these techniques could also be applied in SiN to increase the Kerr nonlinearity.

### Thermal Robustness

The thermo-optical coefficient of SiN is significantly lower than Silicon's, which makes the devices very robust to thermal variations. Although thermo-optical modulation consumes more power and the thermal crosstalk is larger, thermal tuners are fairly established in the SiN platform [42].

## 1.3 Other Integration Platforms

There are still many challenges in SiP. Many of the platform characteristics impose difficulties on some applications. The comparison between different materials shows that there is still a need for further exploration and possible innovation.

One of the considerable concerns when evaluating the prospect of replacing a well-established platform, such as SOI, is that usually a significant investment had already been made on infrastructure, and tossing that aside is not efficient. Renewing and replacing equipment has a financial toll that has to be considered. When considering alternatives to the

SOI platform, retro-compatibility with the established infrastructure is fundamental.

There are many alternative platforms to SOI, and, naturally, each one of them compares differently. Among these are Indium Phosphide, Chalcogenide Glasses (ChGs), and SiN [42]. However, most MPW runs only offer limited options, and a Process Design Kit (PDK) that includes essential devices is not always provided.

### 1.3.1 Chalcogenide Glasses

ChGs are formed using VIa group elements of the periodic table. For example, elements such as sulphur, selenium, and tellurium form glasses using other nonmetals and metalloids, such as phosphorous, germanium and arsenic. They can be deposited onto the silicon wafer using thermal deposition, sputtering and CVD. They show very promising potential for their high photosensitivity and nonlinearity, and losses of 5 dB/m have been reported using  $\text{As}_2\text{S}_3$  [40,49]. Moreover, their large third-order nonlinear coefficient provides great potential for all-optical signal processing and might lead to a wider super-continuum than what is possible with other materials [50].

### 1.3.2 III–Vs

The materials in the III–V family, such as Indium Phosphide, are mostly responsible for active devices such as optical amplification and optical sources, *e.g.* the Semiconductor Optical Amplifier (SOA) and the Light Amplification by Stimulated Emission of Radiation (LASER), respectively. Therefore, the use of III–V materials has been responsible for the commercial success of integrated optical transceivers [51].

The transparency range of III–V materials is very similar to that of Silicon's, ranging within the NIR window. The deposition is often achieved by molecular or adhesive wafer bonding. The integration between the SOI platform and III–V materials usually requires a

hybrid approach, where each of them is separately fabricated and combined afterward [42].

### 1.3.3 Others

We have elaborated on the importance of a few prominent platforms in the photonics field, each with its strengths and weaknesses. These are not the only platforms for SiP. A few other noteworthy ones are thin film lithium niobate, which has shown great potential for optical modulators and nonlinear wavelength converters [52], and silica, which has long been used for optical fibres, and now find great integrated applications such as in arrayed-waveguide-gratings and lattice-form filters, due to their geometric precision [53], for example. However, this thesis will focus on SOI and SiN because these are the two platforms we have used in the applications detailed here.

## 1.4 Motivation

In this thesis, we have designed, characterized and analyzed waveguide devices that include Bragg gratings and a diplexer. We use the comparison between simulated results and measurements from the fabricated devices to better understand the fabrication variations, their possible causes and implications.

### 1.4.1 Estimation of Fabrication Variation

In a controlled environment, the effective index of a structure is primarily dependent on two aspects: (1) the refractive index of the propagating material, and (2) the physical dimensions of the waveguide.

During the fabrication process, many variations can occur to the structures before the process is finished. That includes rounding of the corners, the occurrence of random corru-

gations in the waveguide sidewalls, and variations in the sizes of the structures, among many other deviations from the original layout. Since the wavelength response of the device is most often dependent on the effective index, we can use the wavelength response to estimate the effective index.

Moreover, the accuracy of the simulated results depends both on the precision of the input parameters (such as the refractive indexes of the materials) and the geometrical similarity between fabricated and simulated devices. In the case of Waveguide Bragg Grating (WBG) built with SiN, some of the fabrication variations are not typically assumed in simulation, such as longitudinal shrinkage. However, it is possible to incorporate these variations into the Transfer-Matrix Method (TMM). The idea is to use the measured results of each fabrication run to improve the accuracy of simulated results in an iterative process. This is a standard design and fabrication workflow that is illustrated in Fig. 1.1 and will be one of the focuses of this thesis.

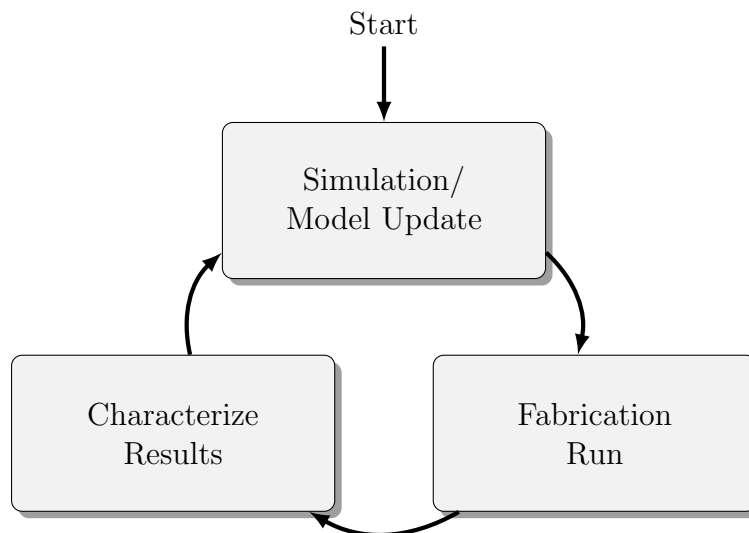


**Fig. 1.1** Standard design and fabrication workflow.

The statistical variation of the wavelength response of photonic devices, such as MRR,

due to fabrication variations has been studied [54–56]. What is proposed in this thesis, however, is the incorporation of plausible fabrication variations of SiN waveguides into the WBG simulation model. This is particularly important for the SiNOI platform since it is subject to not only random variations (which are also common to SOI) but also variations that are inherent to the SiN material. We follow a similar procedure in the case of the Subwavelength Grating (SWG)-based structures by anticipating expected fabrication variations and analyzing their impacts on the simulated results. This will help us to determine which of these variations are more likely and to design devices that are more robust in future fabrication runs.

#### 1.4.2 Control of Wavelength Response

The control of the wavelength response is one of the building blocks of SiP as a field. One of the pillars of the high-capacity telecommunication infrastructure is the reliance on Wavelength Division Multiplexing (WDM) to carry information in separate channels, which is built upon dividing the optical spectrum into wavelength channels. In this context, WDM multiplexers are a vital building block of the infrastructure, which can also take advantage of integration.

Wavelength-selective devices are undoubtedly important in WDM, however, they can find applications in many other fields. Often, photonic filters are used as part of a sensor interrogation system, for example. Wavelength-to-power mapping of photonic filters is often used to design the interrogation system of optical sensors.

In the passive SiP domain, there are several types of structures that can be used to control the amplitude and phase of the spectrum, such as the two shown in Fig. 1.2 – the MZI in (a) and the MRR in (b). Both devices rely on constructive and destructive interference due to phase mismatch. In the MZI, the mismatch is due to the length difference in each

path  $\Delta L = L_2 - L_1$ , where  $L_1$  is the length of the shorter branch and  $L_2$  is the length of the longer. In the MRR, part of the input signal  $E_{\text{in}}$  gets coupled into the ring and, if the critical coupling condition is met, constructive and destructive interference will create a wavelength-periodical response in the drop signal  $E_{\text{drop}}$  and the through signal  $E_{\text{through}}$  [57].

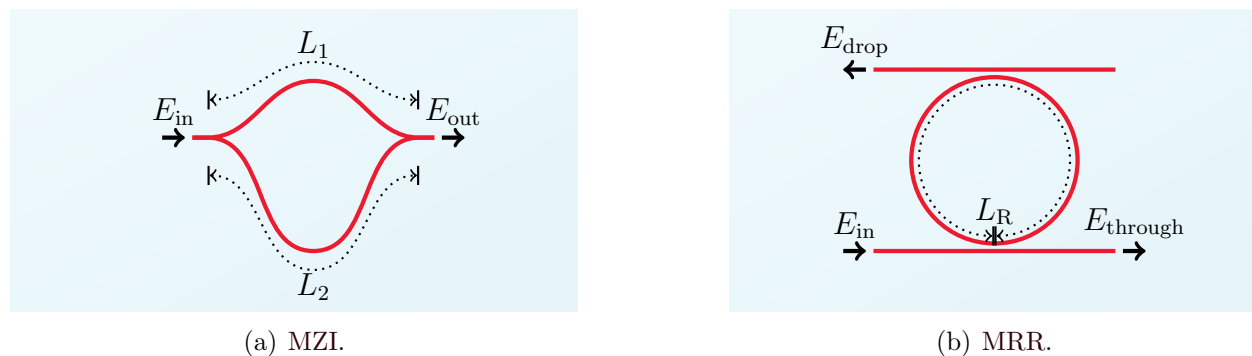


**Fig. 1.2** Two types of wavelength-controlling devices.

Another relevant device that allows us to control the wavelength response of photonic devices is the Bragg Grating (BG). It is a very useful device in integrated photonics because it does not rely on phase-related interference like the previously shown devices, which often require thermal tuning to compensate for any needed phase shift. Instead, it uses accumulated reflection that results from periodic effective index changes. The Fiber Bragg Grating (FBG) has long been used in several types of applications, such as in WDM systems, but a prominent application is in sensors.

The optical nature gives the devices an inherent advantage over electronic sensors because of fast response, distributed sensing, and immunity to electromagnetic fields [58]. The latter can be particularly important in environments subject to emission, such as in space, where background radiation is a problem, or in nuclear applications. Another important application that FBGs have been used is in medical sensing, both in surgical tools and biosensors [59].

However, the integration of the device offers more robustness and has a smaller footprint.

The WBG is illustrated in Fig. 1.3.

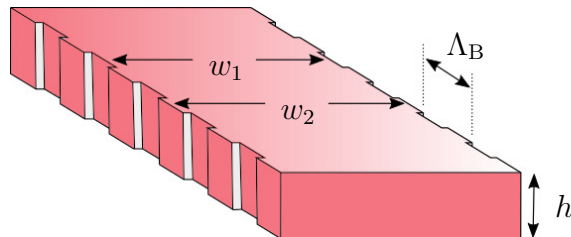


**Fig. 1.3** The Waveguide Bragg Grating.

Its wavelength response is not periodic. But it is possible to replicate the reflection band with a pre-determined wavelength spacing by sampling the gratings. Sampled-WBG have long been built and used for temperature sensors [60], mechanical torsion sensors [61], lasers [62], and other applications.

They have also been established in the SOI platform [63], however, we have designed and characterized them in SWG, which is novel. The usage of SWG allows us to explore a polarization-independent version of the device as future work.

One of the issues with integrated WBG is that the filtered wavelength is reflected and back-propagates from the same waveguide used as input. Circulators are still a challenge to build in the SiP platform, especially if the MPW run only offers access to commonly used materials, such as SOI and SiN structures, and not other more complex materials.

Another effective device that allows us to control the optical signal's path is the Directional Coupler, which can be symmetric, asymmetric, and bent. They can separate signals based on the wavelength channel since dispersion causes each channel to have a different effective index, but it also allows for the separation of different modes [64]. The clever use of modal separation can also allow the construction of WDM add-and-drop multiplexers [65].

### 1.4.3 Control of Effective index

The effective index is one of the most fundamental parameters in integrated photonics. It is safe to say that its accuracy during the design and simulation steps of development will determine whether the fabricated device will work accurately.

In terms of control of the effective index of waveguides in the SOI platform, we usually need to constrain the Si film thickness to the foundry standard in MPW runs – which is usually 220 nm, leaving us with only the width of the waveguides to control the effective index. This is a limitation in our control over signal behaviour. Using strip waveguides, it is reasonably simple to control the effective index of the fundamental mode, but not its relation to the other modes. For instance, by only changing the width of a 220 nm thick waveguide, it is challenging to build a single-mode waveguide that has a polarization-independent effective index. In other words, in a thickness-constrained SOI platform of 220 nm, it is very hard to get a waveguide with the same effective indexes for both Transverse Electric (TE) and Transverse Magnetic (TM) polarized propagation.

SWG is a type of waveguiding structure that uses periodic structures with a longitudinal period below the wavelength of the propagating signal that offers more parameters to control the behaviour of the signal than the typical strip waveguide. SWGs are a powerful tool to control not only the effective index of the fundamental propagating mode, but also its relation with other modes', dispersion, nonlinear coefficient [66], and group index, and it will also be a subject of exploration in this thesis.

Just as the typical solid core waveguides, the SWG is completely compatible with the CMOS and SOI platforms since it just requires the waveguides to be built with Si segments with a subwavelength periodicity. One of the keys for SWG fabrication-wise is that the feature size and spacing allowed in the lithography has to be smaller than the smallest

segments of the SWG structures.

Among the applications that the SWG technique has offered, very low-crosstalk waveguide crossings [67] have stood out since they can help reduce the footprint of photonic circuits significantly. The reduced effective index reduces how concentrated the propagating signal is inside the waveguide dimensions and allows for the low-loss and low-crosstalk crossing.

All of the additional control over the propagating signal behaviour provided by SWGs shows that this is a subject with potential for exploration. In this thesis, we have used SWG to build new devices, such as sampled WBGs and a WDM multiplexer with that intent.

## 1.5 Organization of this Thesis

Chapter 1 offered an introduction and a context to the subjects covered in this thesis. Chapter 2 offers a theoretical background for the upcoming chapters. Chapter 3 will show our simulation model improvements of SiN WBG taking into account the fabrication variations expected for the SiNOI platform. Chapter 4 will show the design, layout, and both simulated and measured results of sampled SWG-based WBGs in both uniform and random versions. In Chapter 5, we similarly present a SWG-based WDM diplexer for the 1310 nm and 1550 nm channels. Lastly, Chapter 6 offers discussions and conclusions about our findings and comments on future works.

## Chapter 2

# Fundamental Background

This chapter will start by establishing the theoretical background that governs signal propagation in optical waveguides. It will then introduce the TMM simulation method, which is often used for simulating BGs. Lastly, it will introduce the fundamental simulations of SWG waveguides.

The TMM simulation method that will be discussed provides a way of using the estimated effective index to compute the reflection and transmission curves of BGs without having to rely on Finite-Difference Time-Domain (FDTD) simulations. BGs structures tend to be physically longer than what is computationally wise viable for FDTD. For comparison, a full 3D FDTD simulation of a  $30 \times 100 \mu\text{m}^2$  device can take around 40 hours to run, depending on the mesh dimensions, accuracy, insertion and propagation losses. The SiN WBG that will be presented in Chapter 3 are almost 1 cm long, which is 100 times longer and have very low propagation losses. Thankfully, TMM allows for much more computationally efficient simulations of BGs. For more compact devices, such as the WDM diplexer of Chapter 5, we can rely on FDTD to compute the simulated results.

## 2.1 Waveguide Propagation

It is important to establish the mechanisms that describe the behaviour of optical signals within a waveguide. In this section, we will analyze the parameters and functioning of waveguide propagation in any platform. However, we will try to exemplify from the perspective of comparing the SOI and SiNOI platforms, using calculations and simulations. This will be important since waveguide propagation is a fundamental concept in the design of photonic devices and the two platforms are going to be used in this thesis.

In order to start the analysis of waveguide propagation, it is useful to make simplifications before a complete description of the propagation inside the typical single-mode strip waveguide. An infinitely wide slab waveguide is a good starting point. It consists of three vertically stacked materials with refractive indices  $n_0$ ,  $n_1$  and  $n_2$ , as illustrated in Fig. 2.1. Usually, the material in the middle is the one that guides the signal, and its refractive index  $n_1$  has necessarily the highest index among them. The solution of the boundary conditions for this structure will lead us to the concept of modal propagation [68].

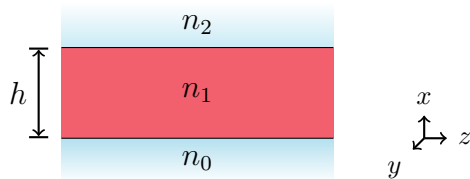


**Fig. 2.1** Example of a slab waveguide. The direction of propagation is  $z$ , the thickness  $h$  is in the  $x$  direction and the waveguide width is in the  $y$  direction.

The optical signal propagating through the waveguide is an electromagnetic wave consisting of an electrical field  $E$  and a magnetic field  $H$ . The orientation of the electric field determines the field's polarization. When it has no longitudinal component in the propagation direction and oscillates in the  $y$ -direction, it is a convention to call the signal TE polarized, whereas when that is the case for the magnetic field, the conventional term is that

it is a TM polarized signal.

Although we have established  $z$  as the propagating direction, there is another more useful term that is comprised of both the direction and the signal's frequency, which is the  $k$ -vector. It is usually defined in terms of the *vacuum wavevector* [68], as in equation 2.1.

$$k = \frac{2\pi}{\lambda} = \omega\sqrt{\mu_0\epsilon} = k_0n \quad (2.1)$$

The wavevector  $k$ , however, is not always entirely directed at the propagating direction. In fact, it comprises two components. The propagation coefficient  $\beta$ , which is the  $z$ -component of  $k$  and also known as the longitudinal wavevector, and the transverse wavevector  $\kappa$ . They are related to each other by a square angle, and thus we can use a Pythagorean relation  $k^2 = \beta^2 + \kappa^2$ , and with these values set for each mode, it is possible to determine their effective index through  $n_e = \frac{\beta\nu}{k_0}$ , where  $\nu$  is an integer relating to the mode.

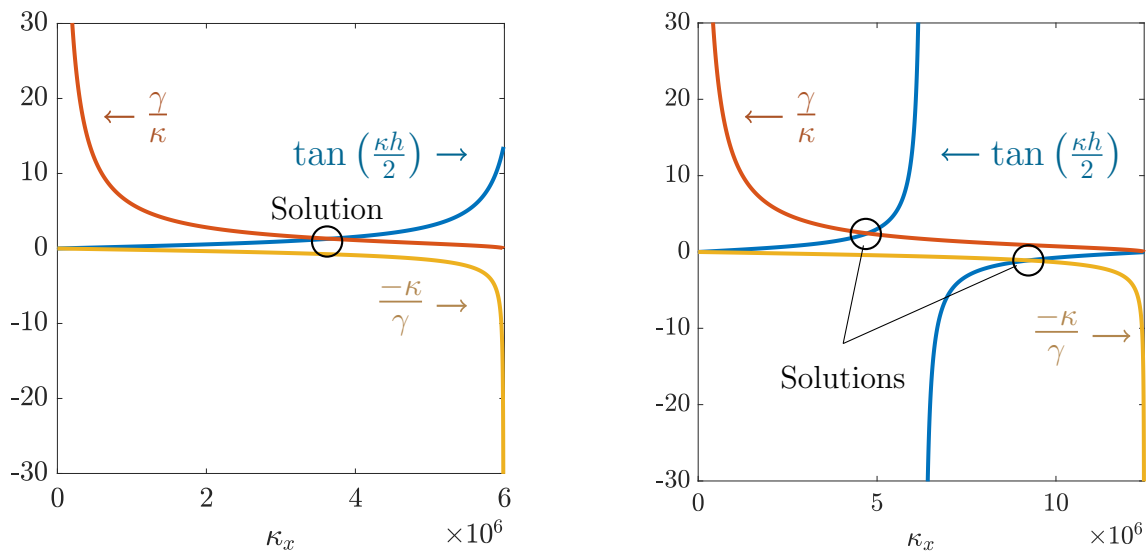
Applying boundary conditions to the wave equation it is possible to find the transcendental eigenvalue equations that can solve the number of propagating modes within the waveguide. The equation for the TE mode in a symmetric waveguide is shown in equation 2.2 and for the TM mode in equation 2.3, where  $\gamma = \sqrt{\beta^2 - k_0^2n_\nu^2}$ .

$$\tan\left(\frac{\kappa h}{2}\right) = \begin{cases} \frac{\gamma}{\kappa}, & \text{for even modes} \\ \frac{-\kappa}{\gamma}, & \text{for odd modes} \end{cases} \quad (2.2)$$

$$\tan\left(\frac{\kappa h}{2}\right) = \begin{cases} \left(\frac{n_1}{n_0}\right)^2 \frac{\gamma}{\kappa}, & \text{for even modes} \\ \left(\frac{n_1}{n_0}\right)^2 \frac{-\kappa}{\gamma}, & \text{for odd modes} \end{cases} \quad (2.3)$$

The solution to these equations can be seen graphically if we plot each side of the equa-

tions simultaneously and find where their curves meet. Each of the crossings/solutions is a valid value for  $\kappa$ , which means it also resolves a propagation constant  $\beta$  for each of these modes. To illustrate this, we can graph the solutions for these equations using a structure of the same dimensions, but different materials. Fig. 2.2(a) shows the solution of a 500 nm thick slab waveguide of SiN – as example, with  $n_1 = 2.07$ , surrounded by silicon dioxide with  $n_0 = 1.45$ , when the signal wavelength is 1550 nm and TE polarized. The fact that there is only one solution to the equations shows that this structure produces a single-mode behaviour in that condition. Fig. 2.2(b) shows the curves for a structure with same dimensions using Si instead of the SiN, increasing drastically the refractive index of the propagating material. The increase induces multimode support in the Si waveguide.



(a) Silicon Nitride slab waveguide.

(b) Silicon slab waveguide.

**Fig. 2.2** Solutions of the eigenvalue equations for a 1550 nm TE polarized signal propagating in a 500 nm thick SiN slab waveguide in (a), and a Si slab waveguide of same size in (b).

### 2.1.1 Normalized Parameters

The eigenvalue equations can solve for the effective index of a particular waveguide with given dimensions. However, there is an alternative method to finding the effective index of a waveguide that gives us a better understanding of the behaviour of the optical signal, which is using the normalizing parameters. The normalized index is  $b$  and the normalized frequency is  $V$  and they are described in equations 2.4 and 2.5 respectively.

$$b = \frac{(n_e^2 - n_0^2)}{n_1^2 - n_0^2} \quad (2.4)$$

$$V = k_0 h \sqrt{n_1^2 - n_0^2} \quad (2.5)$$

The normalized index  $b$  describes how the effective index relates to the surrounding indices of the waveguide, while the normalized frequency also comprises the wavelength of the signal and the thickness of the waveguide. The two parameters relate to each other according to equations 2.6 and 2.7 for TE and TM polarizations, respectively. The parameter  $a$  in the equations is the symmetry coefficient,  $a = \frac{n_2^2 - n_0^2}{n_1^2 - n_2^2}$ .

$$V_{\text{TE}} \sqrt{1 - b} = \nu \pi + \tan^{-1} \left( \sqrt{\frac{b}{1 - b}} \right) + \tan^{-1} \left( \sqrt{\frac{a + b}{1 - b}} \right) \quad (2.6)$$

$$V_{\text{TM}} \sqrt{1 - b} = \nu \pi + \tan^{-1} \left( \frac{n_1^2}{n_2^2} \sqrt{\frac{b}{1 - b}} \right) + \tan^{-1} \left( \frac{n_1^2}{n_0^2} \sqrt{\frac{a + b}{1 - b}} \right) \quad (2.7)$$

The  $b$ - $V$  curves comparing the Silicon platform to the Silicon Nitride we are using in this work can be seen in Fig. 2.3. It shows that the curves for both materials overlap and are practically the same for TE polarized signals, *i.e.*, an increase in thickness of the waveguide

as an increase in the normalized index that is very similar in both materials. However, the TM curve for the SiN platform is much closer to the TE curve. This means that the SiN, and consequently, the SiNOI platform has less birefringence. That naturally comes from the smaller index contrast from SiN to the dioxide. This plays an important role in devices that use multimode propagation, such as the Multimode Interferometer (MMI), or in devices that are designed for operation with both polarization modes, such as Polarization Beam Splitters (PBSs).

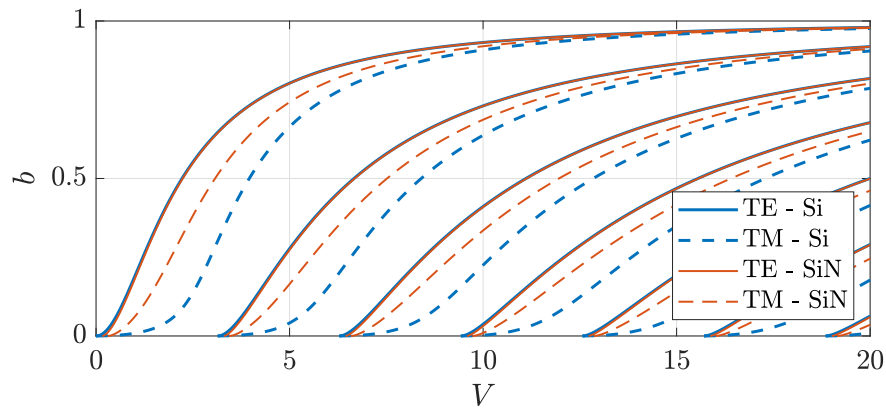


**Fig. 2.3** Normalized parameters curves comparing Silicon waveguides to Silicon Nitride.

### 2.1.2 Effective Index Method

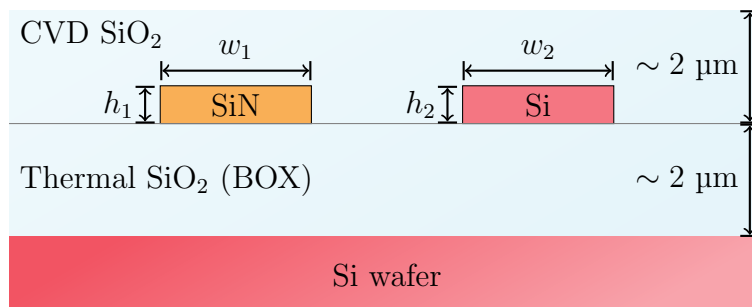


**Fig. 2.4** Cross-section of typical SiN and SOI strip waveguides.

The previous tools shown are used to find the effective index of slab waveguides with infinite width. However, we need an analysis to find the effective index in finite-width waveguides. The effective index method applies the slab waveguide analysis twice to find the effective index  $n_e$  of a strip waveguide [68]. It consists of considering a slab waveguide of vertically stacked materials with a certain thickness to find an effective index and using it as the intermediate effective index in a horizontal direction slab waveguide effective index solution. Using the effective index method, it is possible to estimate the effective index of typical strip waveguides, which is the type of waveguides we typically use in our projects. In a hybrid platform where we could deposit both Si and SiN, the cross-section of a structure with strip waveguides in both materials is illustrated in Fig. 2.4.

### 2.1.3 Width vs. Effective Index

The effective index method can estimate the effective index of a typical strip waveguide, but it has limitations. It is usually recommended that the width of the waveguide  $w$  is at least twice the thickness  $h$  [69]. A Finite Difference Eigenmode (FDE) solver, such as the one provided by Lumerical, provides a more faithful estimate of the effective index and is what we use to simulate the devices as a whole. Fig. 2.5 shows the results of FDTD Mode simulations. It shows the effective index of the first 8 modes as a function of width for both a 600 nm thick SiN waveguide and a 220 nm thick Si waveguide. The results shown are at the wavelength  $\lambda = 1550$  nm. Note that the limits of the  $y$ -axis are the same for Fig. 2.5(a) and (b), but since the refractive index of SiN is much lower, the modal effective indexes converge to a much lower value. Moreover, note that the curves in Fig. 2.5(b) approach two distinctive asymptotes for each mode as the waveguide width increases. The higher convergence level is for TE polarized modes, and the lower is for TM polarized. On the other hand, it is hard to distinguish the two levels of convergence in Fig. 2.5. This is a consequence of the lower

birefringence mentioned in the  $b$ - $V$  results shown in Fig. 2.3.

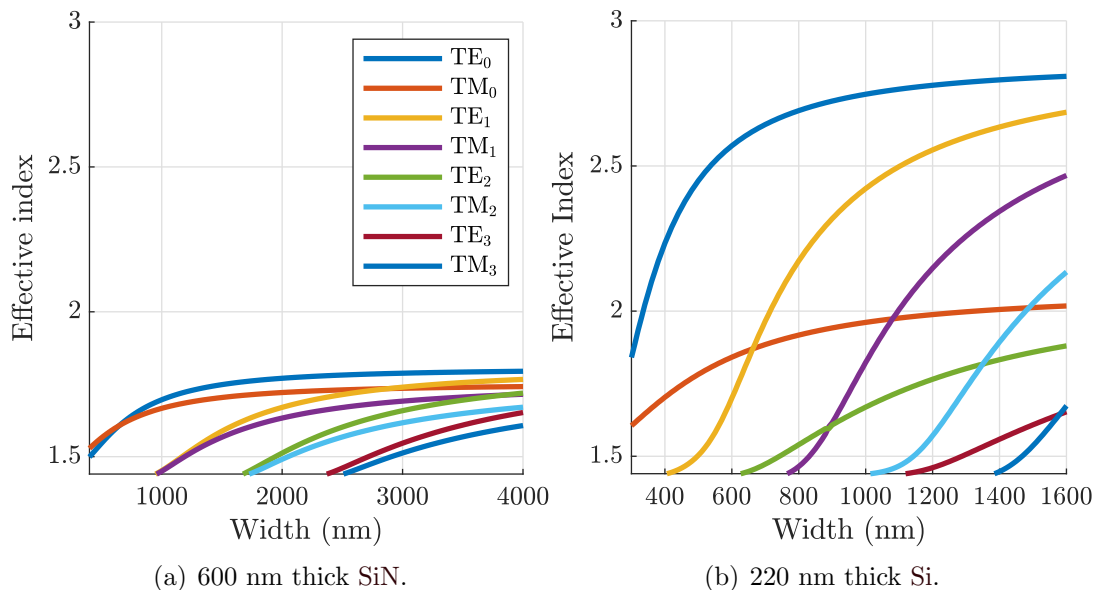


**Fig. 2.5** Effective index as a function of waveguide width in each material.

## 2.2 Bragg Gratings

The Bragg Grating is often called a frequency-selective mirror. The principle of operation of the device is shown in Fig. 2.6. Fresnel's equations determine the amount of signal that is reflected when there is a change in the effective index. As a consequence of consecutive and periodic changes in the effective index, the reflections are accumulated in the structure creating a reflection band in the wavelength response.

The longitudinal period  $\Lambda_B$  determines the Bragg wavelength, also known as the Bragg wavelength or centre wavelength of reflection,  $\lambda_B$ . The centre wavelength also depends on the effective index of the standard waveguide, as follows:

$$\lambda_B = 2\Lambda_B n_{\text{eff}} \quad (2.8)$$

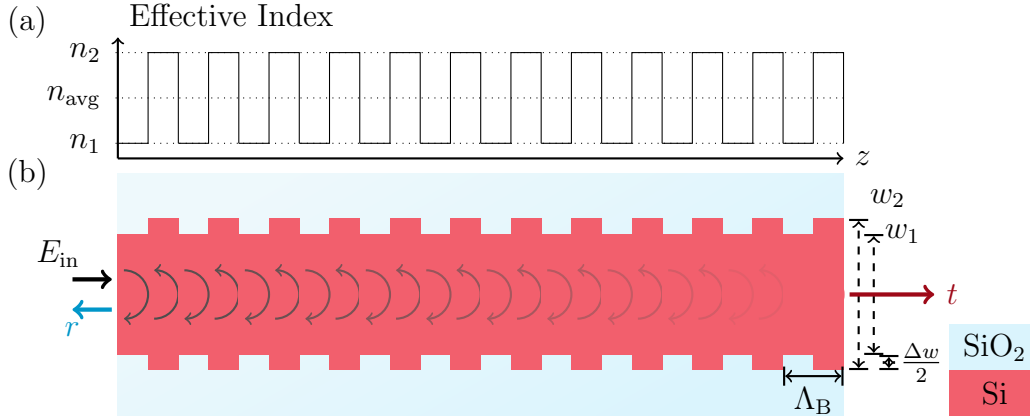


**Fig. 2.6** Principle of operation of the Bragg grating. Subfigure (a) shows the effective index change throughout the longitudinal position  $z$ , while (b) shows the top view of the structure built in SOI with changing width from  $w_1$  to  $w_2$ , and  $\Delta w = w_2 - w_1$ .  $E_{\text{in}}$  is the input signal,  $r$  is the reflected field and  $t$  is the transmitted field.

Since there are two effective index changes in each period, the total reflection created in one period can be found with Eq. 2.9 [70], where  $\Delta n$  is the change in effective index between the widths of the waveguide  $w_1$  and  $w_2$ , and  $\kappa$  comprises the coupling coefficient.

$$\kappa = 2 \frac{\Delta n}{2n_{\text{eff}}} \frac{1}{\Lambda} = 2 \frac{\Delta n}{\lambda_B} \quad (2.9)$$

The coupling coefficient of a sinusoidal profile, on the other hand, is given by Eq. 2.10 [70]. Note that the coupling coefficient of a sinusoidal profile grating is weaker than the standard square profile. The sinusoidal profile is the fundamental term of a Fourier series decomposition of the square profile and, therefore, we can use the comparison between the two profiles as a comparison between stronger and weaker gratings coupling coefficients.

$$\kappa_{\text{sin}} = \frac{\pi}{2} \frac{\Delta n}{\lambda_B} \quad (2.10)$$

FDTD is one of the possible ways of simulating WBGs. However, WBGs usually need con-

siderably long structures in order to get a reasonable peak-reflectivity, which makes FDTD a computationally expensive method of simulation. A more efficient way of simulating the structure is using the TMM [70].

### 2.2.1 Transfer-Matrix Method

We can express the behaviour of a system as a result of forward/backward propagating and reflected signals, as shown in Fig. 2.7, using the scattering matrices form, as in Eq. 2.11.

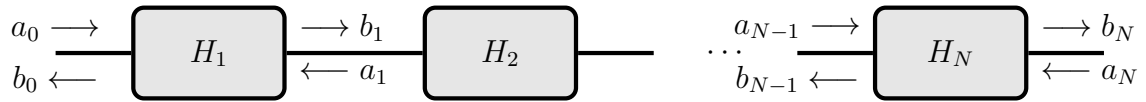


**Fig. 2.7** Illustration of the Transfer-Matrix Method.

$$\begin{bmatrix} b_0 \\ b_1 \end{bmatrix} = H_1 \begin{bmatrix} a_0 \\ a_1 \end{bmatrix} = \begin{bmatrix} h_{11} & h_{12} \\ h_{21} & h_{22} \end{bmatrix} \begin{bmatrix} a_0 \\ a_1 \end{bmatrix} \quad (2.11)$$

$$\begin{bmatrix} b_0 \\ b_1 \end{bmatrix} = \begin{bmatrix} h_{11}a_0 + h_{12}a_1 \\ h_{21}a_0 + h_{22}a_1 \end{bmatrix} \quad (2.12)$$

The scattering matrix form in Eq. 2.12 comprise the S-parameters of a 4-port device, in which each element in the system matrix  $H_1$  has a specific impact:  $h_{11}$  yields the input-side reflection from the system;  $h_{12}$  yields the amount of back-propagating signal that gets through the system to the input-side; similarly,  $h_{21}$  yields the amount of signal that goes through the system; and finally,  $h_{22}$  is the reflection in the output-side of the system.

Another simplification that the TMM provides is that the relation between the signals in the input side of all the subsystems and the output side can be computed by using simple matrix multiplication of the subsystems scattering matrices. The scattering matrix that

expresses the behaviour of the overall system  $H_{\text{total}}$  is the multiplication of all the subsystems  $H_i$ , as in 2.13 and, as a result, we can relate the input and output signals directly.

$$H_{\text{total}} = \prod_{i=1}^N H_i \quad (2.13)$$

$$\begin{bmatrix} b_0 \\ b_N \end{bmatrix} = H_{\text{total}} \begin{bmatrix} a_0 \\ a_N \end{bmatrix} \quad (2.14)$$

Any small inaccuracy in the modelling of a TMM cell might accumulate over the length of a long grating. In short lengths, the accuracy of full 3D FDTD simulations might become beneficial. However, for longer structures (longer than a few hundred micrometers), the accuracy compromise of using 2.5D FDTD defeats its purpose, and the computational cost efficiency of TMM becomes advantageous.

By expressing the behaviour of these subsystems using TMM it becomes possible to simulate Bragg gratings by defining the respective transfer matrices. These will differ depending on the assumed profile of the grating.

### 2.2.2 Squared Profile

To build the transfer matrices required for a squared profile grating, as illustrated in Fig. 2.6, we need two types of matrices: one for homogeneous waveguides, and another for the transition between waveguides with different widths. The transfer matrix for a homogeneous waveguide is shown in 2.15, where  $\beta$  is the propagation-phase constant and  $L$  is the length of the waveguide subsection. We can see it only describes forward and backward propagation, with no reflections.

$$T_{\text{hw}} = \begin{bmatrix} e^{j\beta L} & 0 \\ 0 & e^{-j\beta L} \end{bmatrix} \quad (2.15)$$

The transfer-matrix that describes the transition between waveguides with different widths is shown in 2.16 [70], where  $n_i$  and  $n_j$  are the effective indexes of the  $i^{\text{th}}$  and  $j^{\text{th}}$  subsection of the grating.

$$T_{\text{is}_{ij}} = \begin{bmatrix} 1/t & r/t \\ r/t & 1/t \end{bmatrix} = \begin{bmatrix} \frac{n_i+n_j}{2\sqrt{n_i n_j}} & \frac{n_i-n_j}{2\sqrt{n_i n_j}} \\ \frac{n_i-n_j}{2\sqrt{n_i n_j}} & \frac{n_i+n_j}{2\sqrt{n_i n_j}} \end{bmatrix} \quad (2.16)$$

As shown in Eq. 2.13, it is now possible to combine the transfer matrices to comprise a full period of the grating, as shown in Eq. 2.17.

$$T_p = T_{\text{hw}_i} T_{\text{is}_{ij}} T_{\text{hw}_j} T_{\text{is}_{ji}} \quad (2.17)$$

### 2.2.3 Sinusoidal Profile

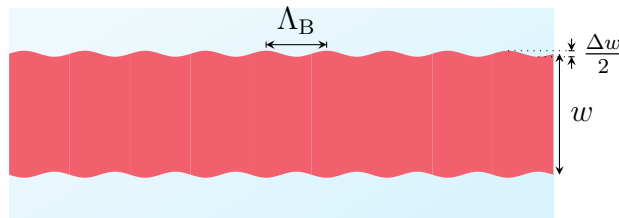


**Fig. 2.8** Top view of a WBG in which the sidewall corrugations have sinusoidal profile.

The premise for building the transfer matrices for a sinusoidal profile, as illustrated in

Fig. 2.8, is that the effective index and propagation loss are themselves sinusoidal, as shown in Eq. 2.18 and 2.19, where  $\tilde{n}(z)$  is the effective index throughout the longitudinal position  $z$ ,  $\tilde{\alpha}$  is the loss profile,  $\beta$  is  $\frac{\pi}{\Lambda}$  and  $\Omega$  is the phase of the sinusoidal profile at  $z = 0$ .

$$\tilde{n}(z) = n_{\text{eff}} + \tilde{n}_1 \cos(2\beta z + \Omega) \quad (2.18)$$

$$\tilde{\alpha}(z) = \tilde{\alpha}_0 + \tilde{\alpha}_1 \cos(2\beta z + \Omega), \quad (2.19)$$

The elements of the transfer-matrix of one period with sinusoidal profile can be derived from Coupled-Mode Theory (CMT) [71] and are as shown in 2.20 through 2.24. Here, the propagation constant is  $\gamma = \frac{\pi\tilde{n}_1}{\lambda_0} + j\frac{\tilde{\alpha}_1}{2}$ ,  $\Delta\beta = \beta_0 - \beta$  (where  $\beta_0 = k_0 n_{\text{eff}}$ ), and the simulated coupling coefficient is  $\kappa = \sqrt{(\tilde{\alpha}_0 - j\Delta\beta)^2 + \gamma^2}$ .  $\Omega$  represents a phase shift in the sinusoidal profile, which is useful when modifying the model to account for apodization, by making sure there are only smooth transitions.

$$T_p = \begin{bmatrix} t_{11} & t_{12} \\ t_{21} & t_{22} \end{bmatrix} \quad (2.20)$$

$$t_{11} = \left[ \cosh(\kappa L) - \frac{\tilde{\alpha}_0 - j\Delta\beta}{\kappa} \sinh(\kappa L) \right] e^{j\beta_0 L} \quad (2.21)$$

$$t_{12} = \frac{j\gamma}{\kappa} \sinh(\kappa L) e^{-j(\beta_0 L + \Omega)} \quad (2.22)$$

$$t_{21} = -\frac{j\gamma}{\kappa} \sinh(\kappa L) e^{j(\beta_0 L + \Omega)} \quad (2.23)$$

$$t_{22} = \left[ \cosh(\kappa L) + \frac{\tilde{\alpha}_0 - j\Delta\beta}{\kappa} \sinh(\kappa L) \right] e^{-j\beta_0 L} \quad (2.24)$$

Regardless of the profile used, if the grating has a uniform corrugation depth, the total

grating transfer matrix can be found by raising  $T_p$  to the power of the number of grating periods  $N$ . If the grating is apodized, it is necessary to determine the transfer-matrix  $T_n$  for each period  $n$  and compute the product of all transfer matrices, as expressed in 2.25. Interpolation can be used to reduce the amount of data needed to import into TMM for the simulation of apodized structures.

$$T_{\text{BG}} = \begin{bmatrix} T_{11} & T_{12} \\ T_{21} & T_{22} \end{bmatrix} = \begin{cases} T_p^N, & \text{uniform grating} \\ \prod_{n=1}^N T_n, & \text{apodized grating} \end{cases} \quad (2.25)$$

After obtaining  $T_{\text{BG}}$ , the transmission  $T$  and reflection  $R$  curves can be calculated with Eq. 2.26.

$$T = \left| \frac{1}{T_{11}} \right|^2, \quad R = \left| \frac{T_{21}}{T_{11}} \right|^2 \quad (2.26)$$

The product operation used for apodized gratings in Eq. 2.25 can also be used to compute the result of random variations in each subsection of the WBG periods. All that is needed to compute these curves is to extract the parameters used in each of the transfer matrices, notably the wavelength and waveguide dimension-dependent effective index, and follow the algorithm described here.

Effectively, the design process used in this thesis can be illustrated in Fig. 2.9. We extract the effective index from FDTD simulation for a range of waveguide dimensions and wavelengths, import it to Matlab TMM simulations and use the simulated results to tune the resulting curves as desired, such as BW and peak-reflectivity. After the design parameters

are decided, the layout is submitted for fabrication and we characterize the fabricated device.

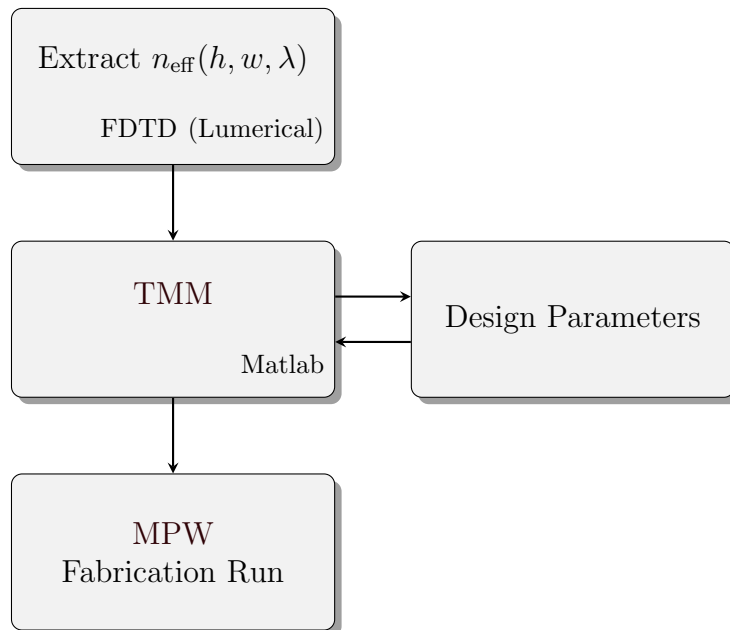


**Fig. 2.9** Simulation and design process of the Bragg grating.

### 2.2.4 Sampled Bragg Gratings

The Sampled BG is a derivation of the BG that yields multiple reflection peaks with controlled spacing [60, 63, 72–74]. It is comprised of periodic sections of BGs intersected by homogeneous waveguides. The device finds applications in many fields, such as in WDM systems and lasers. An illustration of the device is shown in 2.10.

The Sampled BG can be simulated using the same background already presented in this section. Once the transfer-matrix  $T_{\text{BG}}$  for a section of BG of length  $L_{\text{BG}}$  is computed, it can be followed by multiplying it by the transfer-matrix of homogeneous waveguide, as in Eq. 2.15, of length  $L_{\text{wg}} = \Lambda_{\text{Sample}} - L_{\text{BG}}$ . The resulting matrix  $T_{\text{Sample}} = T_{\text{BG}}T_{\text{wg}}$  is the transfer-matrix that describes the behaviour of one sampling section of the Sampled WBG. This process of multiplying the matrices can continue for however many sampling sections

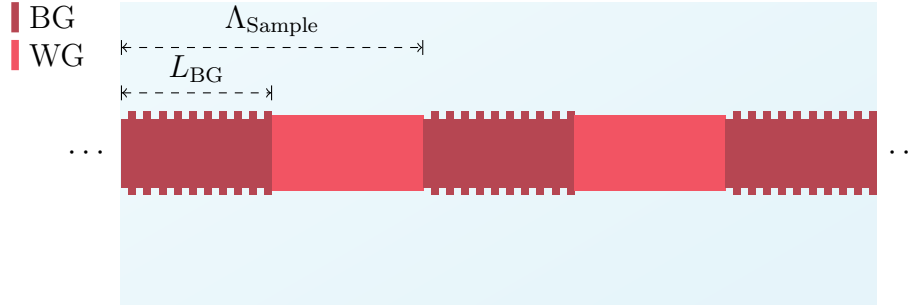


**Fig. 2.10** The Sampled Bragg Grating.

the structure has. The spacing between the reflection bands is determined by controlling the sampling period  $\Lambda_{\text{Sample}}$ , and it is determined by Eq. 2.27.

$$\Delta\lambda = \frac{\lambda_{\text{B}}^2}{2n_{\text{eff}}\Lambda_{\text{Sample}}} \quad (2.27)$$

The number of sampling sections determines the number of reflection band replicas spaced by  $\Delta\lambda$  from  $\lambda_{\text{B}}$  and also the peak-reflectivity since each section comprises a new subsection of WBG with length  $L_{\text{BG}}$  and contributes with more reflection.

## 2.3 Subwavelength Gratings

SWG are similar structures to the BGs, *i.e.*, they comprise a longitudinally periodic index variation. However, the fundamental condition for SWGs is that their longitudinal period has to be much lower than propagating signal's wavelength, *i.e.*,  $\Lambda_{\text{SWG}} \ll \lambda$ , where  $\Lambda_{\text{SWG}}$  is the SWG longitudinal period and  $\lambda$  is the signal wavelength. It was first demonstrated in [75]. When first introduced, the main characteristic was its promise of lower propagation losses when compared with a solid-core waveguide (which is yet to be achieved). It also significantly lowers the effective index of the waveguide, and we can control how much by

determining the duty cycle  $DC_{\text{SWG}}$  as in Eqs. 2.28-2.29 [76], where  $n_{\text{eff}}$  is the resulting effective index,  $n_1$  is the high-index material used in the waveguide, and  $n_2$  is the low-index material surrounding the waveguide (in this work, Silicon Dioxide).

$$n_{\text{eff}}^2 \approx n_1^2 DC_{\text{SWG}} + n_2^2 (1 - DC_{\text{SWG}}), \quad \text{for TE mode} \quad (2.28)$$

$$n_{\text{eff}}^{-2} \approx n_1^{-2} DC_{\text{SWG}} + n_2^{-2} (1 - DC_{\text{SWG}}), \quad \text{for TM mode} \quad (2.29)$$

The structural comparison of a solid-core strip waveguide with the SWG waveguide is illustrated in Fig. 2.11. While we can control the effective index of a single-mode solid-core strip waveguide by controlling its width  $w$ , the SWG offers further control over many important propagation parameters, such as dispersion, nonlinearity, birefringence [77–79].

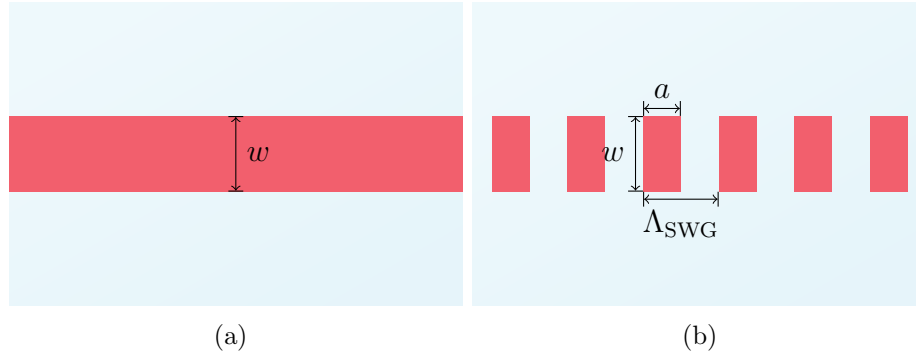


**Fig. 2.11** Top view comparison between the solid core waveguide in (a) and the Subwavelength grating waveguide in (b).

The most appropriate simulation technique to use with SWG structures is the Bloch-Floquet principle [80], which is derived from Maxwell’s equations and defines the propagation of a signal in a periodic structure. It states,

$$E(z) = e^{jk \cdot z} u(z) \quad (2.30)$$

where  $E$  is the wave function,  $z$  is the longitudinal position,  $k$  is the wave-vector and  $u$  is a periodic function of the media, *i.e.*,  $u(z) = u(z + \Lambda_{\text{SWG}})$ . The Bloch boundary conditions are also usually available in simulation software, such as Lumerical, meaning that the simulation will assume the structure inside given boundaries to be periodical in a given direction.

By defining the Bloch boundaries in an FDTD simulation, we can extract the bandstructure, which is a valuable analysis tool for SWG structures. This procedure is detailed in [81]. The script relies on the Chirped Z-Transform (CZT) of several time-monitors to extract the spectrum over frequency  $f$  and the wave-vector in the propagation direction  $k_z$ . Fig. 2.12 shows the resulting 2D spectrum for an SWG of width  $w = 400$  nm, thickness  $h = 220$  nm, periodicity  $\Lambda_{\text{SWG}} = 200$  nm and duty cycle  $DC = 0.5$ . From the peaks in this spectrum curves, we can then extract the propagation coefficient  $\beta$  as a function of wavelength/frequency. If the curve lies above the lightline (which is the line at  $f = \frac{\beta}{n_{\text{sub}}}$ , where  $f$  is the frequency and  $n_{\text{sub}}$  is the substrate refractive index), the waveguide will behave as a grating coupler, scattering light downward to the substrate and upward to the clad. Otherwise, if the curve lies below the lightline, the grating will behave as a low-loss waveguide. Also, the  $\beta(\lambda)$  curve allows us to extract the phase and group velocities, which can then be used to calculate the effective and group index of the waveguide.

As another example, Fig. 2.13 shows the extracted effective index from the bandstructure as a function of the SWG width  $w$  at three different wavelengths, 1310 nm, 1550 nm, and 2000 nm. The graph illustrates two points: (1) there is dispersion in the waveguide, *i.e.*, there is a wavelength dependence on the effective index, and (2) such dispersion changes with difference SWG segment widths  $w$ , namely, the effective index change  $\Delta n_{\text{eff}}$  depending on the wavelength of the propagating signal is directly proportional to  $w$ .

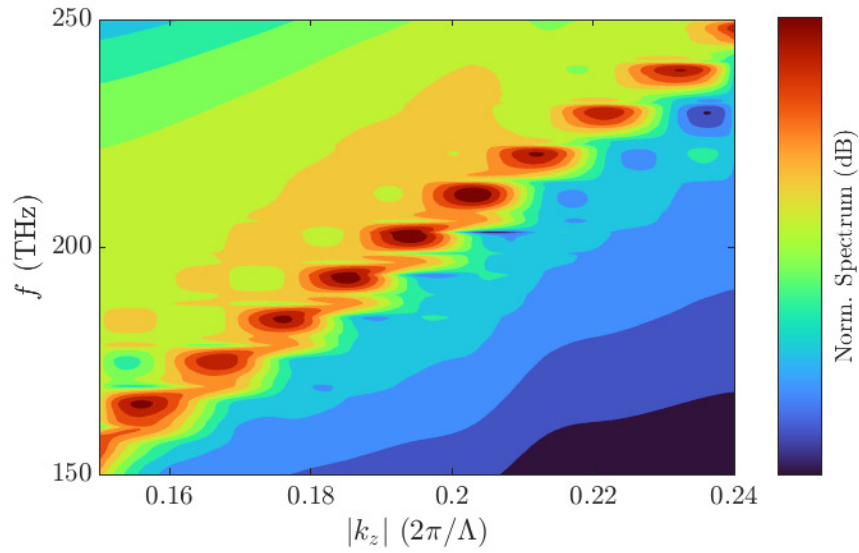


**Fig. 2.12** Example of the  $f$ - $|k_z|$  spectrum of an SWG waveguide.

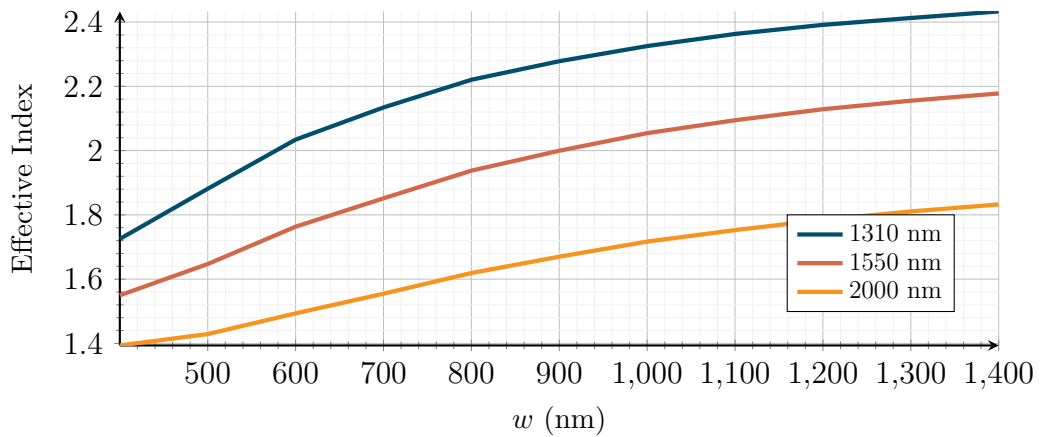


**Fig. 2.13** Effective index with varying width  $w$  at different wavelength channels.

### 2.3.1 Subwavelength Grating Waveguide Bragg Gratings

The SWG also involves a periodic variation in index with a period much smaller than the wavelength of the propagating signal. It is possible to build SWG waveguides that operate in the subwavelength regime while imposing an additional periodic variation in the effective index along the direction of propagation to enable Bragg reflection.

There are many techniques to construct the Bragg grating with SWGs, such as interleaving two SWG waveguides with different duty cycles [82]. However, in this thesis, we use a cladding modulation technique that employs loading segments alongside the SWG waveguide to build the SWG-WBGs. This was first demonstrated in [83], where they placed one pair of loading segments for every two SWG periods. Another way of achieving Bragg reflection is by placing two pairs of loading segments with different gap distances, as illustrated in Fig. 2.14 [84, 85]. The effective index of the loaded waveguide is inversely proportional to the gap distance  $g$ , which periodically changes with period  $\Lambda_{\text{BG}} = 2\Lambda_{\text{SWG}}$ . The periodic index change gives rise to the Bragg reflection.

An interpolation of the effective index as a function of wavelength  $\lambda$  and gap distance  $g$  can be seen 2-D plotted in Fig. 2.15. We can notice that the effective index is highest at lower wavelengths and small gap distances, where  $n_{\text{eff}} \approx 1.65$ , and lowest at higher wavelengths and long gap distances, where  $n_{\text{eff}} \approx 1.53$ , but still higher than the dioxide refractive index of 1.44, allowing for the signal to couple and properly propagate through the SWG waveguide.

With the  $n_{\text{eff}}$  space map shown in Fig. 2.15 it is possible to determine the effective index of any gap distance. By using the effective index change caused by the loading segments positioned  $g$  away from the SWG waveguide, we can use the TMM technique, such as elaborated in Section 2.2, to find the resulting transmission and reflection spectrum of a SWG-WBG.

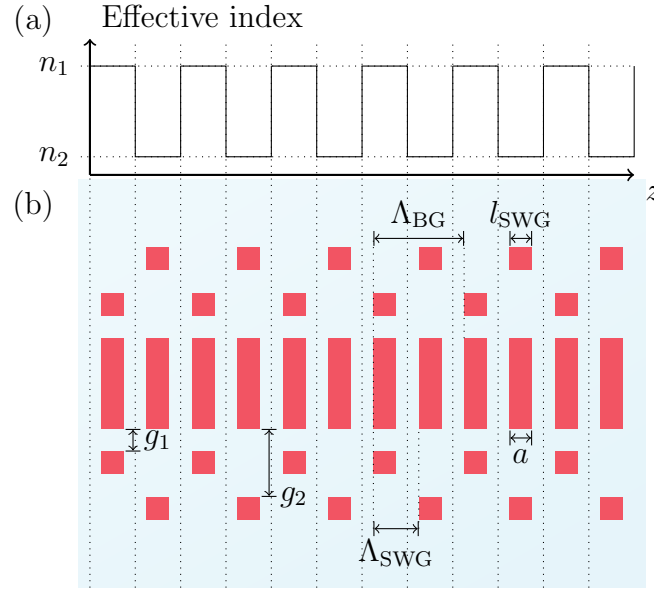


**Fig. 2.14** The effective index curve of the SWG-WBG in (a), and the layout using two pairs of loading segments in (b).

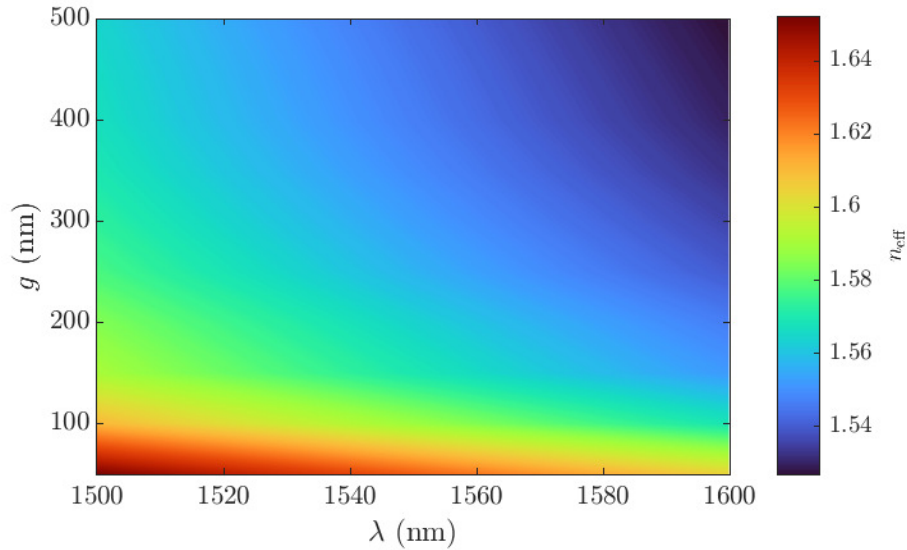


**Fig. 2.15** Effective index as a function of wavelength and gap distance of an SWG-based waveguide that uses loading segments, in which  $w = 400$  nm,  $\Lambda_{\text{SWG}} = 254$  nm,  $a = 127$  nm, and  $l_{\text{SWG}} = 127$  nm.

---

## 2.4 Summary and Conclusion

In this chapter, we have shown a few methods for estimating the effective index of waveguides. They can be useful, although in our simulations we use the Lumerical software suite for estimating the effective index of both solid core and SWG waveguides. We have also elaborated on the TMM, which allows for efficient simulations of BGs, and we've shown the bandstructure simulations for estimating the effective index of SWG. With this background, we can simulate the devices detailed in the following chapters.

## Chapter 3

# Fabrication Variation Estimations for Silicon Nitride Bragg Gratings

When the fabrication of SiN WBGs was being planned – between 2018 and 2019, there were very few accessible published works on either SiN Vertical Grating Couplers (VGCs) or SiN WBGs. This motivated us to (1) use the edge coupling technique to couple light into the waveguides, and (2) fabricate SiN WBGs and analyze the results. Since then, some studies on WBGs in SiN have been presented [86–91]. Using edge-coupling allowed us to analyze the reflection curves in both TE and TM polarization modes simultaneously, which is otherwise difficult to do.

In this chapter, we describe the design, characterization WBGs, and analysis of both the measured responses and simulations. With the comparison between simulated and measured responses, we introduce changes to the simulation model based on known fabrication variations of SiN, aiming to enhance the simulation model. Our improvements focus on SiN but can be applied to any platform.

This chapter will firstly introduce and motivate the use of WBG and the SiNOI platform. Secondly, we will show the characterized results. Thirdly, we will show the model modifications we introduce to take into account the expected fabrication variations. We will then use these modifications to analyze the fabrication variations and, lastly, we will conclude the chapter. The chips were fabrication in collaboration with Dr. Victor Torres Company's team at the Chalmers University of Technology.

### 3.1 Introduction

Frequency multiplexing has always been a fundamental building block of communication systems, where frequency-selective filters are a vital piece. In the optical communication field, Bragg gratings have filled that role effectively, including in integrated photonic applications.

As research and the technology on optical systems develops, alternatives to the SOI platform appear to overcome some of its drawbacks. That is the case for the SiNOI platform. Although confinement is weaker in the platform due to the lower refractive index, some of its advantages are a higher transparency range, lower propagation loss, thermal robustness, and its potential for nonlinear applications due to its absence of TPA. Furthermore, the film can be deposited on the wafer through PECVD and LPCVD, which are compatible with the vast CMOS technology infrastructure already in place [92]. There is an increasing interest in the platform due to these advantages and traditional devices in the SOI platform are being now transferred to SiN. One of these devices is the WBG [88, 90, 93].

As we design, model, simulate and characterize devices for the SiN platform, we encounter challenges and differences from the SOI platform in simulation, fabrication and experimental characterization. However, these differences allow us to probe the accuracy of fabrication

parameters and simulations. In this chapter, we follow that process for SiN WBGs. We show the model, design, characterized and measured results, and we propose modifications to the model to account for fabrication imperfections and fit them to the characterizations, allowing us to better anticipate future results. We also use the divergences between simulation and characterization to infer the fabrication impact on the dimensions of the waveguides.

### 3.2 Characterization Setup

The coupling setup consisted of one six-axis stage and two XYZ-stage, and it was assisted by a microscope for positioning the lensed fibres. The light was coupled into the waveguides by measuring the output power of the coupling with a Power Meter. The schematic of the setup can be seen in Fig. 3.1.

The devices were fabricated at the Chalmers University of Technology, with the collaboration of Dr. Victor Torres-Company's team. They fabricated the devices in a 600 nm thick SiN layer over a 2  $\mu\text{m}$  thick buried-oxide (BOX) and 2  $\mu\text{m}$  thick cladding using 1 nm resolution EBeam lithography. The chip was cleaved into a 1  $\text{cm}^2$  square piece.

The characterization setup includes a SOA with Amplified Stimulated Emission (ASE) centred at the wavelengths of interest, an Optical Polarization Controller (OPC), an Optical Spectrum Analyser (OSA) and the coupling setup. The OSA used a high sensitivity setting and the resolution was 10pm unless otherwise mentioned.

Since the edge-coupling was done using a newer, more accurate six-axis stage on the input side of the system, the Insertion Loss (IL) was lower than on the output side, which used an XYZ stage. We occasionally emphasize the reflection curves over the transmission

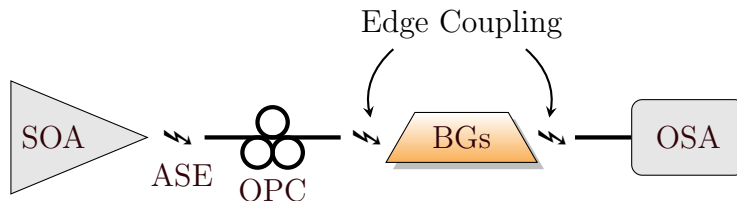


**Fig. 3.1** Experimental setup.

for that reason. The ILs were observed typically between 20 dB and 25 dB. In our devices, we estimated propagation losses by evaluating the minimum ILs of several characterizations of waveguide structures with different lengths. Our estimation is approximately 1 dB/cm, which is coherent with the expected propagation losses of Silicon Nitride. We could have a more accurate propagation loss estimation by matching simulated and characterized results of MZIs. Unfortunately, we did not include them in the fabricated chip. We did not have access to a polarizer in the experiment, so we were not able to ensure the power was concentrated in a particular polarization while characterizing it. Were the light purely TE polarized, the characterized wavelength response would show one reflection band at  $\lambda_{\text{TE}} = 2n_{\text{avgTE}}\Lambda_{\text{B}}$  and no reflection at  $\lambda_{\text{TM}} = 2n_{\text{avgTM}}\Lambda_{\text{B}}$ , and vice-versa, where  $n_{\text{avgTE}}$  and  $n_{\text{avgTM}}$  are the average effective index for the TE and TM modes, respectively. Without the polarizers, we can still see the reflection bands for both polarization modes, but not the full peak reflectivity.

### 3.3 Design

The common parameters between all fabricated WBG structures and simulation devices, unless otherwise mentioned, are shown in Table 3.1. Since we took part in a fabrication run planned by Dr. Company's team, the SiN film thickness was previously decided, *i.e.*,  $h = 600$  nm. The average waveguide width  $w_{\text{avg}}$  of 1  $\mu\text{m}$  is appropriate for single-mode

propagation in both TE and TM polarization modes. The total length  $L$  of 8.76 mm is large enough to take almost the entire chip length of 1 cm while leaving a safe distance from the edges, where the Bragg gratings could be cleaved.

The Bragg period  $\Lambda_B$  was initially decided so that the Bragg wavelength would be in the C-band. However, a unit conversion issue with the scripts that converted the ellipsometry measurements into the refractive index curves and imported them to Lumerical resulted in a Bragg wavelength in the S-band for both TE and TM modes. Fortunately, this issue did not prevent the characterization of the devices.

**Table 3.1** Common parameters of the fabricated SiN WBGs.

Parameter	$\Lambda_B$	$N_G$	$L$	$h$	$w_{\text{avg}}$
Value	438 nm	20,000	8.76 mm	600 nm	1 $\mu\text{m}$

We have fabricated Bragg gratings with corrugation depths of 20 nm, 50 nm, 60 nm, and 100 nm. A corrugation depth  $\Delta w$  of 20 nm represents a change in the effective index for TE mode of  $\Delta n = 0.0034$ , which is approximately 0.2% of the uniform strip waveguide effective index, or the average effective index of the grating. This is a small effective index perturbation, although we can expect the lithographic resolution (of 1 nm) to resolve the structure with accuracy. Early simulations of 1 cm long apodized gratings showed a BW of approximately 3 nm in the TE polarization mode and 2 nm for the TM mode, which should be easy to characterize with our characterization setup. A corrugation depth of  $\Delta w = 100$  nm yields an effective index change of approximately  $\Delta n = 0.017$ , which is approximately a 1% change of the average effective index in the grating. Early simulations of a 1 cm long apodized structure showed a BW of 15 nm for the TE polarization mode and 10 nm for the TM mode. The two corrugation depths are large enough for the lithographic resolution and not too large that the effective index perturbation would cause light scattering, which

would not be accurately simulated using TMM. We include 50 nm and 60 nm as intermediate corrugation depths for better analysis.

All of the gratings are apodized using a Gaussian profile with a standard variation of  $\sigma = 0.35$ , *i.e.*, if the propagation axis is normalized to  $z = -1$  at the beginning of the grating and  $z = 1$  at the end, the width of each Bragg period section could be found by iterating the period position  $z$  in  $w[z] = \Delta w \cdot e^{-\frac{1}{2}\left(\frac{z}{\sigma}\right)^2}$ , where  $\Delta w$  is corrugation depth at its maximum in the apodized grating. The apodization function was empirically decided based on the suppression of the sidelobes in simulated results. We have only used one apodization profile in the analysis in order to reduce the parameter space.

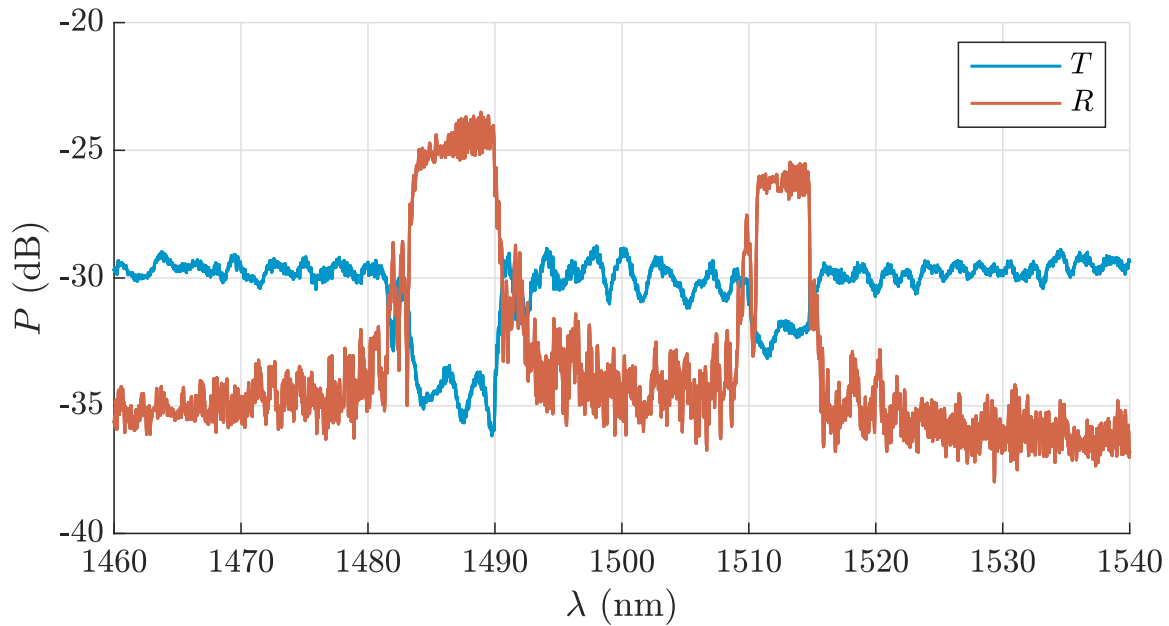
### 3.4 Characterized Results

Figure 3.2 shows the characterized results for one of the WBGs with a corrugation depth of  $\Delta w = 60$  nm. Fig. 3.2(a) shows a broad spectrum that includes the reflection and transmission responses of the Bragg grating for both polarizations simultaneously with the OSA resolution of 20 pm, while Fig. 3.2(b) and 3.2(c) show a focused span with a resolution of 2 pm of TE and TM polarizations, respectively.

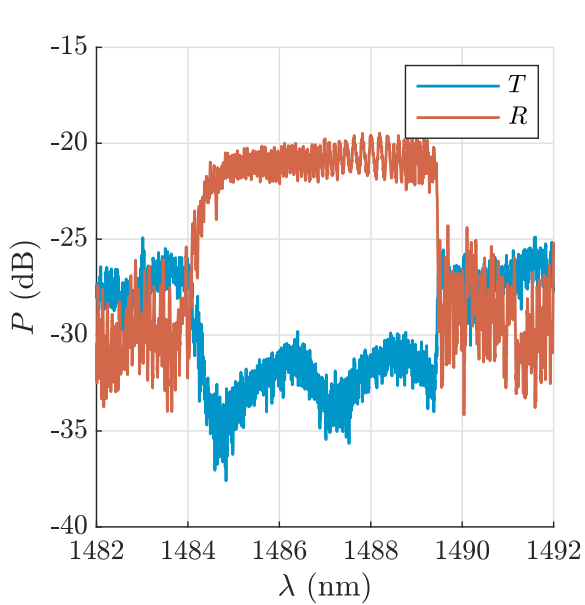
In Figs. 3.2(b) and 3.2(c), where the resolution provides more detail, we can see that there are oscillations in the reflection response which may be due to Fabry P erot (FP) resonances in the fibre-to-chip interface.

### 3.5 Analysis

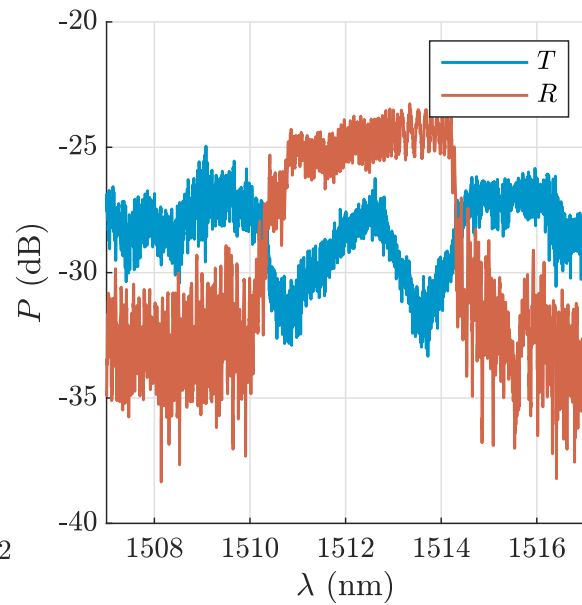
It is important to evaluate the similarity between simulated and characterized results and, as shown, there are key divergences. Since we used the edge-coupling technique, without



(a) Broad spectrum with both polarizations.



(b) TM mode.



(c) TE mode.

**Fig. 3.2** Reflection  $R$  and transmission  $T$  spectra of SiN Bragg gratings.

VGCs, there was no suppression of polarization except for the manual control of the OPC. The absence of a polarization-selective structure makes the peak-reflectivity measurement less reliable. However, the Bragg wavelength (or Bragg wavelength) and the BW of the filter can be analyzed.

The fabrication process of the SiNOI platform is known to have variations from the layout imposed through a lithographic mask [94–99]. Besides the issues known to the SOI platform as well, such as sidewall angle and random corrugations due to the etching step of the CMOS process, the SiN is known to shrink after deposition, and the SiN film thickness varies radially over the Si insulator.

Amongst the types of shrinkage that the Bragg grating structures are subject to, the two key shrinkages to the performance of the devices are longitudinal and transversal shrinkage. The locations where they are likely to occur are illustrated in Fig. 3.3, in which (A) depicts the longitudinal shrinkage that can cause the wide sections of the Bragg period to reduce in length, and (B) and (C) show where the transversal shrinkages can occur.

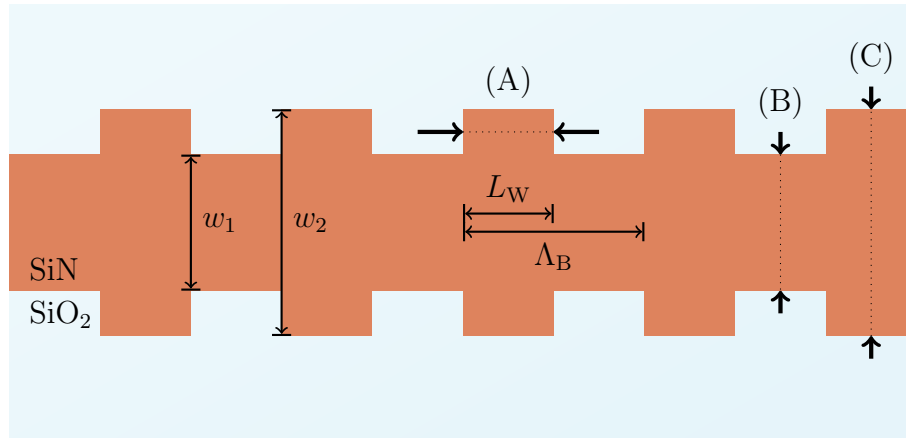


**Fig. 3.3** Characteristic shrinkage of deposited SiN. (A) shows the longitudinal shrinkage, and (B) and (C) show the transversal types of shrinkage over  $w_1$  and  $w_2$ , respectively.

Regarding the transversal shrinkages, there are two plausible hypotheses: (1) the size reduction caused in the narrower section (B) is the same as in the wider section (C), and (2) the narrower section (B) is subjected to less shrinkage than the wider section (C). In hypothesis (1) the corrugation depth  $\Delta w$  remains the same, but the average width of the structure and, as a consequence, the average effective index  $n_{\text{avg}}$  is reduced.

We posed the question of which of these two hypotheses is more likely to Dr. Torres Company and his team, who fabricated the devices. It was their understanding that hypothesis (1) is more likely, the shrinkage in (B) and (C) should be very similar or, at least, the difference is negligible.

According to their expertise in the fabrication process of SiN structures, we should also expect:

- Refractive index accuracy of up to  $\pm 0.001$  – in other words,  $n(\lambda) = \hat{n}(\lambda) + e$ , where  $\hat{n}(\lambda)$  is the characterized refractive index through ellipsometry,  $n(\lambda)$  is the actual refractive index, and  $e$  is the possible measurement error of at most  $\pm 0.001$ ;
- waveguide sidewall angle of  $85^\circ$ ;
- thickness variation of 3% towards the edges of the wafer;
- average transversal waveguide shrinkage of 50 nm.

These points will inform the presumptions and hypotheses of fabrication variations that we will consider in the analysis of the results. Unfortunately, we did not have access to SEM images of the fabricated devices to verify which of these variations were actually present.

### 3.5.1 Analysis Presumptions

We can consider many types of variations in order to adapt and improve the simulations. However, some possible variations are challenging to consider using FDTD-assisted TMM simulations. Therefore, it is important to list the presumptions we are assuming for this analysis and the respective reasons.

#### Accurate Refractive Index

Informed by the highly accurate characterization of the refractive index through ellipsometry, we will assume that the characterized refractive index curve  $\hat{n}(\lambda)$  is the actual refractive index  $n(\lambda)$ .

#### Waveguides with Constant Thickness

We will assume that the thickness is constant throughout the Bragg structures. In other words, the top and bottom of the waveguides will be considered perfectly flat. The accuracy of SiN films can be around 1 Å [100], although we were informed that in this specific fabrication run we should expect a 3% increase in the outer regions of the insulator.

The process of shrinkage that the SiN material is subject to might impose a thickness variation, especially in the corners of the gratings. However, it would be significantly time-consuming to consider this vertical variation in the TMM simulations and, thus, this is kept outside the scope of this analysis.

#### Rounding of Corners

The fabrication process of both Si and SiN is known to impose rounding of square corners. We can consider the impact of such rounding by comparing the simulated results of a perfectly square profile with the simulation of the fundamental term of the Fourier Series of the square profile, which is a sinusoidal profile.

### Shrinkage

As previously mentioned and illustrated in Fig. 3.3, we will consider two types of shrinkage. However, informed by our collaboration with Dr. Victor Torres Company's team, we will consider the transversal shrinkages to submit the same width variation to both the narrower and wider sections of the Bragg period.

Regarding the longitudinal shrinkage, it is possible to consider this variation in simulation by imposing a Duty Cycle on the square profile. In the case of the sinusoidal profile, it is possible to shrink the length of the sinusoidal period and follow it by a constant-width waveguide to compose one Bragg period. These adaptations are illustrated in Fig. 3.4.

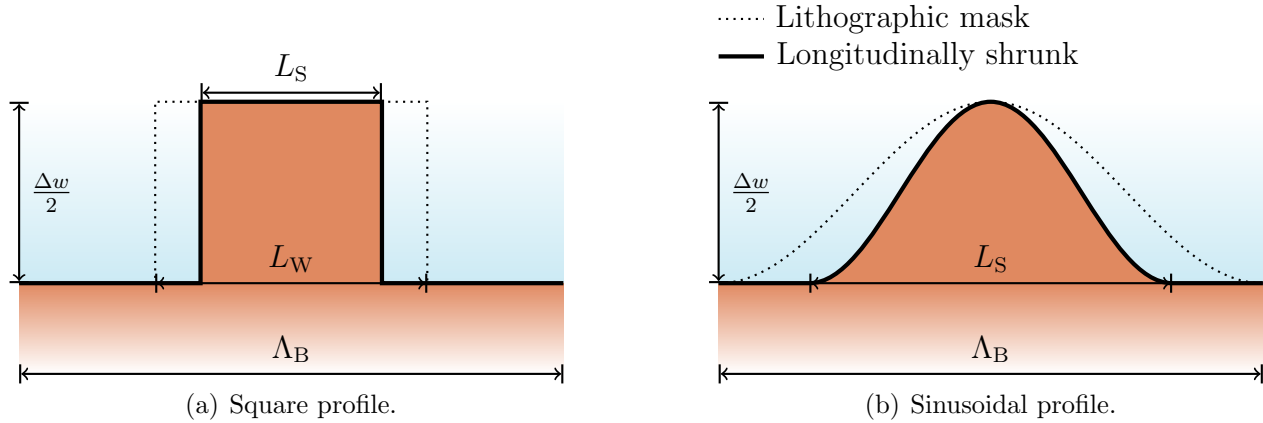


**Fig. 3.4** Longitudinal shrink adaptations to the simulation model of the SiN WBG.

In both of the profiles we can consider the Duty Cycle to be comprised of  $DC = \frac{L_S}{\Lambda_B}$ , the difference being that, before any shrinkage imposed by the fabrication variations, the original Duty Cycle of the square profile is 0.5, whereas for the sinusoidal profile it is 1.

These are the assumptions we are assuming for the analysis and for improving on the BG simulation model. We will evaluate the most reasonable fabrication variations and see

which ones will best fit the simulated to the measured results. Ideally, we would use these estimated variations to design new devices accounting for them. That would allow us to verify the improvements to the model. This proposed process is illustrated in Fig. 3.5, which is built over the process illustrated in Fig. 2.9.

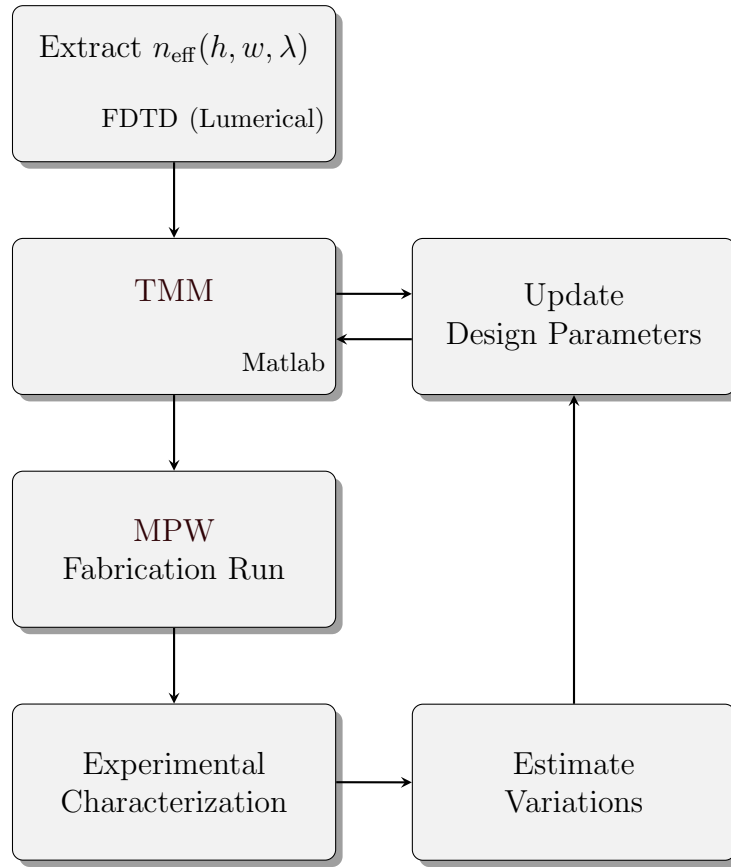


**Fig. 3.5** Iterative process of improving the BG simulation model.

### 3.5.2 Simulated Results

We have simulated the BGs using the process described in section 2.2 and illustrated in Fig. 2.9, *i.e.*, we have used the measured refractive index curves, which is shown in Appendix A.1, to simulate the effective index as a function of the waveguide dimensions using 2.5D

FDTD (Lumerical MODE analysis). The effective index curves are then imported to the TMM simulations. The Matlab script that simulates the devices is shown in appendix A.2.

As described in Eq. 2.25, when the Bragg grating is uniform, *i.e.* not apodized, the transfer matrix that describes the behaviour of the total grating can be computed by  $T_p^N$ . In other words, by raising the transfer matrix of one Bragg period  $T_p$  to the power of the number Bragg periods  $N$ . Since the structures fabricated are all apodized, the TMM simulations need to compute the transfer matrices for each individual Bragg period and apply the matrix product. Although the simulations take considerably more time to compute, this allows us to also consider other types of variations in the grating, as will be discussed in the following sections.

Figure 3.6 shows the comparison between the simulation curves and the characterization results of the same device shown previously in Fig. 3.2. These simulations use the parameters used in the layout submitted for fabrication, without any correction and use the square profile. We've used the relative wavelength instead of the absolute in this particular Fig. to better compare the curves' shapes and BW.

We can see that the simulated BW matches the characterized better for the TM mode. For the TE mode, the simulated BW is much wider than the characterized. Qualitatively evaluating the mode profiles in the gratings can help shine some light on the reasons for this and other discrepancies. Fig. 3.7 shows the power profile from both a top view perspective and cross-section for both TE and TM polarization modes. They show the absolute square of the electric field because it is more impacted by the refractive index change of the propagating material. We can see that in both perspectives the TE mode concentrates the signal more in the middle of the waveguide and spreads more horizontally, while the TM mode is more

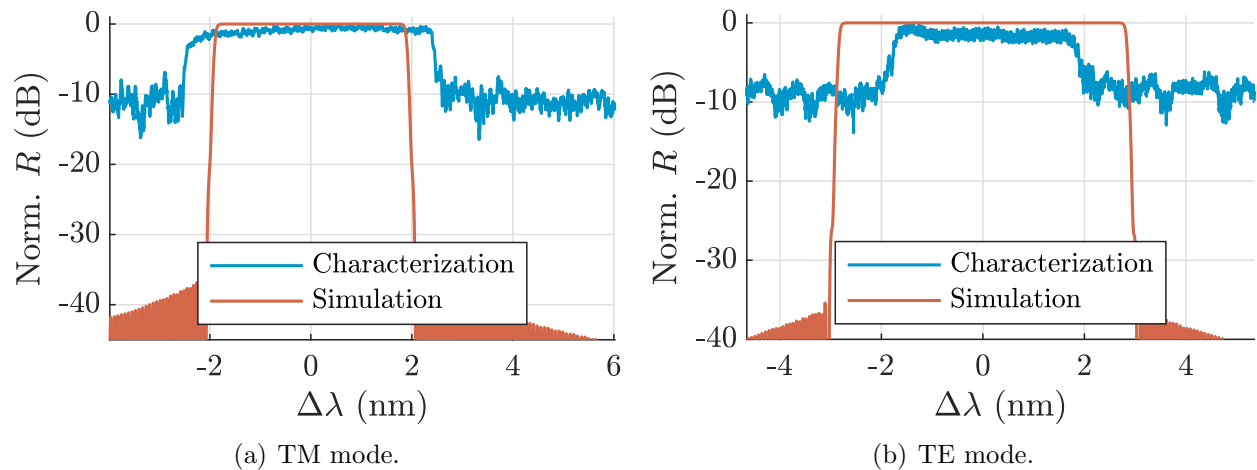


**Fig. 3.6** Comparison between simulation and characterization results in the reflection spectrum for both polarizations.

evenly spread inside the cross-section, and that a significant portion of the signal travels on the top and bottom surfaces of the waveguide.

One of the possible reasons for the divergence between characterized and simulated BWs could be the rounding of the corners in the gratings, and simulating different grating profiles can help us evaluate this. Fig. 3.8 shows the results using both square and sinusoidal profiles. We can see that the simulated square profile yields wider BW than the sinusoidal profile. We can also see that the Bragg wavelength is not impacted by changing the grating profile. The change to a square profile would generally increase the simulated BW. This would increase accuracy for the TM mode BWs, but diverge the simulated results from the characterizations in the TE mode. Therefore, it is unlikely that rounding in the corners is fully responsible for the divergence between measured and simulated results.

Fig. 3.8 shows a qualitative comparison, but it is important to make a more general analysis of the adaptations to the model. We will focus on Bragg wavelength and BW separately. Fortunately, for such a long WBG – 20,000 periods, the resulting BW and

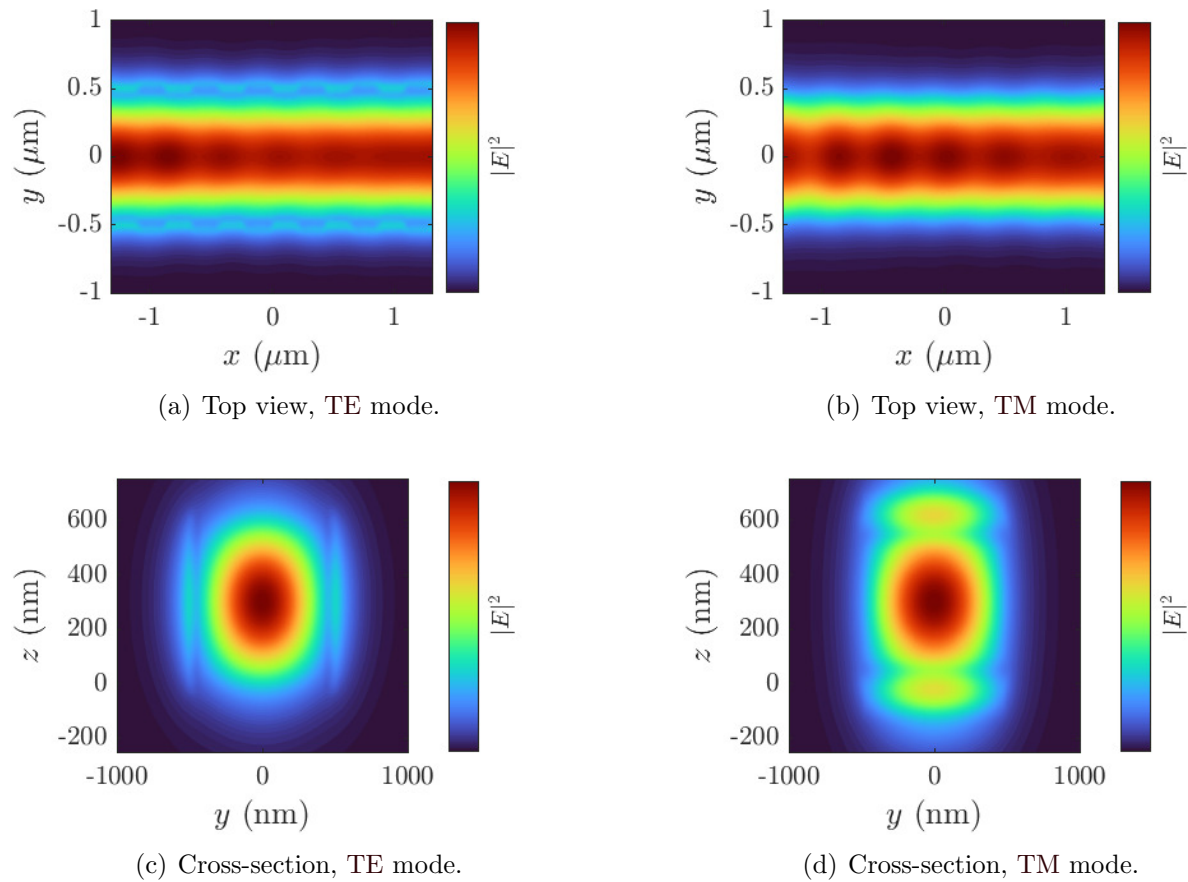


**Fig. 3.7** Power profiles of the SiN WBG from a top view perspective and cross-section for both polarization modes.

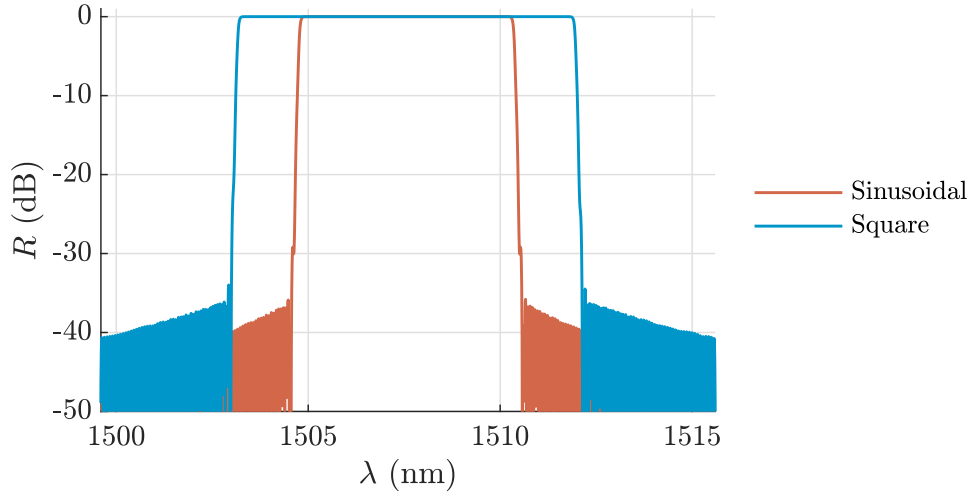


**Fig. 3.8** Profile comparison of simulated results.

Bragg wavelength are impacted mostly by separate parameters, which allows us more easily evaluate them. Namely, the Bragg wavelength is mostly impacted by the Bragg period  $\Lambda_B$  and cross-section waveguide dimensions, and the BW is more impacted by changes in the grating strength, *i.e.* duty cycle and general grating profile changes.

### 3.5.3 Bragg Wavelength

In the designing process of WBG, we establish that the most direct parameter that controls the Bragg wavelength of reflection is the longitudinal Bragg period  $\Lambda_B$ . However, it is important to establish the (in)dependence on other parameters.

Fig. 3.9 shows the Bragg wavelength as a function of the corrugation depth. It shows the characterized results for both the TE and TM in purple and dark red circled markers, respectively. The simulated Bragg wavelengths for the TE mode using sinusoidal and square profiles are shown in lighter and darker blue shades (or down-pointing and up-pointing

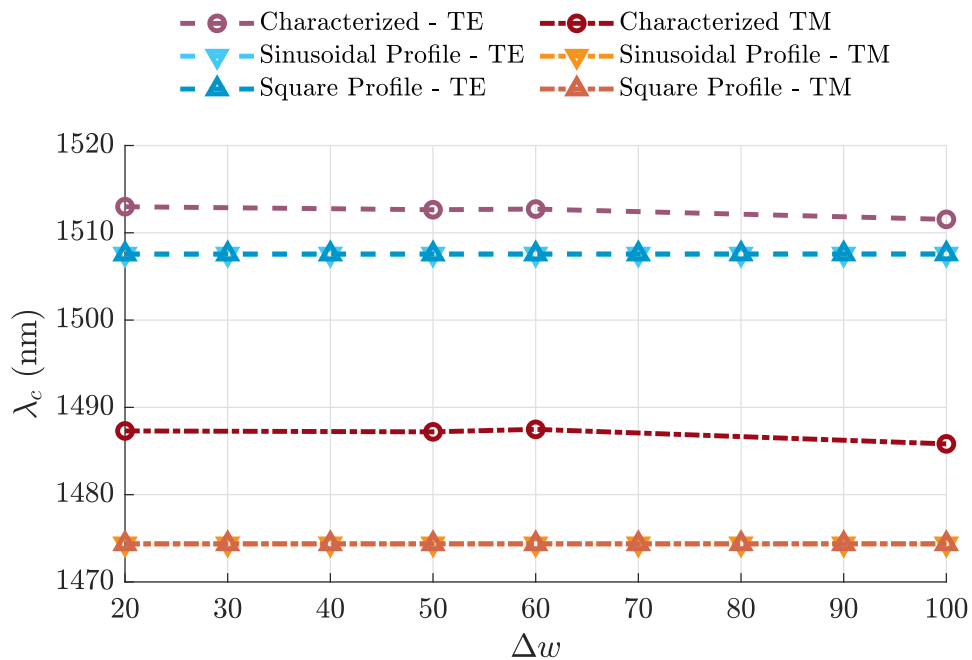


**Fig. 3.9** Bragg wavelength  $\lambda_B$  as function of corrugation depth  $\Delta w$ .

triangle markers), respectively. The same happens for the TM mode simulations, however using orange shades.

These results establish a few points. Firstly, the change in the grating profile has no significant impact on the Bragg wavelength for either polarization mode or grating profile, as anticipated in Fig. 3.8. Also, the resulting Bragg wavelength seems considerably constant as a function of corrugation depth. This is because the  $n_{\text{eff}}$  to  $w$  curve around the 1  $\mu\text{m}$  wide waveguide is close to a linear curve for a corrugation depth  $\Delta w$  of 100 nm at most, as shown in Fig. 2.5. This means that the average effective index  $n_{\text{avg}} = \frac{n_1+n_2}{2}$  is maintained for the given  $\Delta w$ .

We can also see in Fig. 3.9 that the characterized Bragg wavelength is higher than in the simulation for both polarization modes. This brings us to the modifications we can consider for the simulation model so that we can find better matching simulated results. Since the

Bragg wavelength is constant for varying corrugation depths  $\Delta w$ , it is possible to average them for analysis.

Fig. 3.10 shows the average Bragg wavelength for the TE mode on the horizontal axis and the TM on the vertical axis for a series of modifications to the simulations. The legend organizes the results by showing the cross-section dimension  $h \times w$  followed by a comment. The characterized Bragg wavelength is the red circle on the top-right and serves as a reference. The average of the original simulations using the device parameters, with average waveguide width of 1000 nm and thickness of 600 nm is shown with a blue down-pointing triangle to the right of the center, listed as 600nm  $\times$  1000nm. We can see that it is approximately  $-5$  nm away from the characterized results for the TE mode and  $-13$  nm away for the TM mode.

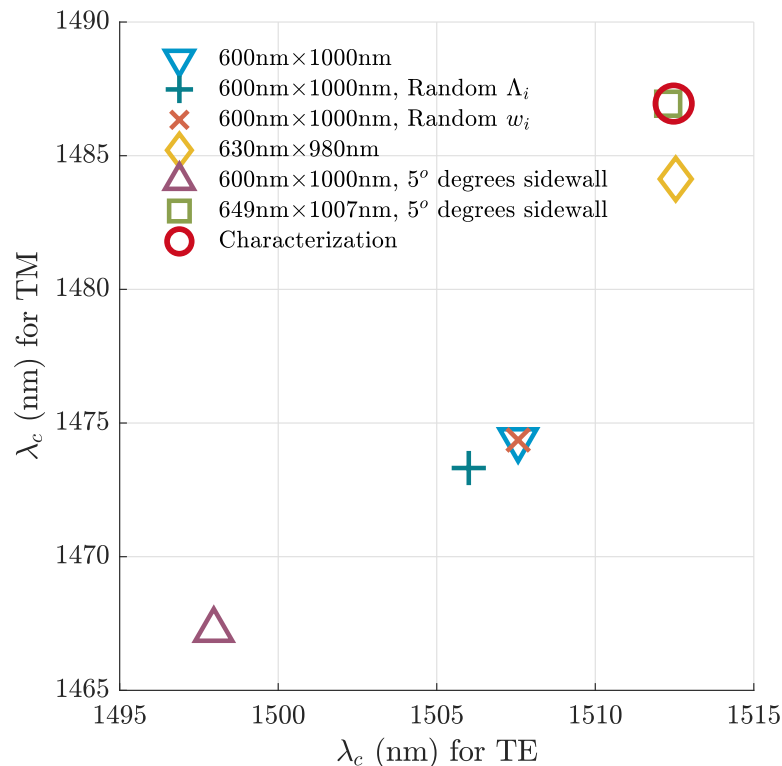


**Fig. 3.10** Average Bragg wavelengths for TE and TM modes.

By adding the  $5^\circ$  sidewall angle change to the simulation, we find the simulated Bragg wavelength plotted as a purple triangle marker. The Bragg wavelength was significantly decreased for both polarization modes.

We have simulated the WBG with a uniformly random variation on the widths  $w_1$  and  $w_2$  of each subsection of the Bragg periods, with a variance of 1 nm, which was the lithographic resolution used in fabrication. The result is shown as an orange cross and it is located on top of the blue triangle, listed as  $600\text{nm} \times 1000\text{nm}$ , Random  $w_i$ , where  $w_i$  is the width of the  $i^{\text{th}}$  subsection of the WBG. As already established, the corrugation depth does not have a significant impact on the Bragg wavelength and, thus, random variations to the width should also not impact the Bragg wavelength. The overlap of the simulated reflection and transmission curves with and without random variations in the widths confirms the independence between the parameter and the result.

Longitudinal random variations (with the same variance of 1 nm), however, show a small impact on the wavelength center. The result is shown as a green cross and is listed as  $600\text{nm} \times 1000\text{nm}$ , Random  $\Lambda_i$ , where  $\Lambda_i$  is the length of the  $i^{\text{th}}$  Bragg period. The longitudinal random variations have reduced the wavelength center by about 2 nm. However, this difference does not help determine the cause of the simulation to characterization divergence in Bragg wavelength.

The Bragg wavelength equation of the Bragg grating, shown in Eq. 2.8, relates the Bragg wavelength to the physical dimensions of the structure. It is established that longitudinal random variations do not explain the divergence. A deterministic longitudinal variation would cause the overall length of the WBG to significantly change, and so the parameter  $\Lambda_B$  in Eq. 2.8 is not the most likely responsible for the divergence. This leaves us with  $n_{\text{eff}}$ . As put in subsection 3.5.1, we assume that the refractive index acquired via ellipsometry is

accurate. Therefore, the most likely responsible for the divergence is the average cross-section dimensions of the structures.

From Eq. 2.8 we can determine the required effective index of both polarization modes that would result in the characterized Bragg wavelengths. We also know that the waveguide width has a larger impact on the effective index for the TE polarization, and the thickness has a larger impact on the effective index for TM. We can use a Particle Swarm Optimization (PSO) algorithm [101, 102] to find the waveguide dimensions that match the effective index of both TE and TM modes simultaneously with the ones estimated from the Bragg wavelength ( $n_{\text{eff}} = \frac{\lambda_{\text{B}}}{2\Lambda_{\text{B}}}$ ). PSO is a built-in feature of the Lumerical suite. Therefore, a deep understanding and a from-scratch implementation of the algorithm are not needed. All we need is to set as the tuning parameters the waveguide width  $w$  and thickness  $h$ , and to minimize a Figure of Merit (FOM) that is determined as the absolute difference between the simulated effective index and the estimated effective index from the Bragg wavelength. That is, the PSO algorithm finds a width  $w$  and thickness  $h$  that minimizes the FOM determined in Eq. 3.1, where  $n$  is the simulated effective index and  $\hat{n}$  is the estimated effective index calculated from  $\lambda_{\text{B}}$ , and the subscript indicates the polarization mode.

$$\text{FOM} = |n_{\text{TE}} - \hat{n}_{\text{TE}}| + |n_{\text{TM}} - \hat{n}_{\text{TM}}| \quad (3.1)$$

Using this process we have found the results shown as the yellow diamond marker with 630 nm  $\times$  980 nm cross-section, and the green square marker with 649 nm  $\times$  1007 nm and 5° sidewall angle. We can see that these are the two simulated results that are closer to characterizations.

### 3.5.4 Bandwidth

The bandwidth is most impacted by changes in the grating shape. The characterized results and the simulations of the original layout using both types of grating profiles are shown in Fig. 3.11. The simulated results show varying BW slopes as a function of  $\Delta w$  depending on the grating profile and polarization mode, but all are linearly distributed. The characterized BWs, on the other hand, are not linear. Moreover, the BWs for the TM polarization mode is consistently higher than for the TE, which is not the case for the simulated results.

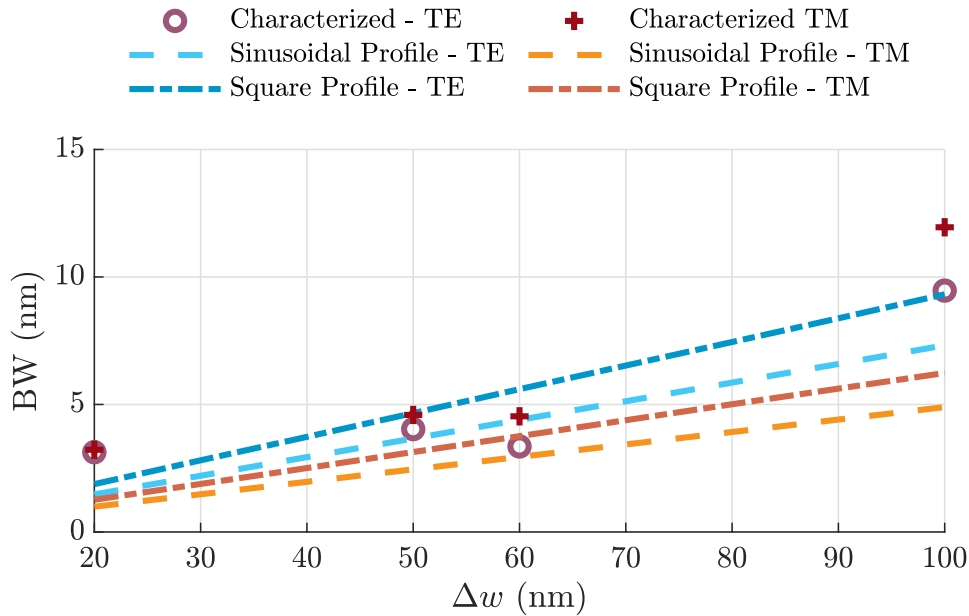


**Fig. 3.11** Bandwidth as a function of corrugation depth.

Generally, there are two main parameters in the WBG design that control the BW, the total structure length  $L = N_G \Lambda_B$ , and the corrugation depth  $\Delta w$ . Since all the structures we are using have the same number of periods  $N_G$  and total length  $L$ , the only parameter left is the corrugation depth  $\Delta w$ . However, we established as a presumption the fact that shrinkage would not impact the corrugation depth, as illustrated in Fig. 3.3. Therefore,

we need to adapt the model to include a parameter that controls the grating strength. By incorporating the longitudinal shrinkage, such as elaborated in Fig. 3.4, we can achieve that.

Fig. 3.12 shows simulated results for BW as a function of corrugation depth  $\Delta w$  with increasing longitudinal shrinkage and, thus, decreasing duty cycle, for both the square and sinusoidal profiles. The blue curves show the simulated results for the TE polarization mode and the orange curves for the TM mode. The darker shades of dashed-dotted curves show the simulated results using the square profile, while the lighter dashed curves use the sinusoidal profile. The simulation of the squared profile have consistently higher BW than the sinusoidal profile. In terms of polarization, the simulated TE mode consistently shows higher BW than TM, which is not true in the characterized results. As we can see, the addition of the Duty Cycle as a model parameter offers good control over the grating strength (the slope of the curves).

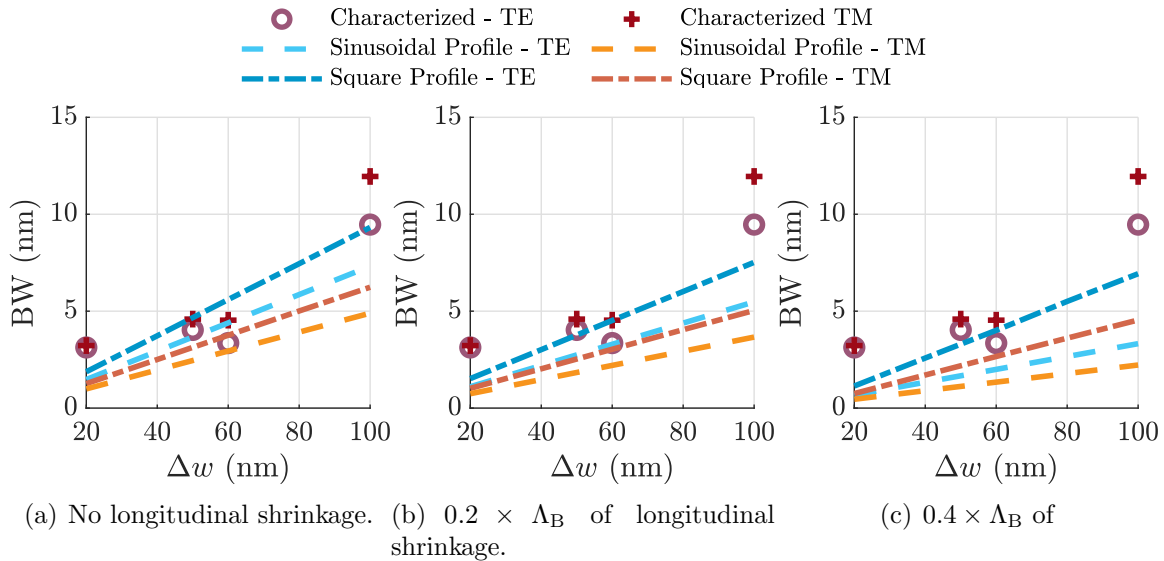


**Fig. 3.12** Effect of Duty-cycle on BW. Captions show the amount of longitudinal shrinkage.

According to [103], square and sinusoidal profiles should show a similar grating strength

up to  $\Delta w = 100$  nm in SOI, at which point the square profile should show over perturbation of the index while the sinusoidal profile should still show increasing grating strength. Since SiN has a lower refraction index than SiN, we should not expect over-perturbation of the index profile at  $\Delta w < 100$  nm, so this does not explain the higher TM BW than for TE. However, there are still other fabrication variations that we can consider in the BW analysis, as we did with the Bragg wavelength analysis.

In the results shown in Fig. 3.11 we can also see that the *characterized* BW to corrugation depth function does not seem to be a linear relation – there seems to be a vertical shift to a lower slope function. There may be a transversal shrinkage that is a function of the corrugation depth. In other words, the larger the corrugation depth, the stronger the transversal shrinkage.

Because the wavelength center was considerably constant as a function of corrugation depth, it was possible to visualize the results as averages. However, this is not the case for BW. It tends to behave as a linear function of corrugation depth, so a more qualitative approach to the analysis is better. Fig. 3.13 shows the BW curve as a function of corrugation depth for several types of fabrication variations. Similarly to the previous BW curves, the blue shaded curves show results for TE and orange for TM, darker dashed-dotted curves show results for the square profile and lighter for sinusoidal.

The characterized results that are also shown in all curves for better comparison. We can see that the characterized BW span from around 3 nm up to 12 nm for the TM polarization in the corrugation depth range analyzed, and 3 nm up to 9 nm of BW for the TE polarization. Fig. 3.13(a) shows the simulated results for the structure with the same thickness and width as the original design ( $600 \times 1000$  nm<sup>2</sup>), but including a sidewall angle of  $5^\circ$ . We can see

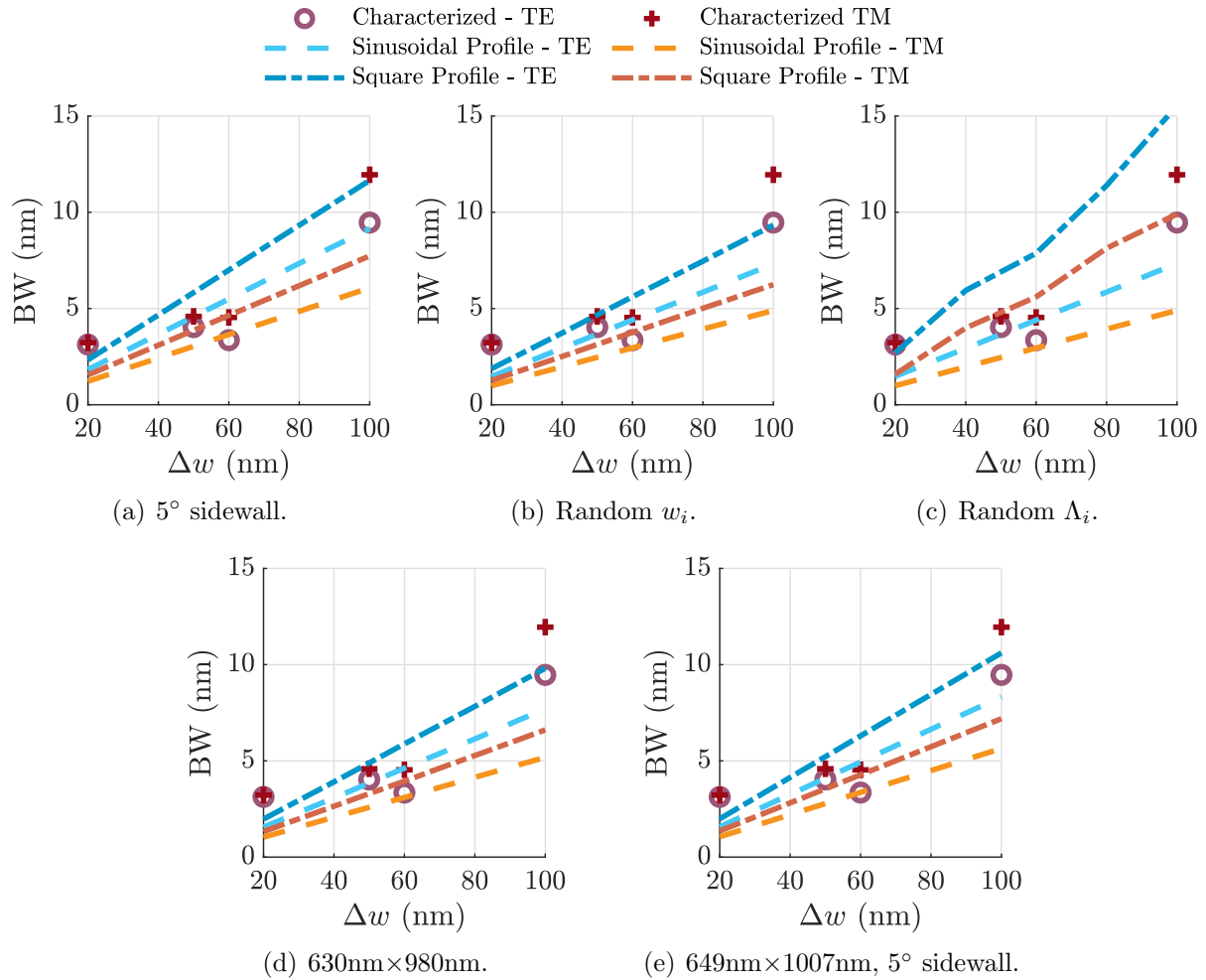


**Fig. 3.13** Bandwidth as a function of corrugation depth for different types of fabrication variations.

that the BW curve increases slope in both polarization modes, which increases accuracy for the TM mode, but overshoots for the TE.

Fig. 3.13(b) shows the results considering uniformly distributed random variations in each of the widths  $w_i$  of the  $i^{\text{th}}$  subsection of the SiN WBG around the lithographic resolution of 1 nm. No significant change from the results in Fig. 3.11 can be seen. This is likely because the uniform variations have a zero mean, and the great number of periods makes the positive variations statistically cancel out the negative variations.

In Fig. 3.13(c) we see the results with uniformly distributed random variations to the  $i^{\text{th}}$  Bragg period  $\Lambda_i$ . These are the only simulated results that break the linearity of the BW-to- $\Delta w$  slope but only for the square profile. The random variations in each Bragg period increase significantly the BW for the square profile, and yield the best accuracy for the TM polarization mode.

Figures 3.13(d) and 3.13(e) are the two simulations that come from the Bragg wavelength analysis in subsection 3.5.3, and they consider changes in the cross-section dimensions of the average waveguide structures determined by the PSO algorithm. They both yield similar results in terms of BW, although the  $5^\circ$  waveguide sidewall angle of Fig. 3.13(e) has a slightly larger slope. Fig. 3.13(e) shows the simulation that yielded the best results in the Bragg wavelength analysis since its PSO algorithm ran for the longest period. We can see that the results of BW did not significantly change from the results shown in Fig. 3.13(a), although a slightly lower BW to corrugation depth slope. The lower slope is likely due to the higher average effective index from the larger cross-section. The same corrugation depth means a lower change in the effective index for each mode with the larger cross-section.

If the reason that the characterized BW in the TM polarization mode was consistently higher than TE while the opposite was true for simulated results was because of fabrication

variations, the most likely explanation for the divergence is that the simulations assumed the waveguide has perfectly flat top and bottom surfaces. Moreover, the rounding of the corners is a three-dimensional phenomenon, and the change from square to the sinusoidal profile does not fully capture such variation. A vertical variation in the corners is reasonable and would likely impact more the BW of the TM mode than the TE. Moreover, if the SiN shrinkage imposes a thickness variation that is periodical with period  $\Lambda_B$ , we should expect a BW increase for the TM mode. In other words, if the material shrinkage makes the narrower section of the BG period have a slightly smaller thickness than the wider section, this would also impact more the TM mode than the TE. This is corroborated by the mode profile distribution shown in Fig. 3.7, where the TM mode profile distribution is more concentrated in the top and bottom surfaces. However, we should not expect a thickness variation greater than 0.1 nm [100], which is a variation that is too small to impact the BW so drastically. Further analysis is needed to explain the exact reason for the BW divergence, and also for the nonlinear behaviour in the BW-to- $\Delta w$  measured curve.

### 3.6 Conclusion

We have improved the simulation model to better match the simulated results with the characterized results in both Bragg wavelength and BW, although the peak reflectivity measurements were compromised. For the devices tested in this work, the model has fairly independent parameter control over BW and Bragg wavelength. The waveguide cross-section average dimensions have a great impact on the Bragg wavelength, whereas the longitudinal shrinkage, parametrized by the inclusion of a duty cycle, has a greater impact on BW and no significant impact on the Bragg wavelength. The addition of a waveguide sidewall angle has an impact on both measurements. It reduces the effective index (and consequently the Bragg

wavelength) and increases the BW. The addition of a duty cycle to the model, whichever grating profile is used, allows us to account for grating strength in simulation, which will help us to better plan for future fabrication runs.

Our analysis of Bragg wavelength and average effective index lead us to the possibility of having a much larger waveguide cross-section than what was lithographically etched. This is unlikely to be happening with fabricated devices. The lithographic resolution in the fabrication process is 1 nm, which is currently a state-of-the-art resolution. SiN is known to shrink by about 50 nm in width. Our original layout had average waveguide width of 1000 nm and our analysis found a width of 1007 nm. Although the divergence is not extraordinary from the original layout, SiN does shrink, so an expansion is unlikely. Moreover, the expected variation in thickness after the LPCVD of SiN on the Si wafer is 3%, whereas we found around 8% of thickness increase. Such a significant increase raises the possibility that there might be other reasons for the divergence between simulation and characterization, such as an inaccurate refractive index curve measurement from the ellipsometry.

We have presented the presumptions we made at the start of our analysis, such as assuming the accuracy of the refractive index used, and that the thickness is constant throughout the entire structure. These should be reasonable assumptions for the analysis since the TMM simulation model is widely used although it has its limitations, and simulating an almost 1 cm long apodized structure using FDTD is currently very challenging. However, there is a possibility that the refractive index measurement is not as accurate as we expected, especially because the measurement was done prior to fabrication at another wafer. Moreover, the assumption that the thickness is constant helps to model the WBGs using TMM, but it is not reasonable to expect that the shrinkage characteristic to SiN would constrain itself only to the horizontal direction, leaving the top and bottom waveguide surfaces perfectly flat. It is also possible that the simulation software is responsible for these inaccuracies.

Because we used edge coupling instead of VGCs, we were able to characterize both polarization modes simultaneously. This is the reason why the simultaneous analysis of both modes is rare in the literature – where VGCs are usually used. Although we were unable to fully replicate the BW divergence for both modes, we have introduced the duty cycle as a parameter for the gratings, which can be used to more accurately tune the BW-to- $\Delta w$  for a single polarization mode at a time, with negligible impact on the accuracy of the Bragg wavelength. We saw that the waveguide sidewall angle had a significant impact on the bandwidth. Perhaps the modal divergence is due to some other geometric asymmetry that we have not considered, such as an uneven shrinkage as a function of the transversal position in the waveguide. Nonetheless, further analysis is needed to accurately replicate the BW results in both modes simultaneously.

In truth, the fabricated WBG are probably subject to, not just thickness variations or a refractive index divergence, but in fact, many of the fabrication variations we have hypothesized (and probably others) simultaneously. New fabrication runs will allow us to better determine which of these variations is more responsible for the divergences in the results. This will become easier to test now that SiN is becoming more available at MPW run options, such as with ANT. Determining with more precision the variations that happen in the fabrication process is critical for the successful design of such delicate components as photonic devices.

For future works, the corner rounding in the gratings can be further analyzed. Moreover, other fabrication variations, such as different material shrinkage modellings, might help explain the divergences between simulated and characterized results. Full 3D FDTD using both periodical boundaries cannot simulate the grating with the specific length as the fabricated device, but it might be more accurate and facilitate the simulation of the grating variations that would be challenging to model with TMM.

The lack of an available PDK for the SiN platform is only a temporary issue. Several devices have recently been demonstrated, such as VGCs [104–106], WDM (de)multiplexers [107,108], PBSs [109–111], and Add/Drop multiplexers [112]. Moreover, SiN waveguides have achieved propagation losses of  $< 1$  dB/m with a significant transparency range between 400 nm and 2350 nm [44].

It has become hard to see a future where SiN has no place in integrated photonics. As the platform becomes more available with further adoption, it will become important to improve the simulation models for these devices. We have here started this work on WBG structures, and that will help shine an early light onto the various issues that the fabrication variations might bring to devices built using this platform.

## Chapter 4

# Sampled Subwavelength Grating Waveguide Bragg Gratings

### 4.1 Introduction

The control of wavelength response is a fundamental building block of devices used in SiP. There are many photonic wavelength-based filtering devices, such as the MZI, and the MRR, that rely on phase interference, which might require thermal tuning. For purely passive devices, it is sometimes important to specify the filtering wavelength, which BGs allows us to do. However, BGs only have one reflection band. Sampled BGs allows us to replicate the reflection band with pre-determined wavelength spacing.

The Sampled FBG is a well studied device that has been demonstrated not only using uniform sampling but with several more complex sampling functions, such as chirped-sampled FBGs [113, 114], sampled-chirped [115], strongly chirped sampled FBGs [116, 117],

and phase-shifted [118]. Many applications of these structures have been found even before the integration effort with SOI. Sampled FBGs have been used, for example, in WDM systems as add/drop multiplexer [73], simultaneous sensors for temperature and refractive index [60], multiwavelength Raman fibre lasers [119], pulse multiplication (from 10 GHz to 40 GHz) [120], and in the detection of aliasing in spectrometers [121].

Naturally, with the effort of integrating photonic devices, sampled WBG have found renewed interest and applications. These structures have been demonstrated and analyzed in SOI [63] and chalcogenide ( $\text{As}_2\text{S}_3$ ) [60]. In this context, they have been applied as integrated add/drop multiplexers for WDM systems [122], and also in multiwavelength lasers using a III-V/SOI hybrid platform [123]. Moreover, an anti-symmetric version of the sampled SWG-WBG can suppress the 0th-order resonance while maintaining the  $\pm$  1st-order resonances [124].

The sampled WBG is also a relevant structure in the application and study of random gratings. Although the fabrication process imposes several random variations to SOI structures, sampled WBG allows us to randomize parameters that are undoubtedly deterministic, such as the number of SWG periods in the uniform waveguide or BG subsection of the device. A noteworthy use of random sampled WBG is in the generation of pseudo-random and chaotic waveforms with high time-bandwidth product [74, 125]. Another application of random gratings is in random lasers, which can be based on natural Rayleigh scattering in glass, but more reliably on random gratings [126–131].

The versatility brought by using SWG as a building block has found many applications, including in BG structures [83–85, 132–134]. The construction of sampled WBG using SWGs structures has shown polarization-independent operation [135], however, the device requires a two-step deposition/etching process, since it uses rib-waveguides.

In this chapter, we employ SWG to construct sampled WBGs. One important motivation for using SWG with loading segments to build the WBGs is that it might allow us to explore a polarization-insensitive version of the device by employing tilted SWG waveguides [133,136]. Moreover, these structures only require a single etching step in fabrication. We present the device in both uniform and random versions.

## 4.2 Uniform Sampled SWG-WBG

### 4.2.1 Design and Layout

As previously commented, the BG is built upon a periodically changing effective index in a waveguide. The method we employ to achieve this with SWG-based waveguides is by placing loading segments beside the main SWG waveguide segments with periodically changing gap distances [85], first introduced by [83]. This is illustrated in Fig. 2.14. The sampled BG is built by intersecting uniform waveguide sections between BGs sections, as illustrated in Fig. 2.10.

In the same way that WBG can be built using SWG waveguides with loading segments, we can also construct sampled WBG using SWG. Fig. 4.1 shows the cross-section in (a), the schematic parameters of the sampled SWG-WBG in (b), and a top view of the complete PIC in (c), including SWG tapers and VGCs. The cross-section in (a) shows the thermally grown Buried Oxide (BOX) in the lower portion and the deposited dioxide clad on the upper portion of the device. In between the two layers of dioxide, we see three Si segments; the middle segment has width  $w$  and thickness  $h$ , while the loading segments have the same thickness  $h$ , but their widths and lengths are  $l_{\text{SWG}}$ . In the schematic in (b), we can see

that the main SWG segments have width  $w$ , length  $a$  and periodicity  $\Lambda_{\text{SWG}}$ , comprising the SWG duty cycle  $DC_{\text{SWG}} = \frac{a}{\Lambda_{\text{SWG}}}$ . We can also see the sampling taking place by cascading a section of BG of length  $L_{\text{BG}}$  with a section of SWG waveguide of length  $L_{\text{WG}}$  and, by consequence, comprising a sampling duty cycle of  $DC_{\text{Sample}} = \frac{L_{\text{BG}}}{\Lambda_{\text{Sample}}} = \frac{L_{\text{BG}}}{L_{\text{BG}}+L_{\text{WG}}}$ . The BG section periodically changes the effective index by placing the loading segments with two gap distances,  $g_1$  and  $g_2$ , with periodicity  $\Lambda_{\text{BG}}$ . Note that the SWG uniform waveguide section also includes loading segments. This is done to control the effective index of the waveguide section reducing reflection in the transition between sections and also reducing FP interference.

#### 4.2.2 Design and Layout

We have constructed several versions of the device, and in order to compare the results, we have organized the order of the shown results as illustrated in Fig. 4.2, in which the dark red segments illustrate the WBG sections and the lighter red illustrates uniform SWG waveguides. The illustration only shows two sampling periods for each version, but in fact, our simulated and fabricated devices have 10 sampling sections. The accumulated length of the SWG-WBG sections remains the same for all the devices, but we change the length of intersecting SWG waveguides in between them. Consequently, we are iterating the sampling duty cycle  $DC_{\text{Sample}}$  of the structures.

The common parameters between all versions is shown in Table 4.1. We used the standard 220 nm Si film thickness. The width of 400 nm was used based on the literature device [83], and the fact that our group had previously successfully fabricated SWG-WBGs using this width [85]. During the design and simulation process, we planned to use  $g_1 = 450$  nm, but a small typographic mistake in the Python script that generated the GDS layout file set it

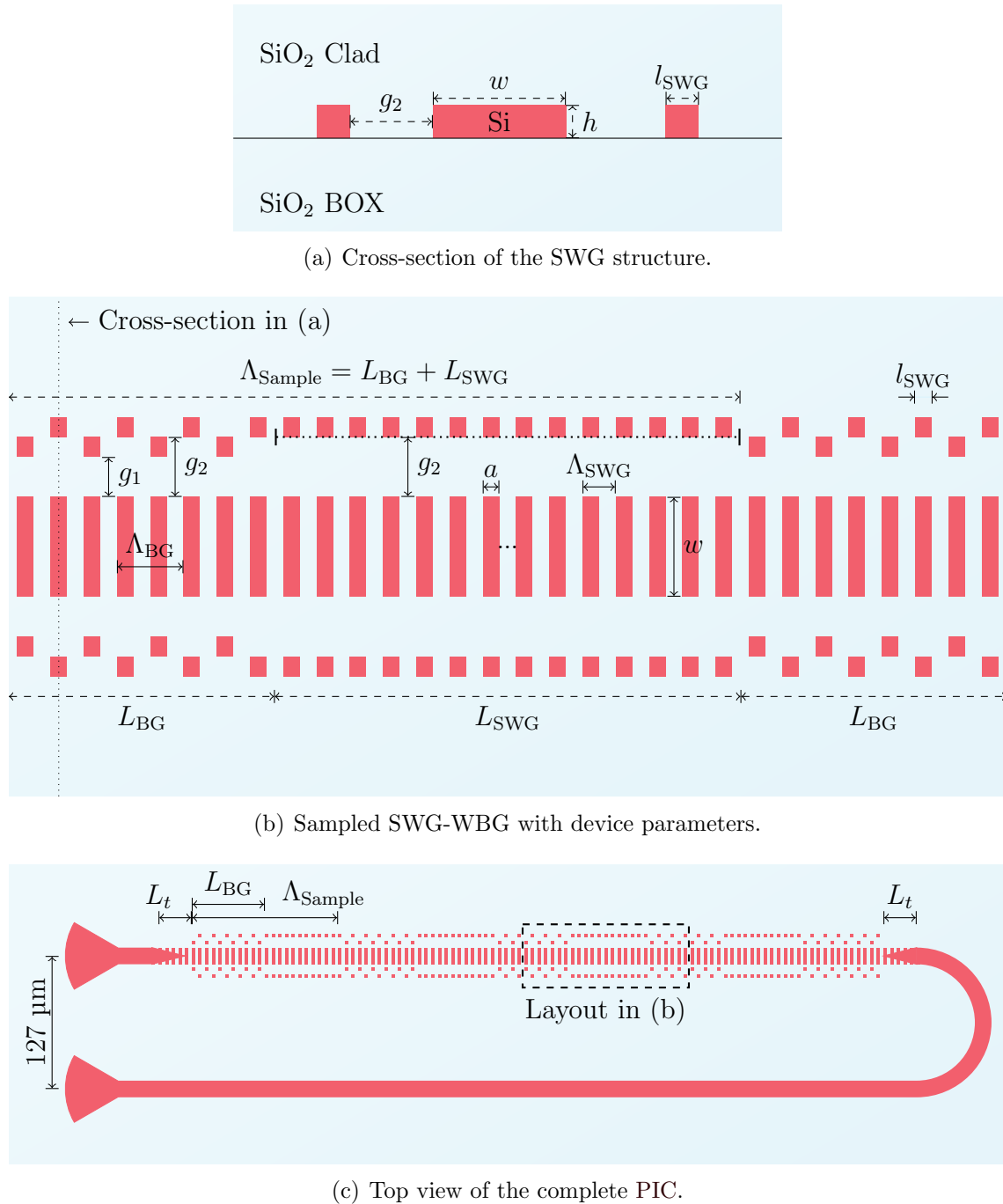


**Fig. 4.1** Layout and schematics of the device.

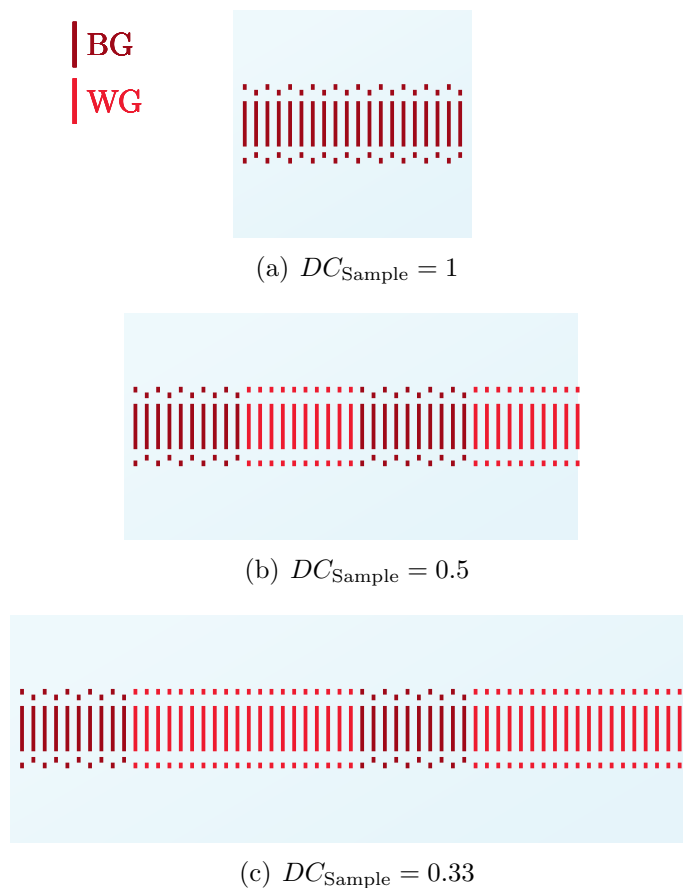


**Fig. 4.2** Order of results of the sampled SWG-WBGs.

to 449 nm. Fortunately, this imposes very little change to the effective index perturbation, and so we use 449 nm in the analysis as well. The gap distance  $g_2 = 500$  nm and, thus, the  $\Delta n$  of the Bragg structure, was empirically decided using simulated results as a reference, however, in more recent explorations we have found that such a difference in gap distance might create an effective index perturbation that is larger than ideal. Future fabrication runs will probe this hypothesis. The SWG periodicity  $\Lambda_{\text{SWG}} = 254$  nm and, consequently, the Bragg period  $\Lambda_{\text{B}} = 2\Lambda_{\text{SWG}} = 508$  nm (for symmetry), were decided based on the SWG condition  $\Lambda_{\text{SWG}} \ll \lambda$  (the SWG period has to be much smaller than the period of the propagating signal), and with intention of having the Bragg wavelength in the C-band. In

our experience, the characterized reflection band of SWG-WBGs consistently show a blue shift from the simulated reflection. The Bragg period  $\Lambda_B$  yields a simulated Bragg wavelength at 1565 nm, whereas we found the characterized Bragg wavelength at 1530 nm. The blue shift is likely due to fabrication variations, which will be discussed further. We have decided to use a SWG duty cycle  $DC_{\text{SWG}} = 0.5$  and, consequently,  $a = \Lambda_{\text{SWG}}DC_{\text{SWG}} = 127$  nm. The size and position of the loading segments control the effective index change of the SWG waveguide. We have decided to fix the size and vary the position for better fabrication accuracy. The segment size  $l_{\text{SWG}}$  is symmetric with  $a$ . The number of sampling sections  $N_{\text{Sample}}$  needs to be large enough to create the reflection band replicas but keeping in mind the available length in the SOI chip.  $N_{\text{Sample}} = 10$  was a good trade-off for the devices we decided to fabricate.

**Table 4.1** Common parameters between all sampled SWG-WBG versions.

$h$	$w$	$g_1$	$g_2$	$\Lambda_{\text{SWG}}$	$\Lambda_B$	$a$	$l_{\text{SWG}}$	$N_{\text{Sample}}$
220 nm	400 nm	449 nm	500 nm	254 nm	508 nm	127 nm	127 nm	10

Similarly to the SiN WBGs, the sampled SWG-WBGs can be simulated using TMM, as described in section 2.2. The SWG-WBG illustrated in Fig. 4.2(a) (not sampled) follows the same simulation procedure as the SiN WBGs, *i.e.* we use the effective index of the waveguide structure extracted from FDTD simulations to create the transfer matrixes and apply TMM to find the transfer matrix that describes the complete structure. In this case, instead of the waveguide width controlling the effective index, we have the gap distance of the loading segment, as illustrated in Fig. 2.15. Since there is no apodization taking place in our structures, the uniform version of Eq. 2.25 can be used, which is computationally much faster and more efficient. The uniform SWG waveguide in each of the sampling sections can be described with the homogeneous waveguide transfer matrix, as in Eq. 2.15. Once we have used the matrix product to account for the  $N_{\text{Sample}}$  cascaded sampling sections, the resulting

transfer matrix  $T_{\text{BG}}$  yields the response of the complete structure. The transmission and reflection curves can be extracted as in Eq. 2.26.

### 4.2.3 Results

The devices reported here were fabricated at ANT, which provided a PDK that included the design for the TE polarization optimized VGC that we used. As shown in Fig. 4.1(c), the VGCs were spaced 127  $\mu\text{m}$  away from each other, which matches the pitch of the 12-ports  $8^\circ$  Fibre Ribbon Array (FRA). Both the FRA and the chip were placed on top of manually controlled XYZ-stages.

The simulated and characterized results are shown in Fig. 4.3, 4.4, and 4.5. Figure 4.3 shows the result for a SWG-WBG with total length of  $L = N_{\text{BG}} \times \Lambda_{\text{BG}} = 5.08$  mm, *i.e.*  $N_{\text{BG}} = 10,000$ , and no intersecting waveguide sections and, thus, no sampling. The results show one single reflection band at the center of the wavelength response, and the BW of both the simulated and characterized results are similar, at approximately 1 nm. The transmission curve is reduced by over 50 dB at the Bragg wavelength in the simulated results, while it is reduced by around 25 dB in the experimental results. The simulation assumes the signal is absolutely TE polarized. In the characterized results, although we use VGCs that are optimized for the TE polarization mode, this does not ensure that the input signal is 100% TE polarized. Therefore, a portion of the signal being coupled into the characterized result is likely TM polarized, which will not reflect at the Bragg grating for the TE mode and, consequently, bring the transmission curve upward at the Bragg wavelength. Regarding the Bragg wavelength itself, in simulations, the reflection band was centred at approximately 1565 nm, whereas the characterized results were centred at approximately 1530 nm. The variation is likely due to fabrication variations in the SWG segments positions and, most

importantly, dimensions, since the etching step of the CMOS process can impact them significantly. Because of the difference in Bragg wavelengths, we use the shift from Bragg wavelength as  $x$ -axis  $\Delta\lambda$  instead of the absolute wavelength  $\lambda$ , which helps us compare the curves more effectively.

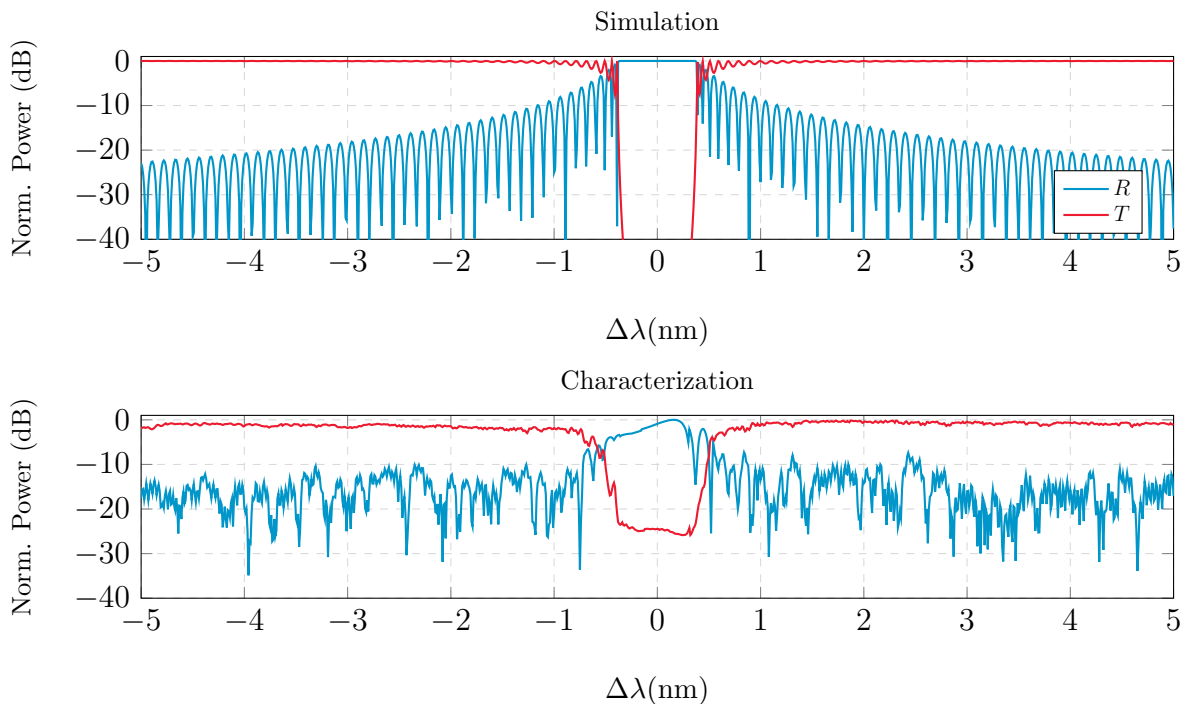


**Fig. 4.3** Uniform SWG-WBG (no sampling). Total length  $\approx 5$ mm.

Figure 4.4 shows the simulated and characterized results for a Sampled SWG-WBG with 10 sampling sections, in which the number of Bragg periods in each section is  $N_{\text{BG}} = 500$ , resulting in a Bragg grating section of length  $L_{\text{BG}} = 254 \mu\text{m}$ , and the number of SWG periods in the waveguide section is  $N_{\text{SWG}} = 1000$ , resulting in a uniform SWG waveguide section of the same length,  $L_{\text{SWG}} = 254 \mu\text{m}$ . The resulting sampling duty cycle is, thus,  $DC_{\text{Sample}} = 0.5$ , since  $L_{\text{BG}} = L_{\text{SWG}}$ . The anticipated spacing between the reflection bands is given in Eq. 2.27, which results in approximately 1.6 nm. The simulated and characterized

results show very similar spacing between the reflection bands, at approximately 1.2 nm. The reason for the difference from the anticipated wavelength spacing from Eq. 2.27 is the same reason for the wavelength shift between simulated and characterized wavelength responses. Because of fabrication variations there is likely a difference in effective index  $n_{\text{eff}}$  used in Eq. 2.27 from simulation to characterization. The simulation using TMM may have an overall wavelength shift, but it finds a more accurate spacing than the equation when compared with the characterized results. Another aspect to note is that the reflection band depth in the transmission curve is reduced in both simulation, which in Fig. 4.3 was above 50 dB of suppression and is approximately 35 dB in Fig. 4.4, and in characterization, which was around 25 dB of suppression in Fig. 4.3 and is around 20 dB in Fig. 4.4.

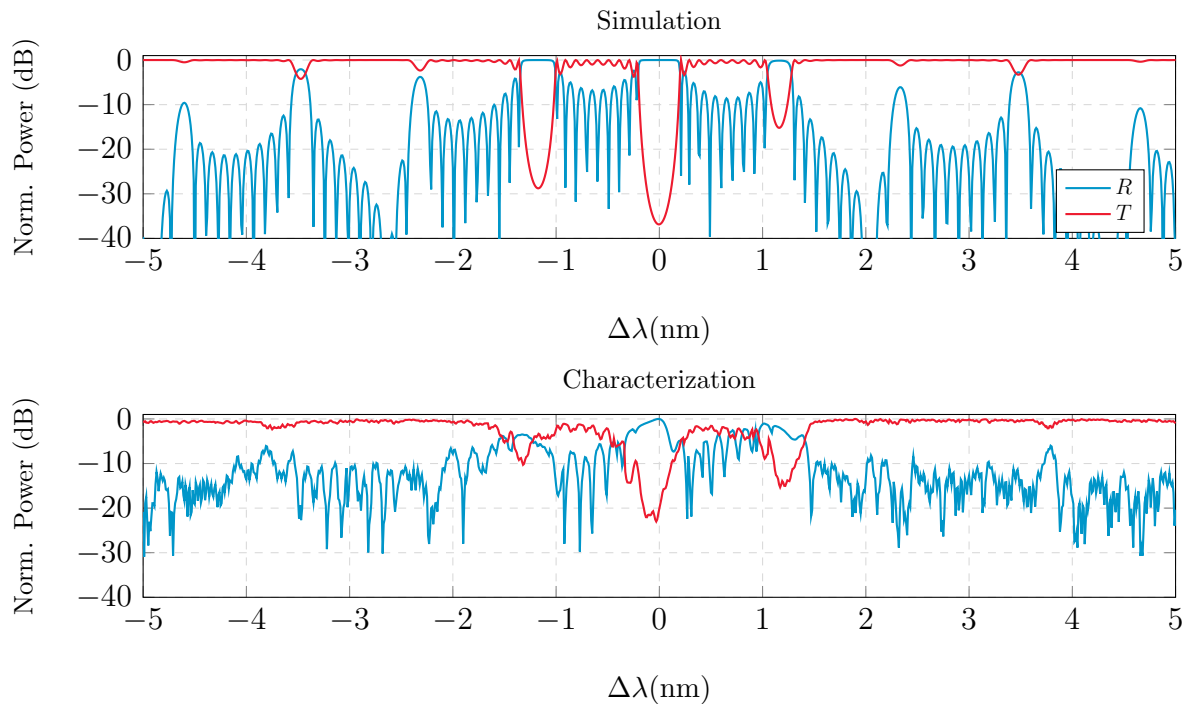


**Fig. 4.4** Sampled SWG-BG with 10 sampling sections of  $N_{\text{BG}} = 500$  and  $N_{\text{SWG}} = 1000$ . The sampling duty cycle is 50%.

In Fig. 4.5 we see the characterized results for a Sampled SWG-WBG with 10 sampling

sections, in which the number of Bragg gratings remains the same as the previous devices,  $N_{\text{BG}} = 500$ , but the number of SWG periods is increased to  $N_{\text{SWG}} = 2000$ . Consequently, the sampling duty cycle is now reduced to  $DC_{\text{Sample}} = \frac{1}{3}$ , since  $L_{\text{BG}} = 254 \mu\text{m}$  and  $L_{\text{SWG}} = 508 \mu\text{m}$ . We can note that the deepest reflection band in the transmission curve has a suppression of only around 15 dB, and we cannot clearly distinguish the reflection bands and the wavelength spacing, which merits further investigation.

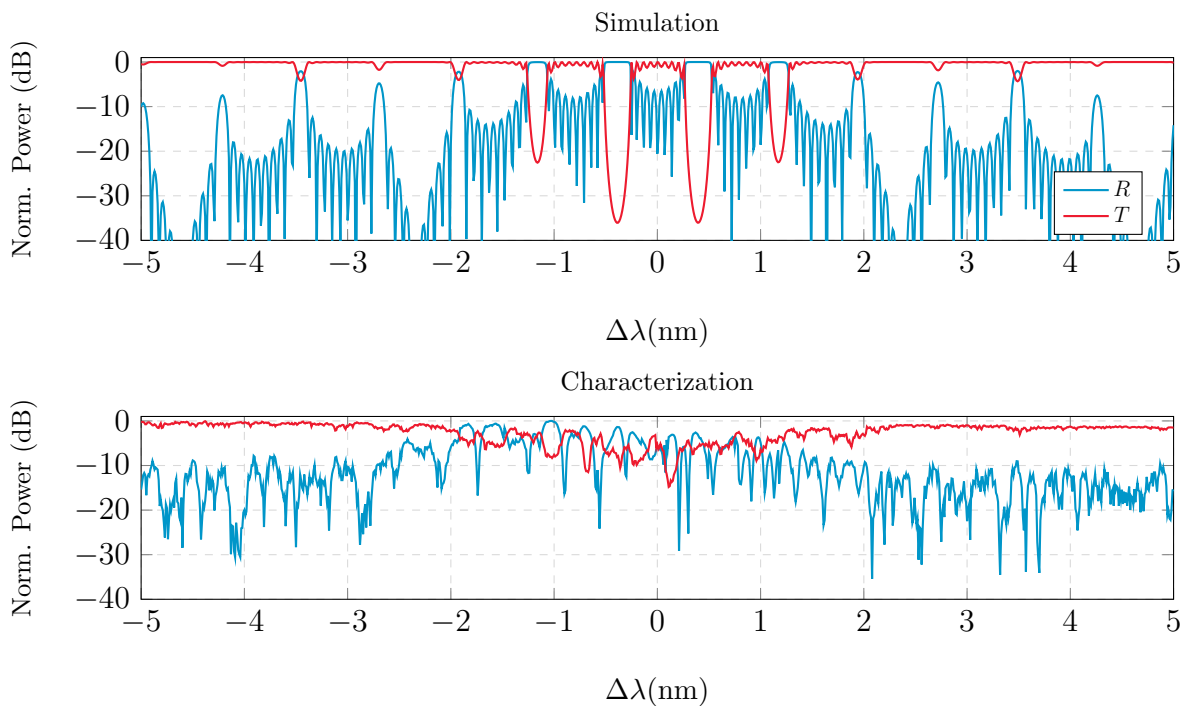


**Fig. 4.5** Sampled SWG-WBG with 10 sampling sections of  $N_{\text{BG}} = 500$  and  $N_{\text{SWG}} = 2000$ . The sampling duty cycle is 33%.

In Fig. 4.6 we can see simulated results considering either higher propagation losses in yellow, or random variations in the positions of the loading segments in red. The random variations were simulated by adding a uniformly distributed variation around the lithographic resolution of 120 nm, in other words, the gap distances  $g_1$  and  $g_2$  were uniformly shifted by  $\pm 120$  nm. Subfigure (a) shows only reflection curves and (b) transmission curves for better

comparison. As we can see, higher propagation losses do not impact so much the response of the device, except for a higher number of notches, and they have deeper notches in the transmission curves, due to the power lost in propagation. However, the random variation in the loading segment positions makes the reflection bands have less clear spacing and widens the reflection bands. This is consistent with the characterized results shown in Fig. 4.5 and is a likely explanation for the absence of clear reflection bands. In more recent explorations, we have also found that the gap distances  $g_1 = 449$  nm and  $g_2 = 500$  nm might impose an effective index perturbation that is greater than ideal. This would also help to explain the weak reflection bands in the results in Fig. 4.5 and will be probed in future fabrication runs.

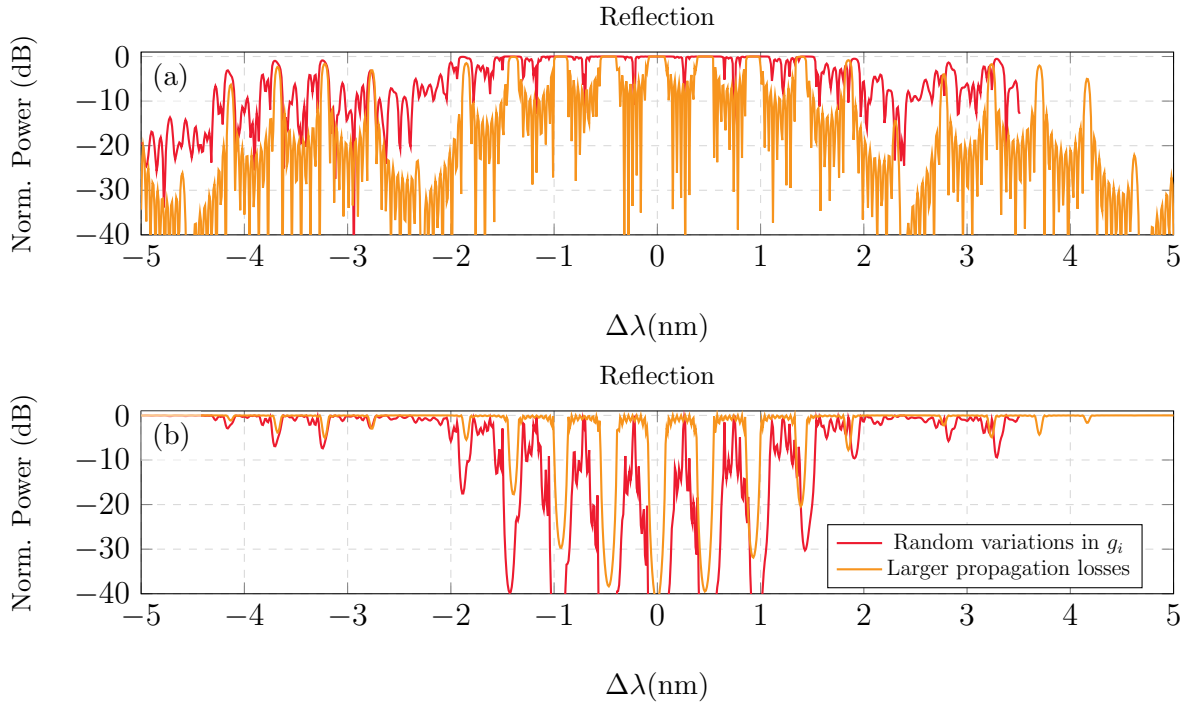


**Fig. 4.6** Comparison between simulated results with higher propagation losses and random variations to the loading segments position. Reflection curves are shown in (a) and Transmission curves are shown in (b).

## 4.3 Random Sampled SWG-WBG

### 4.3.1 Design and Layout

Random BGs have many applications that rely on the random reflection of the propagating signal. Random variations are inherent to the fabrication process of SiP devices. However, we need to apply random variations to the design in a rigorous manner. Fig. 4.7 shows the device layout.

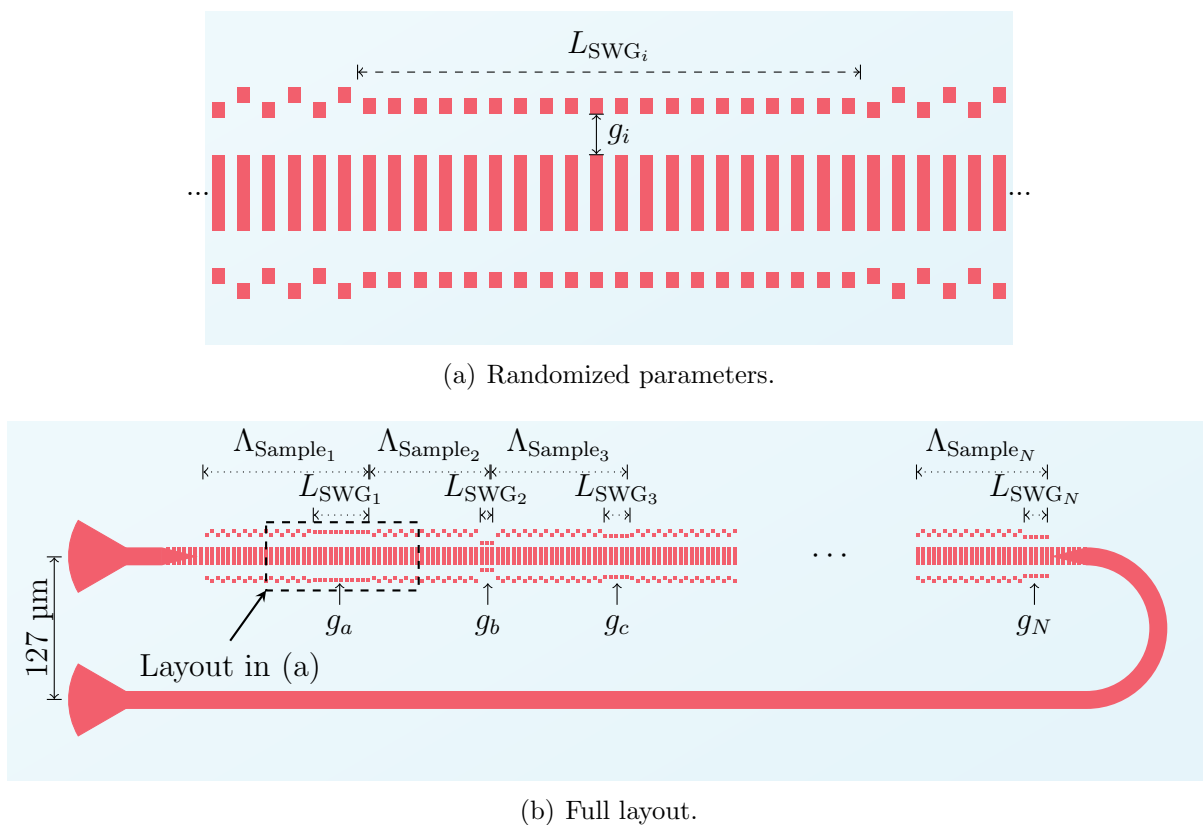


**Fig. 4.7** Layout of the Random Sampled SWG-WBG.

Figure 4.7(a) focuses on the two randomized parameters, which are the length of the  $i^{\text{th}}$  uniform SWG waveguide section  $L_{SWG_i}$  and the loading segments gap distances in the

same section  $g_i$ . Fig. 4.7(b) shows the full layout and highlights individual randomized parameters (such as  $L_{\text{SWG}_N}$ ,  $\Lambda_{\text{Sample}_N}$ , and  $g_N$ ). It also shows the region in the full layout that is illustrated in Fig. 4.7(a). The randomized lengths  $L_{\text{SWG}_i}$  are uniformly distributed between one SWG period and a maximum number of periods  $N_{\text{SWG}_{\text{max}}}$  and, consequently, the sampling period  $\Lambda_{\text{Sample}_i}$  and duty cycle  $D_{\text{Sample}}$  also vary with each section. Similarly, the gap distances are uniformly randomized between a minimum gap distance  $g_{\text{min}}$  and a maximum gap distance  $g_{\text{max}}$ . The individually randomized gap distances illustrated in Fig. 4.7(b) use alphabetical subscripts ( $g_a$ ,  $g_b$ , and  $g_c$ ) so that they are not confused with the gap distances in the WBG sections  $g_1$  and  $g_2$ . Effectively, the randomized uniform SWG waveguide lengths and gap distances in each sampling section create random phase shifts, as well as randomly sampling the BG structure.

The remaining parameters do not vary between the devices we will present, and their values are listed in Table 4.2. We have used standard Si film thickness of 220 nm. Many of the parameters used in the random versions of the device share their value and reason with the uniform version. This is the case with the main SWG segments width  $w$  and length  $a$ , which follows previously tested devices, the gap distances  $g_1 = 449$  nm and  $g_2 = 500$  nm are the same as in the uniform device, so are the SWG and Bragg periodicities,  $\Lambda_{\text{SWG}}$  and  $\Lambda_{\text{B}}$ , respectively, and the loading segment length and width  $l_{\text{SWG}}$  is symmetric with  $a$ . The randomized gap distances are between  $g_{\text{min}}$  and  $g_{\text{max}}$ , and  $g_{\text{min}}$  complies with the fabrication minimum feature spacing. Since we are uniformly randomizing the length of the uniform SWG waveguide in each sampling section, the sampling duty cycle  $D_{\text{Sample}}$  varies, and so we use the average sampling duty cycle  $\bar{D}_{\text{Sample}}$  as a reference for the results of each randomized device. We were able to fit one more sampling section for the random devices than the uniform version and, thus,  $N_{\text{Sample}} = 11$ .

**Table 4.2** Common parameters between all random sampled SWG-WBG versions.

$w$	$g_1$	$g_2$	$g_{\min}$	$g_{\max}$	$\Lambda_{\text{SWG}}$	$\Lambda_{\text{B}}$	$a$	$l_{\text{SWG}}$	$N_{\text{BG}}$	$N_{\text{Sample}}$
400 nm	449 nm	500 nm	70 nm	500 nm	254 nm	508 nm	127 nm	127 nm	1000	11

### 4.3.2 Results

The fabricated devices were included in the same chips as the uniform version of the device and, thus, the same VGCs and characterization setup were used.

In order to better compare and organize the characterized and simulated results, they are all shown in Fig. 4.8, where the plot rows are referenced by letters from (a) to (c) followed by a number that references the column from 1 to 3. The graphs in row (a) show the simulated Reflection for devices without any randomization. This serves as a reference for the randomized devices. The graphs in row (b) show simulated results for devices with randomizations and evidences the effective randomization of the reflection curves. In row (c), we see the characterized results for two different versions of each type of device, one in blue and another in orange. The columns, on the other hand, separate the results as they change their average uniform SWG waveguide section length and (average because  $L_{\text{SWG}_i}$  is randomized), consequently, their average sampling duty cycle  $\bar{D}_{\text{Sample}}$ . Column (1) shows results for devices with very short SWG waveguide sections, with duty cycle  $\bar{D}_{\text{Sample}} = 99.8\%$ , column (2) shows devices with duty cycle  $\bar{D}_{\text{Sample}} = 50\%$ , and lastly, column (3) shows devices with duty cycle  $\bar{D}_{\text{Sample}} = 33\%$ .

The first row of results shows the expected simulated reflection curves of sampled BGs. With decreasing duty cycle we see the wavelength spacing between the reflection notches also decreasing. In the following rows, we see results that take into account the random variations applied to the devices. In the results shown in (b1), we see a significant change

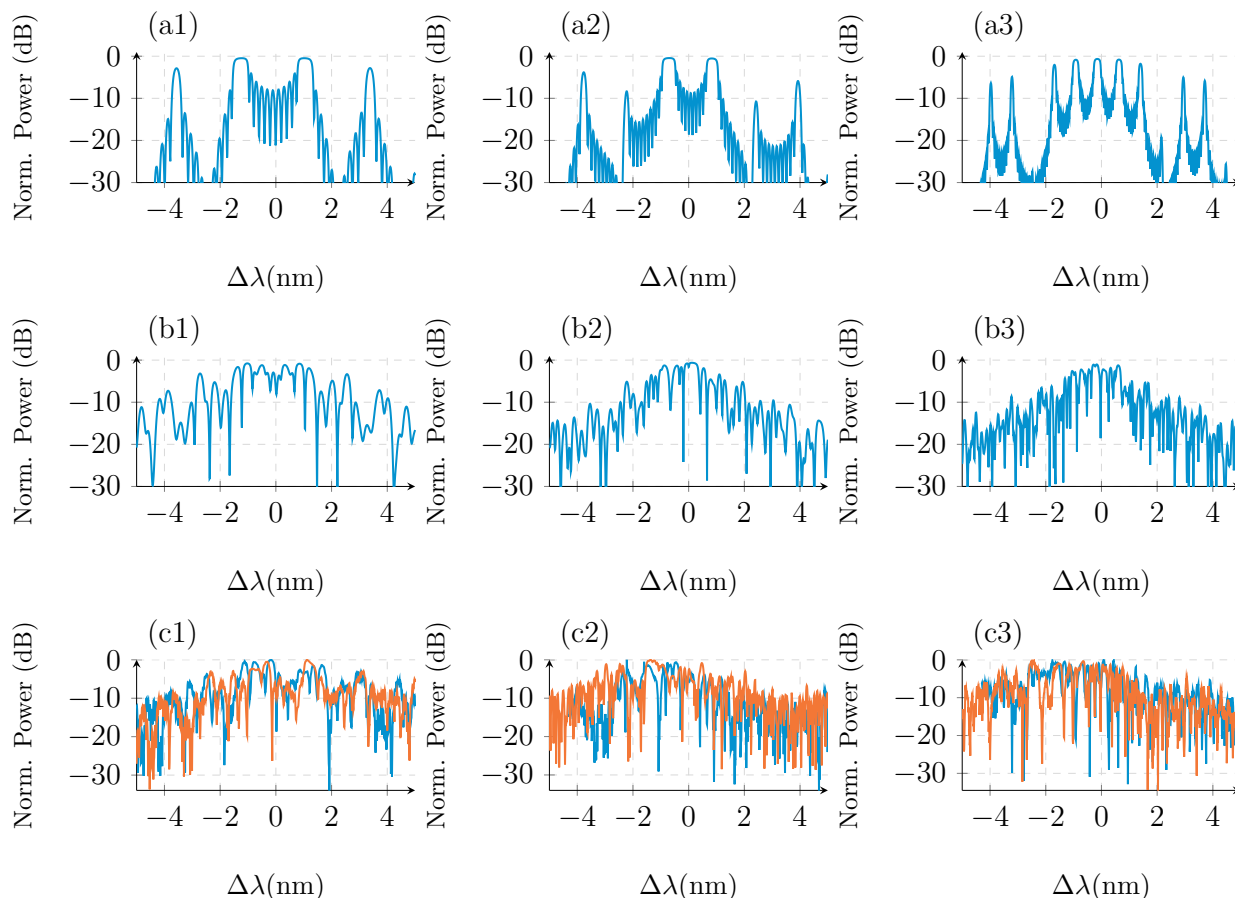


**Fig. 4.8** Reflection curves. Row (a) shows results of simulated non-randomized structures; row (b) shows the simulated results of randomized structures, and row (c) shows the characterized results of two randomized fabricated structures in blue and orange. Column (1) structures have  $\bar{D}_{\text{Sample}} = 99.8\%$ ; column (2) structures have  $\bar{D}_{\text{Sample}} \approx 50\%$ ; and column (3) structures have  $\bar{D}_{\text{Sample}} \approx 33\%$ .

from (a1), even though the duty cycle is very high at 99.8% and there are significantly fewer randomizations than in the other columns. As the duty cycle decreases with the following columns in row (b) we see less and less order in the curves.

The last row (c) shows the characterized results where, as we expected, we see curves that have even more noise than the simulated curves. What is important to notice is that the two versions of the device show different results in a pattern, not only in noise. We can

see notches that appear on one device, but not on the other. With the higher duty cycle in column (c2), we can see that the randomization makes the reflection curves less ordered, as expected. The same happens in the results shown in (c3).

Although the characterized curves in row (c) are clearly different from one another, it is hard to visually evaluate how similar they are, so it is better to compare them statistically. In a close-to-ideal scenario, the reflection curve of the gratings in the wavelength range of interest should be mostly random and, consequently, if we calculate the correlation of two random curves the result should be close to zero.

Table 4.3 shows the correlation between each of the characterized curves. To better relate the table to the characterized curves, the curves are named in the table by their position in Fig. 4.8 and are coloured by the colour of their reflection curves. We can see that between randomization versions of the same device, the reflection curves can have correlations as low as 38%, such as the correlation between the two curves in (c2). However, when comparing all of the devices, we can find a correlation as low as 28%, such as between the blue curve in (c1) and the blue curve in (c2). The low correlation means that the two randomized devices will behave very differently from one another, which is the goal of random BGs.

**Table 4.3** Correlation-matrix of the reflection curves.

	c1	c1	c2	c2	c3	c3
c1	1					
c1	0.55	1				
c2	0.28	0.38	1			
c2	0.37	0.38	0.38	1		
c3	0.4	0.4	0.38	0.54	1	
c3	0.52	0.53	0.43	0.6	0.54	1

It might seem that the achieved correlation of approximately 30% is not that low. However, we are only uniformly randomizing two parameters in the devices, and we should expect

to see some similar behaviour, such as peak-reflectivity and Bragg wavelength in the devices. Nonetheless, we were able to achieve a low correlation even between different randomizations of the same device.

We have recently found that the gap distances  $g_1$  and  $g_2$  used in these gratings produce a very strong index perturbation. We believe that with a weaker perturbation, we might be able to achieve more random responses from the devices.

#### 4.4 Summary and Conclusion

We have designed, simulated, and characterized SWG-based sampled Bragg grating devices. The SWG structures allow us to explore the technique further and use these devices as a building block to achieve other functionalities.

The wavelength spacing between the reflection bands of the Uniform Sampled SWG-WBG showed very good accuracy between the simulated and characterized results, which is crucial when building devices that control the wavelength response of the photonic circuit. The fabrication variations imposed on the device limit how much we can extend the sampling sections. It is also possible that the perturbation caused by the gap distances used in these devices is stronger than ideal, which we have found in more recent simulations and explorations. By exploring larger loading segment gap distances and in different positions we might be able to mitigate this issue.

We also showed how the SWG structures allow for efficient randomization of WBGs. The statistical differences between devices are evidenced by the correlation between reflection curves. It is still possible to explore the randomization of other parameters, *e.g.*, the

position/size of the loading segments and the duty cycle of the SWG waveguide. We can also explore WBG structures with very weak peak-reflectivity by increasing the gap distance of the loading segments.

The versatility brought by the use of SWG will also allow the exploration of more complex sampling functions. Phase-shifted and chirped sampling, for example, can still be further explored.

## Chapter 5

# Subwavelength Grating WDM

## Mux/Demux for 1310 nm and 1550 nm

### 5.1 Introduction

Diplexers are fundamental building blocks in WDM systems, which have greatly increased and allowed the expansion of the capacity in optical links, including in the fibre-to-the-home (FTTH) networks [137]. Different techniques and material platforms have been used to realize diplexers and triplexers that operate over different wavelength bands, including 1310 nm, 1490 nm, 1550 nm, and 2000 nm. The SOI platform alone has presented devices using many types of structures. For example, MMIs that incorporate tilted structures or photonic crystals have been used to realize compact structures (as short as 55  $\mu\text{m}$ ) and high Extinction Ratios (ERs) of 20  $\sim$  25 dB [138–141]. The directional coupler is another structure that has

been widely investigated using both rib waveguides [142] and standard strip waveguides, in Asymmetric Directional Couplers (ADCs) [143] and bent directional couplers [144], which achieved the shortest footprint in an experimentally characterized device ( $19 \mu\text{m} \times 31 \mu\text{m}$ ) with  $15 \sim 25$  dB of ER.

The SWG is a technique of building photonic structures with a periodicity below the wavelength of the propagating signal. It allows for increased versatility in several parameters, such as dispersion [79], and notably controlled birefringence [134, 145]. WDM diplexers/triplexers have also been proposed using SWG structures, such as solid-core waveguides with SWG structures around them [146, 147], which have achieved a simulated extinction ratio of approximately 30 dB for both 1310/1550 nm channels. A combination of solid-core waveguides with standard SWG waveguides (which is simply comprised of consecutive rectangular segments with a subwavelength periodicity) [148], has been demonstrated with simulated ERs of over 25 dB for the 1550 nm and 2  $\mu\text{m}$  channels in a 12  $\mu\text{m}$  long structure. A 1550/2000 nm diplexer design based on an Symmetric Directional Coupler (SDC) with simple SWG waveguides was reported in [149]; however, no experimental results were reported.

The reason why the exclusive use of standard SWG waveguides (consisting simply of consecutive rectangular segments with subwavelength periodicity) is of interest is the possibility to control their birefringence by tilting the segments [134, 145]. While it may be possible to design zero-birefringence waveguides and hence achieve a polarization-insensitive waveguide device, by playing with the cross-section, using different materials, polymers, or waveguide types, e.g., ridge or rib as opposed to strip. SWGs waveguides can be made in conventional silicon foundries using a single etch so there is an advantage from the fabrication point of view. In this paper, we report the design and experimental characterization of 1310/1550 nm diplexers based on an SDC with SWG waveguides.

In contrast to the BGs shown in the previous chapters, this diplexer design has a much more compact footprint. Because of that, we can rely on FDTD simulations.

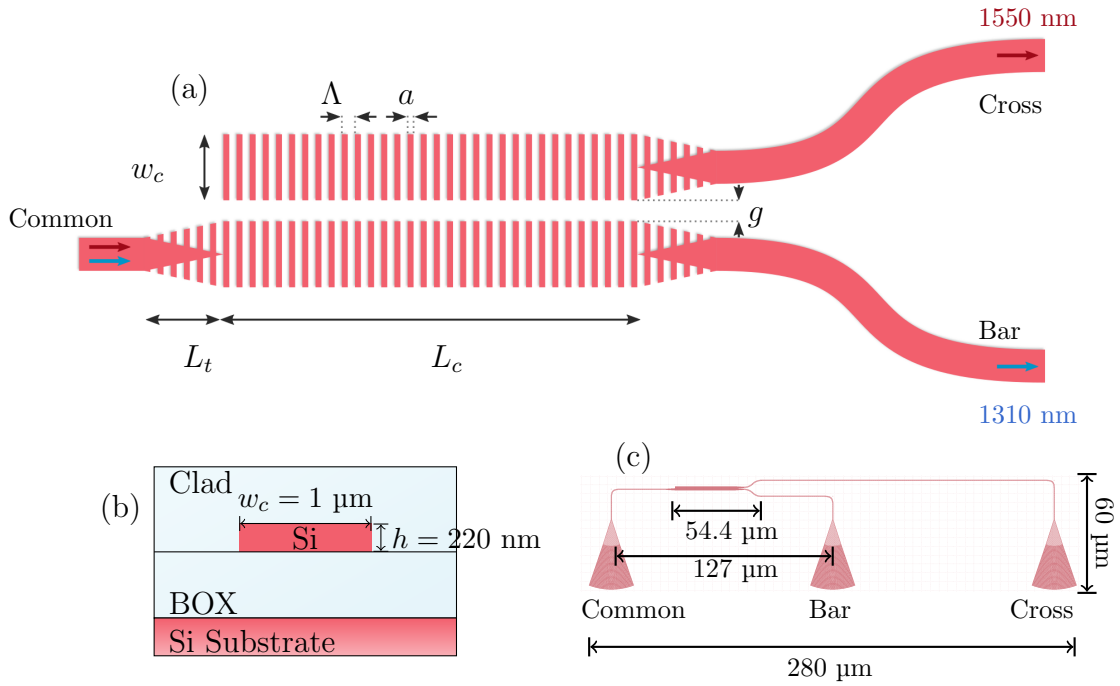
## 5.2 Layout and Design

Fig. 5.1 shows the layout of our 1310/1550 nm diplexer, which is based on an SDC with SWG waveguides. VGCs are used for the fibre-to-chip coupling; they are separated by 127  $\mu\text{m}$ , corresponding to the pitch of the fibre ribbon array used for input/output coupling, and they are connected to standard 500 nm wide solid-core waveguides. 5  $\mu\text{m}$  long SWG tapers are used to transition between the standard solid-core and SWG waveguides and 10  $\mu\text{m}$  long S-bends are used to separate the signals from the SDC region. The height/thickness of the waveguides is 220 nm.

The parameters of the device include the SWG longitudinal periodicity, which is  $\Lambda$ , and  $a$  is the length of the SWG segments. Both combined comprise the SWG duty cycle  $DC_{\text{SWG}} = \frac{a}{\Lambda}$ . The width of the SWG segments is  $w_c$ ,  $g$  is the gap distance between the two SWG waveguides, and  $L_c$  is the length of the coupler. The device is designed so that the 1550 nm channel is coupled into the Cross port and the 1310 nm channel is directed to the Bar port. The footprint of the device that shows the best results is 44.4  $\mu\text{m} \times 2.2 \mu\text{m}$  including tapers, which is only a fraction of the space between VGCs. The key parameters of our design are the SWG duty cycle  $DC_{\text{SWG}}$ , the gap distance  $g$  and the coupler length  $L_c$ .

### 5.2.1 Design

There are three key characteristics of a diplexer. The first is a high ER in both ports. Here, the ER is defined as the capability of a port to suppress one of the channels while allowing



**Fig. 5.1** The top-view of the full schematic of the device is shown in (a), the cross-section of the 220 nm thick waveguide is shown in (b), and the full device layout is shown in (c), including the VGCs.

the other channel to go through, *i.e.*, the ER of the Cross port is defined as  $ER_{\text{Cross}} = \frac{T_{\text{Cross}}(1550 \text{ nm})}{T_{\text{Cross}}(1310 \text{ nm})}$ , while  $ER_{\text{Bar}} = \frac{T_{\text{Bar}}(1310 \text{ nm})}{T_{\text{Bar}}(1550 \text{ nm})}$  for the Bar port. Secondly, the IL of the signal getting directed to its respective port should be low. Here, the IL is defined as the amount of power lost from the input to the respective output port, *i.e.*,  $IL_{\text{Cross}} = \frac{P_{\text{in}}(1550 \text{ nm})}{P_{\text{Cross}}(1550 \text{ nm})}$  and  $IL_{\text{Bar}} = \frac{P_{\text{in}}(1310 \text{ nm})}{P_{\text{Bar}}(1310 \text{ nm})}$ . Lastly, the 3-dB BW of the signal going through to its respective port should be high, while still allowing the suppression of the undesired channel. Here, the 3-dB BW is defined around the maximum point of transmission for each port/channel, which is usually centralized at the desired channel for the optimized devices.

It is well established that SDC show sinusoidal responses as a function of the coupler length and coupling coefficient [150], as shown in Equations 5.1 and 5.2, which considers lossless propagation. Two important variables in this mechanism are  $L_c$  and  $\Delta\beta$ , where  $L_c$

is a direct design parameter and  $\Delta\beta = \beta_{00} - \beta_{01}$  is the difference in supermode propagation constants, which defines the beating length among the two waveguides and can be controlled by changing the gap distance  $g$ , or the effective index. In this device's parameter space, we can control the effective index of the SWG waveguides through the width  $w_c$  and the duty cycle  $\text{DC}_{\text{SWG}}$ . Once the subwavelength periodicity  $\Lambda$  is defined,  $\text{DC}_{\text{SWG}}$  is controlled through  $a$ . Because they both have a similar impact, it is best to vary one and fix the other, and so we have arbitrarily chosen to fix  $w_c$  and vary  $a$ .

$$T_{\text{Bar}} = \frac{P_{\text{Bar}}}{P_{\text{Common}}} = \cos^2\left(\frac{L_c}{2}\Delta\beta\right) \quad (5.1)$$

$$T_{\text{Cross}} = \frac{P_{\text{Cross}}}{P_{\text{Common}}} = \sin^2\left(\frac{L_c}{2}\Delta\beta\right) \quad (5.2)$$

As a starting point for the exploration of the parameter space, we use  $\Lambda = 200$  nm, which satisfies the subwavelength operation  $\Lambda \ll \lambda$ ,  $a = 100$  nm, which yields a duty cycle of 50%, and  $w_c = 1$   $\mu\text{m}$ , which has a good difference in the effective index for the 1310 nm and 1550 nm channels, making the beating length for each channel differ, allowing wavelength-dependent coupling. The use of the ER as a FOM is effective in making sure that one channel gets through the device and the other gets suppressed. On the other hand, maximizing BW or minimizing IL might not ensure the suppression of the undesired channel. Fig. 5.2 shows the ER of both ports as a function of the coupler length  $L_c$  for two different gap distances  $g$ . Unless otherwise stated, the simulations were done using 2.5D FDTD in Lumerical. Based on Fig. 5.2, we can see that for a gap distance of  $g = 120$  nm, at around a coupler length of  $L_c = 45$   $\mu\text{m}$  the ERs of both ports are consistently higher than 10 dB for several consecutive points. This represents a good starting point for the optimization. We can also see that in

the second graph, in which the gap distance is set at  $g = 150$  nm, there is not a clear region in the curves where the ERs of both ports are higher than 10 dB or lower than -10 dB.

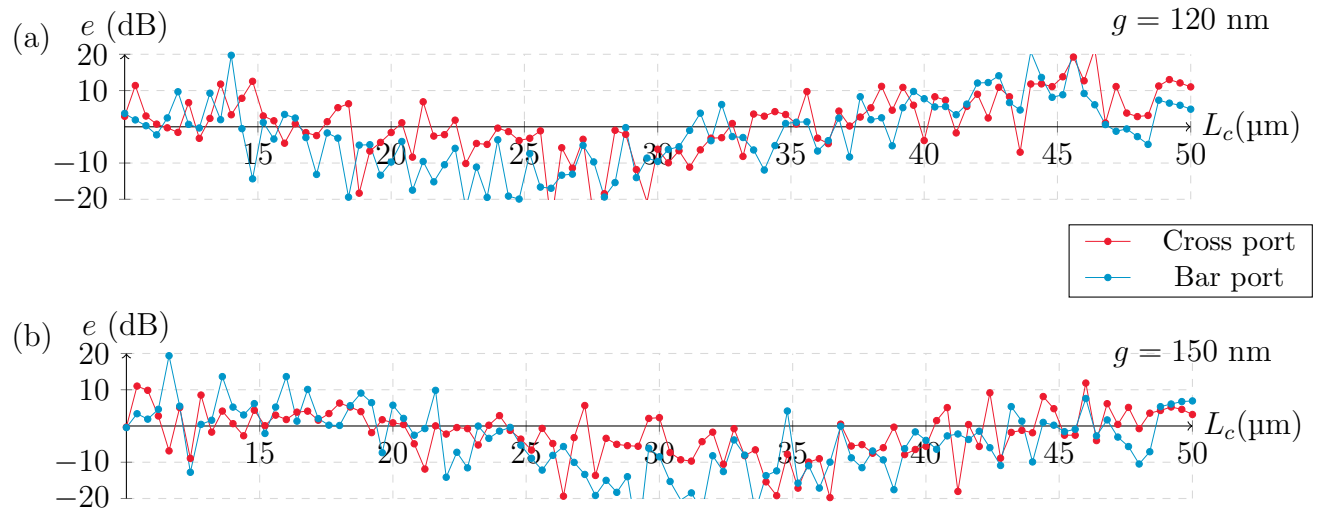


**Fig. 5.2** Extinction ratio of both ports as a function of the coupler length  $L_c$ .

We use  $g = 120$  nm,  $a = 100$  nm, and  $L_c = 45$   $\mu\text{m}$  as a starting point for the PSO algorithm. The PSO maximizes a FOM that is defined as the product of the ERs (in dB) of both ports, *i.e.*,  $\text{FOM} = \text{ER}_{\text{Bar}}(\text{dB}) \times \text{ER}_{\text{Cross}}(\text{dB})$ . In case both ERs are positive, that means that the Cross port will let through the C-band channel and suppress the O-band, and the Bar port will do the opposite. If both ERs are negative, the product will still be maximized, but the Cross port will now let through the O-band and suppress the C-band, and the Bar port, again, will do the opposite. Effectively, the PSO will maximize both ERs, regardless of which port each channel gets directed to. Moreover, the product of both ERs is an effective FOM at improving the performance of both ports simultaneously, without prioritizing a single port too heavily. There might be room for improvement in the design of a multi-objective function, where the FOM could be comprised of not only the ER but also BW and/or IL.

Having defined the parameter space starting point and FOM, we need to define the range for each parameter. The parameter ranges require caution since a range that is too small will likely not converge to a FOM maximum that yields a good performance, and a range that is too large will likely make the parameters completely diverge. A starting point can be  $\pm 10\%$  for each parameter from the starting point, and then let the algorithm run until it reaches a FOM plateau for several generations, at which point the algorithm will have reached a local maximum that might require a parameter range update. After a few parameters range updates the algorithm will have reached a local maximum that is, hopefully, higher than a FOM of  $ER_{\text{Cross}} \times ER_{\text{Bar}} > M$ , where  $M$  is the desired magnitude of the product of both ports ERs, *i.e.*, if we desire both extinction ratios to be around 20 dB,  $M \approx 20^2$ . There is a trade-off between the time required to achieve a local maximum (computational cost) and how finely optimized each parameter is. Generally, our optimized sets of parameters required around a few hundred generations with 6 particles. This process is illustrated in the flowchart shown in Fig. 5.3.

By following this procedure, we have found optimized devices for a range of SWG periodicities, namely 200 nm, 205 nm, 210 nm, and 215 nm. We have also found a set of optimized parameters for a device with SWG periodicity of  $\Lambda = 200$  nm and width  $w_c = 500$  nm, instead of 1  $\mu\text{m}$ . This would allow for a SWG taper with no width change, and it is also a significant effective index change from  $w_c = 1$   $\mu\text{m}$ , which allows us to probe whether it was a good decision to fix it and only vary  $a$  to control the effective index. Table 5.1 shows the aforementioned sets of optimized parameters and the simulated results. The BWs of the optimized designs are over 200 nm, which is larger than that of the VGCs used in fabrication.

Figure 5.4 shows the power profiles for each port, 1310 nm in (a) and 1550 nm in (b) for Design 1. It clearly shows the signal getting directed at each port depending on the

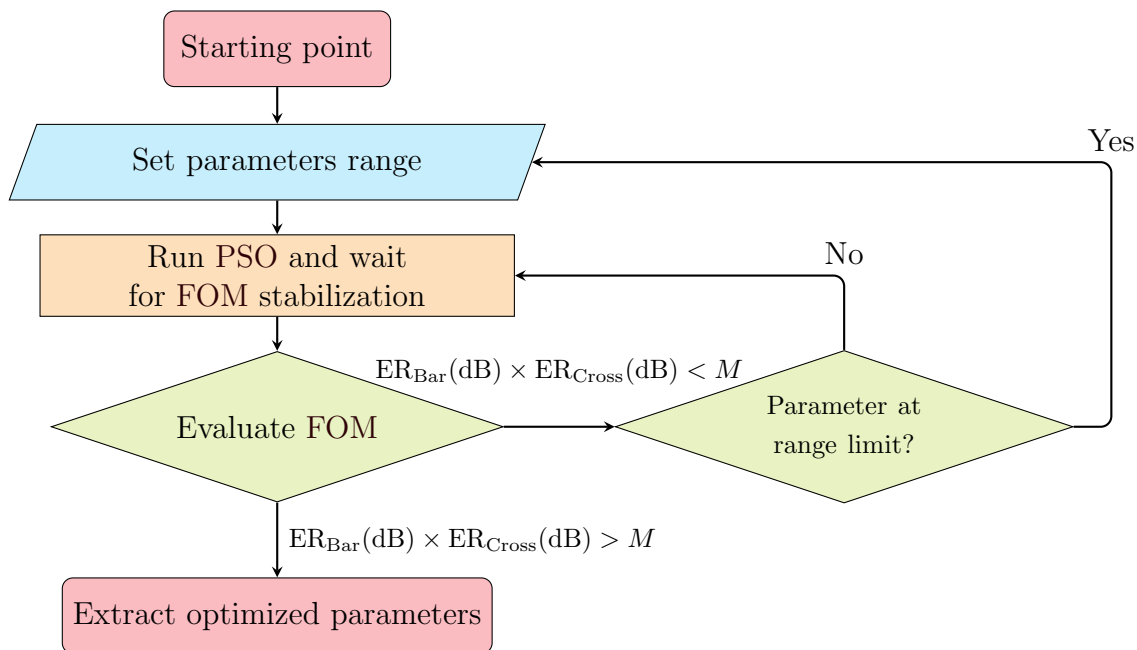


**Fig. 5.3** PSO algorithm flowchart.

**Table 5.1** Parameter values of the optimized WDM diplexers.

	$\Lambda$ (nm)	$L_c$ ( $\mu\text{m}$ )	$a$ (nm)	$g$ (nm)	$w_c$ ( $\mu\text{m}$ )	$\text{ER}_{\text{Cross}}$ (dB)	$\text{ER}_{\text{Bar}}$ (dB)	$\text{IL}_{\text{Cross}}$ (dB)	$\text{IL}_{\text{Bar}}$ (dB)
Design 1	200	34.4	82	98	1	24.7	20.4	0.6	0.6
Design 2	205	41.205	89	118	1	18.0	21.0	0.4	0.5
Design 3	210	38.01	89	106	1	12.6	8.3	2.6	3.2
Design 4	215	37.84	89	114	1	6.9	6.9	2.3	3.1
Design 5	200	13.2	90	150	0.5	9.3	19.5	0.0	0.3

wavelength of the propagating signal. It also shows that the signal at 1310 nm gets across the gap, into the parallel SWG waveguide once before coming back to the Bar port. This means that it is possible to reduce the footprint of the device where the signal at 1310 nm gets concentrated at the Cross port and 1550 nm at the Bar port. We have explored the parameter space to achieve this and, although it is feasible, the ER of the ports gets significantly reduced and insertion loss is increased. This set of optimized parameters is a compromise between footprint and performance. The ERs for the Cross and Bar ports are 25 dB and 20 dB, respectively, the IL is 0.6 dB for both ports, and the BWs are 230 nm and

300 nm for the Cross and Bar ports, respectively.

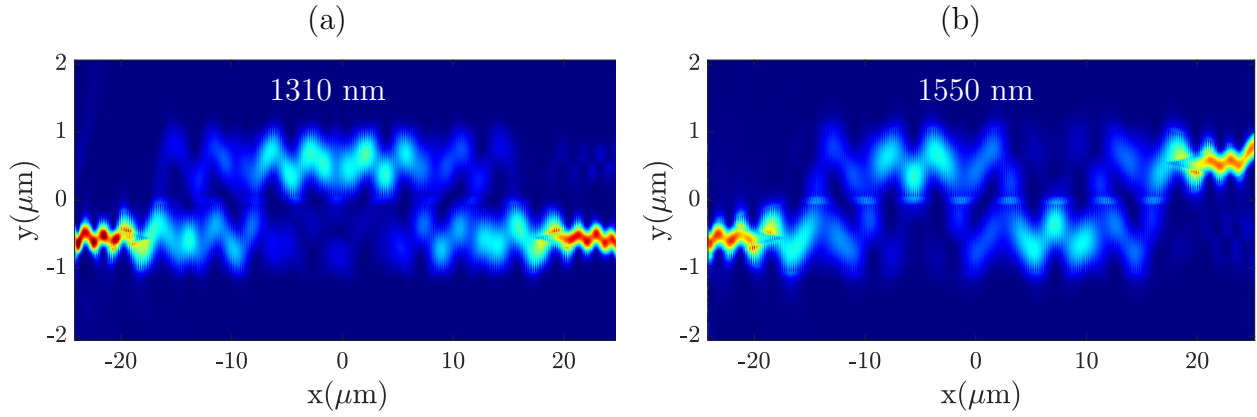
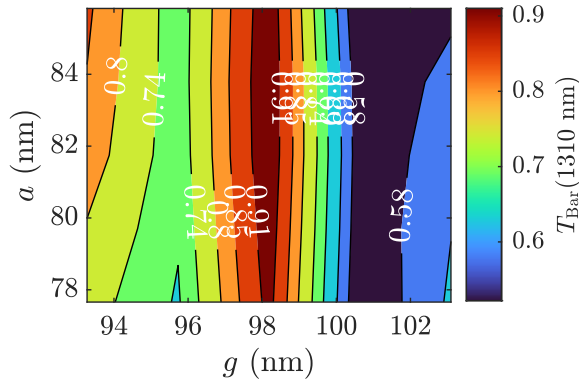


**Fig. 5.4** Simulated power profile for 1310 nm in (a) and 1550 nm in (b) of Design 1.

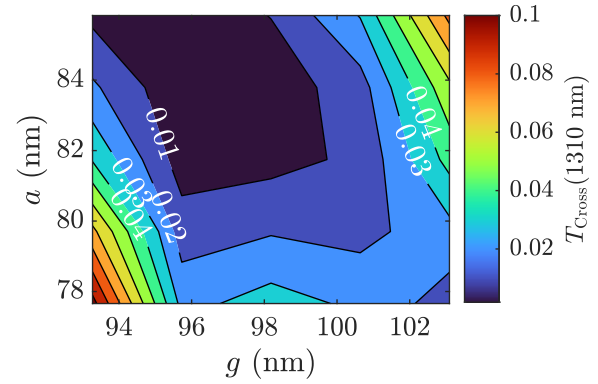
### 5.2.2 Tolerance Analysis

To assess the tolerance of the device we perform a corner analysis of two of the key parameters of the device,  $a$  and  $g$ .  $L_c$  depends on an integer number of SWG periods and should not meaningfully vary in fabrication. Fig. 5.5 shows the transmission at 1310 nm for the Cross and Bar ports in (a) and (b), respectively, and 1550 nm in (c) and (d) for Design 1. We can see that the center of the plots simultaneously minimizes one channel while maximizing the other and that the center of the plots is a good compromise between the two functions. This ensures a good ER of the device.

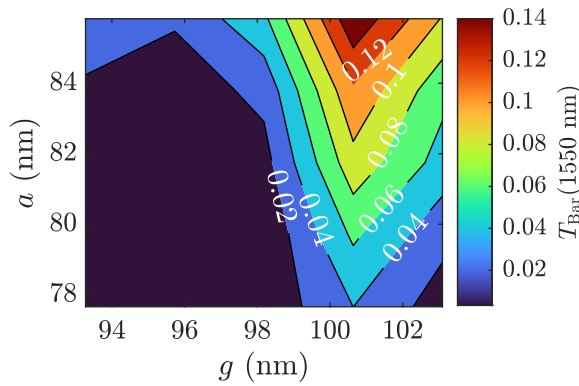
With the transmission values, we can calculate the ER of each port in the same corner analysis. Fig. 5.6 shows a  $\pm 5\%$  corner analysis of the ER at both ports as a function of  $a$  and  $g$ . The center of the plot represents the optimized value and reflects a good compromise between the performance of each port; it also highlights how the gap distance  $g$  is a sensitive parameter.



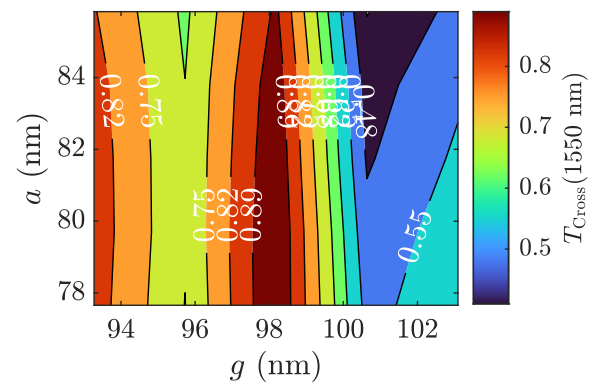
(a) Transmission of the Bar port at 1310 nm.



(b) Transmission of the Cross port at 1310 nm.

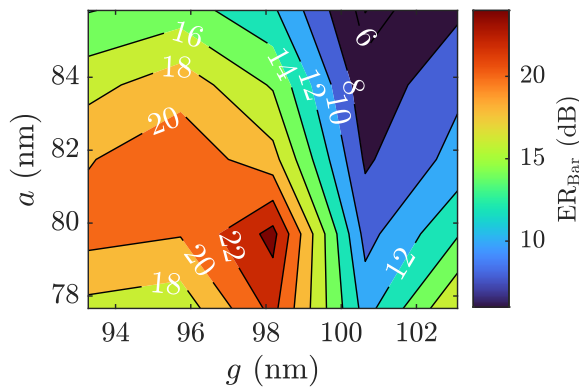


(c) Transmission of the Bar port at 1550 nm.

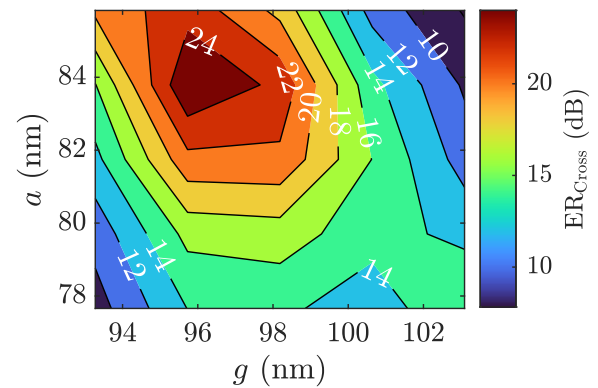


(d) Transmission of the Cross port at 1550 nm.

**Fig. 5.5** Transmission as function of gap length  $g$  and SWG segment length  $a$  for each port and each channel.



(a) Bar port.



(b) Cross port.

**Fig. 5.6** Extinction ratio as function of gap length  $g$  and SWG segment length  $a$  for each port.

Fig. 5.7 shows the corresponding IL for the Cross and Bar ports in (a) and (b) for Design 1. Again, we can see that the gap distance  $g$  is particularly important to maintain low insertion losses.

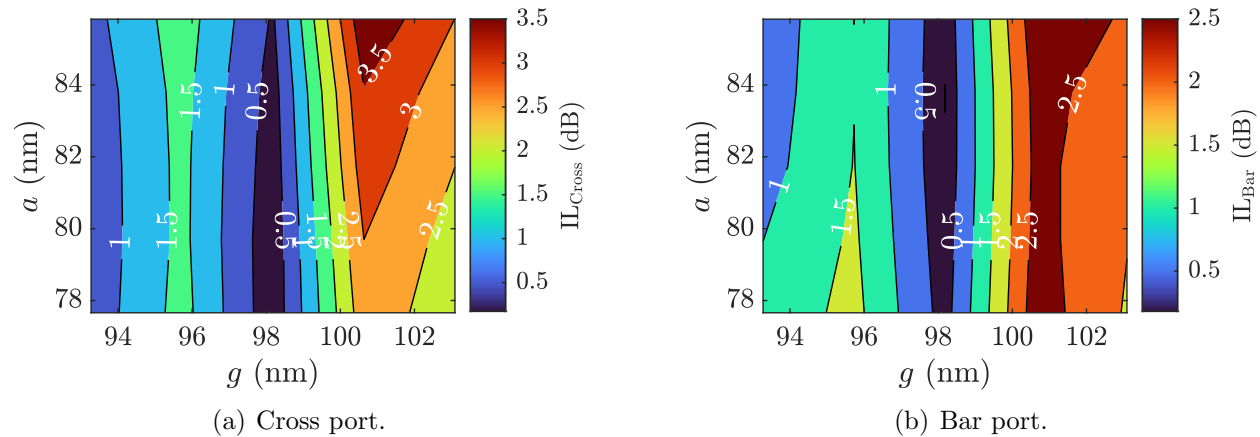


**Fig. 5.7** Insertion Loss as function of gap length  $g$  and SWG segment length  $a$  for each port/channel.

### 5.2.3 Fabrication Variations

Fabrication variations are a known issue in SiP devices and are the main reason why the simulated results diverge from characterizations. In SWG-based structures, two prominent variations are in segment sizes and sidewall angles, see Fig. 5.8. There could also be random variations in the position of the segments, although the impact on the effective index would be smaller. In order to consider a simplified version of the size variations, which can occur due to over-etching and lithographic-resolution-related issues, we have simulated a uniform distributed random size reduction of the SWG segments. In other words, the  $i^{\text{th}}$  SWG segment has a length of  $a_i = a - \mathcal{U}(0, \sigma)$  (where  $\sigma$  is a maximum variation) and width  $w_i = w_c - \mathcal{U}(0, \sigma)$ , where  $\mathcal{U}(0, \sigma)$  is a uniformly distributed random number between 0 and  $\sigma$ , resulting in smaller segments and causing the effective index to decrease. Another typical

issue in fabrication is a non-vertical sidewall angle, which is due to the shortened erosion time at the bottom of the Silicon substrate etching process, although it can be controlled to a certain degree [151].

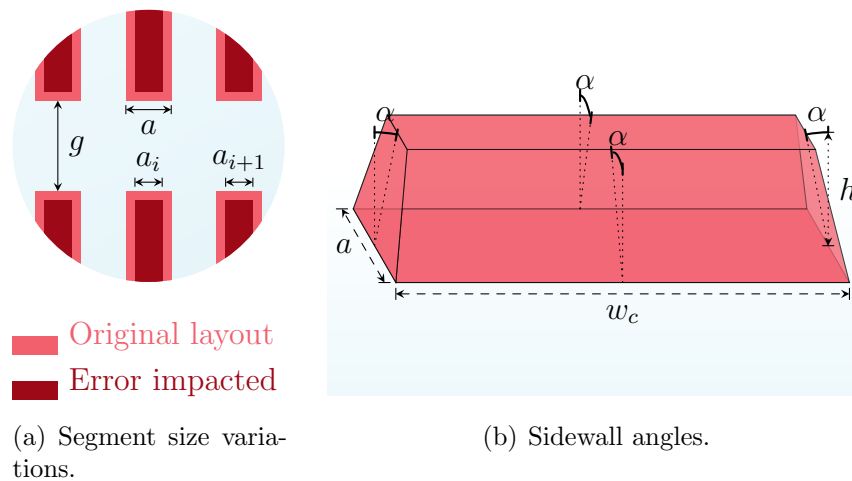


**Fig. 5.8** Simulated fabrication variations on the SWG segments.

Here, we use 3D FDTD simulations to investigate the impact of variations in segment size and 2.5D FDTD for sidewall angles on the device performance. The results in Fig. 5.9 show that for state-of-the-art e-beam (corresponding to a random error between 0 and 1 nm), the impact of size variations is negligible whereas an error between 0 and 10 nm shows a degradation in ILs and more significantly in ER, especially for the Cross port.

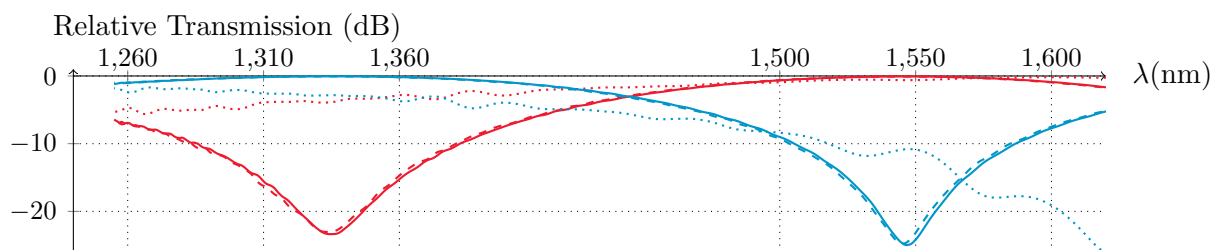


**Fig. 5.9** Simulated relative transmission for the Cross port in red and the Bar port in blue, considering random SWG segment size reductions for Design 1. Solid line shows the ideal case, dashed for  $\mathcal{U}(0, 1)$ , and dotted for  $\mathcal{U}(0, 10)$ .

Similar to the lithographic resolution-related issue, a sidewall angle reduces the volume of the Si segments and, consequently, reduces the effective index of the waveguide. Fig. 5.10 shows the simulations where all the SWG segments have sidewall angles in all four directions. As we can see, even a  $1^\circ$  sidewall angle impacts the extinction ratio of the device. However, a  $5^\circ$  angle in all four sides of the SWG segments can compromise the ERs and ILs. We can expect the sidewall angle to be smaller than  $5^\circ$  since it is controllable [151].

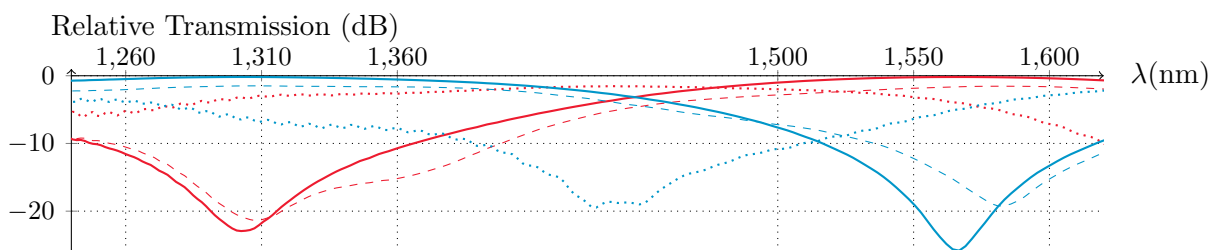


**Fig. 5.10** Simulated relative transmission for the Cross port in red and the Bar port in blue considering sidewall angles in the SWG segments. Solid line shows the ideal case ( $\alpha = 0^\circ$ ), dashed for  $\alpha = 1^\circ$ , and dotted for  $\alpha = 5^\circ$ .

### 5.3 Results

The devices were fabricated at ANT and were characterized using a tunable laser and power meter. We have fabricated not only the devices listed in Table 5.1 but also variations to the key parameters of the device. Namely, we included versions of each optimized device with both a negative and positive shift of 10 nm, 20 nm and 50 nm to  $a$  and  $g$  (limiting these variations to the fabrication constraints). We have also included versions with a simultaneous increase to  $\Lambda$ ,  $a$ , and  $g$  of 10 nm, 20 nm, and 50 nm, and also a proportional increase to the same parameters of 5%, 10%, and 25%.

We did not have access to wideband VGCs at the time of fabrication, so we fabricated the devices with C-band and O-band VGCs, but both versions of each device were fabricated

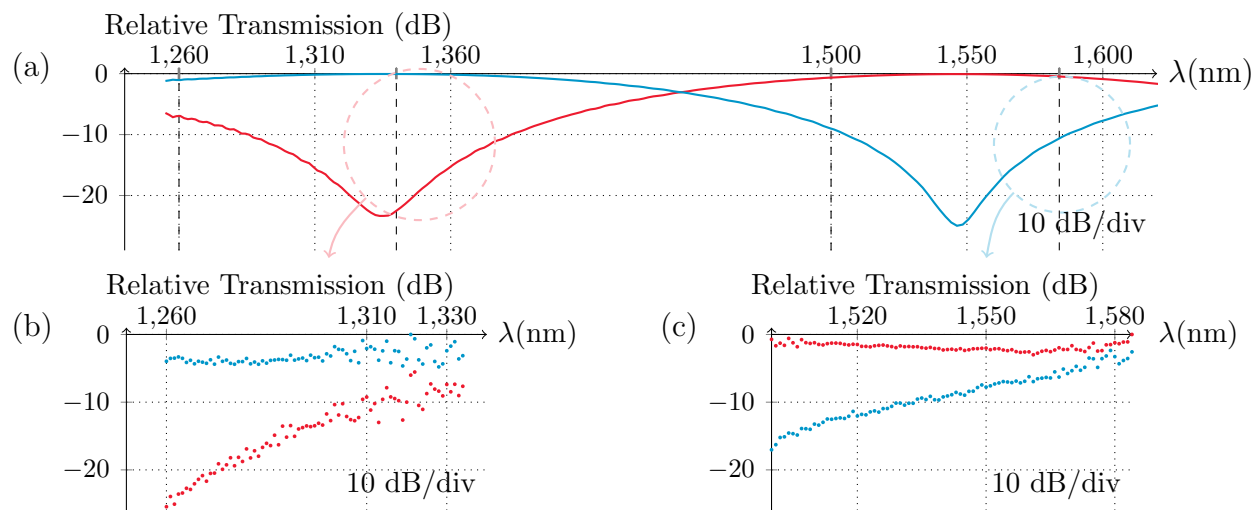
in the same chip only 110  $\mu\text{m}$  apart. The BW and IL for the VGCs are 80 nm and 7 dB, and 70 nm and 10  $\sim$  12 dB in the C-band and O-band, respectively. It is possible to use improved VGC, as there have been couplers demonstrated with IL as low as 1.2 dB and 134 nm 3-dB BW [152], although requiring several material deposition layers.

### 5.3.1 Device with Simulated Optimized Parameters

The devices for which we show the characterized results in this subsection were fabricated in two separate fabrication runs. The results were significantly similar, which evidences the replicability of the devices.

Fig. 5.11(a) shows the simulated transmission spectra at both ports of the diplexer using 3D FDTD while the measured responses are shown in Fig. 5.11(b) and (c) for the C-band and O-band, respectively. The full 3D FDTD simulation causes a small red shift in  $T_{\text{Cross}}$  and a small blue shift in  $T_{\text{Bar}}$  compared to the 2.5D FDTD simulations used for optimizing the device design with the PSO. The characterized response is limited by the tuning range of the laser source as well as the bandwidth of the VGCs (70 nm in the O-band and 80 nm in the C-band). The reason for the wide variations observed at the upper wavelengths in Fig. 5.11(b) is that the O-band VGC used was not optimized for this MPW run and has limited bandwidth.

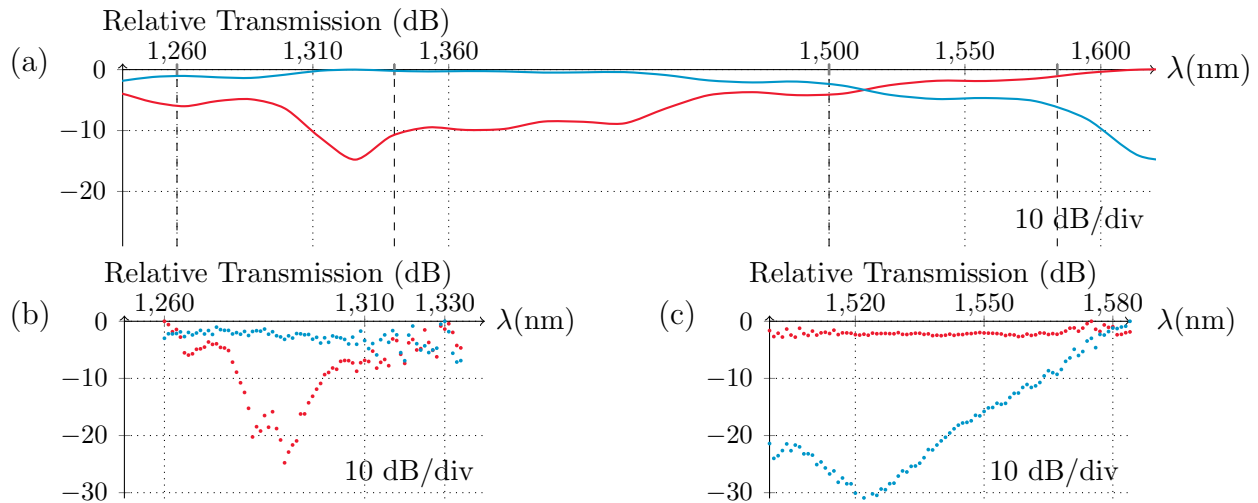
The simulated results show an ER of around 25 dB and negligible IL. The fabricated device shows a spectral shift that we attribute to fabrication variations, which we have also observed in other SWG-based devices that were fabricated in the same MPW runs [84]. Based on the spectral shifts from the other devices, the measured transmission spectra correspond to the simulated results highlighted by the dashed circles in Fig. 5.11(a). The measured ERs are almost 10 dB and the ILs are approximately 2 dB for both ports.



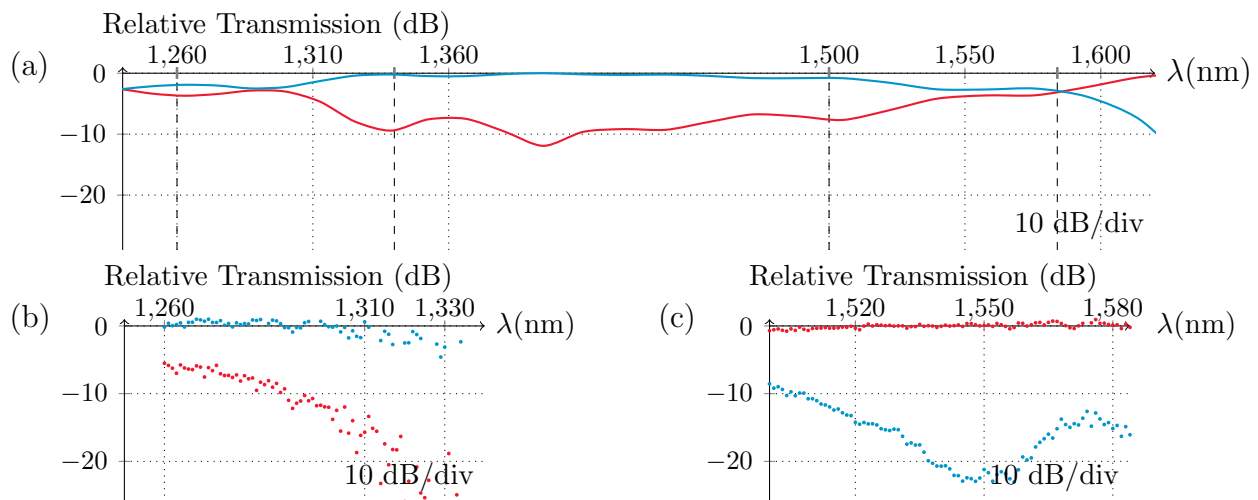
**Fig. 5.11** Simulated relative transmission for the Cross port in red and the Bar port in blue are shown in (a) and the characterized relative transmission curves are shown in (b) and (c) for the O-band and C-band, respectively, with a vertical scale of 10 dB/div.  $DC_{SWG} = 0.41$ . The vertical dashed lines indicate the characterization range, 1260 nm to 1330 nm and 1500 nm to 1584 nm in the O and C bands, respectively.

Fig. 5.12 shows the responses from 2.5D FDTD simulation in (a) and characterizations in (b) and (c) for one of the variations of Device 1, *i.e.*, where  $a$  is 10 nm larger, corresponding to an effective index approximately 4% larger. The larger effective index causes a change to the beating length and, consequently, a spectral shift in the device due to dispersion. The ILs are -3 dB and -1 dB for the Cross and Bar ports, respectively. Although the ERs are only 5.5 dB and 9 dB for the Cross and bar ports, respectively, we observe a red shift from the device shown in Fig. 5.11.

Figure 5.13 shows another variation of Design 1 where the  $a$  is increased by 20 nm and, consequently, the duty cycle  $DC_{SWG}$  is increased to 0.51. A larger red shift from the results in Fig. 5.11 is observed, and we can now see the minimum of  $T_{Cross}$  and  $T_{Bar}$  much closer to 1310 nm and 1550 nm, respectively. The devices with increased duty cycle have an ER of around 20 dB for both ports and negligible ILs.



**Fig. 5.12** Simulated relative transmission for the Cross port in red and the Bar port in blue in (a) and characterized in the O-band in (b) and C-band in (c) for the device with a 10 nm increase in SWG segment length, *i.e.*,  $DC_{\text{SWG}} = 0.46$ .



**Fig. 5.13** Simulated relative transmission for the Cross port in red and the Bar port in blue in (a) and characterized at the O-band in (b) and C-band in (c) for the device with a 20 nm increase in SWG segment length, *i.e.*,  $DC_{\text{SWG}} = 0.51$ .

The results in Figs. 5.11-5.13 show how the effective index impacts the specific spectral range of the diplexer and that the spectral shift can be tuned through the duty cycle  $DC_{\text{SWG}}$  for a fixed SWG period  $\Lambda$ . The ERs are not larger than 10 dB for duty cycle of 0.41 and 0.46, whereas we achieve around 20 dB of ERs with a duty cycle of 0.51.

### 5.3.2 Footprint Focused Design

As shown in Table 5.1, Design 5 uses an SWG width of 500 nm and, more importantly, a significantly smaller coupler length  $L_c$  and, consequently, a significantly smaller footprint. The design process prioritized compactness, as opposed to a greater ER. The achieved size would be such a significant footprint reduction that would make this device stand out. Fig. 5.14 shows the simulated and characterized results of the device. The simulated results in (a) show a slightly smaller ER  $ER_{\text{Cross}}$ , but negligible IL and wide BW for both ports. Unfortunately, the performance of the fabricated devices in (b) and (c) do not reproduce those expected from simulations.

We also characterized parameter-shifted versions of Design 5, similar to what was done with Design 1. None of the variations achieved the desired results for both ports. We were able to enhance the results of one port, by varying SWG duty cycle, to the detriment of the other port.

Figures 5.15 and 5.16 show the simulated transmission spectra from 3D FDTD and 2.5D FDTD, respectively, of Design 5 with variations in the SWG segment size and sidewall angles. In contrast to the results shown in Figs. 5.9 and 5.10 for Design 1, it is clear that such variations have less impact on the response (*e.g.*, ER or IL). While these simulations might seem to suggest Design 5 is more robust to these types of variations, the fabricated

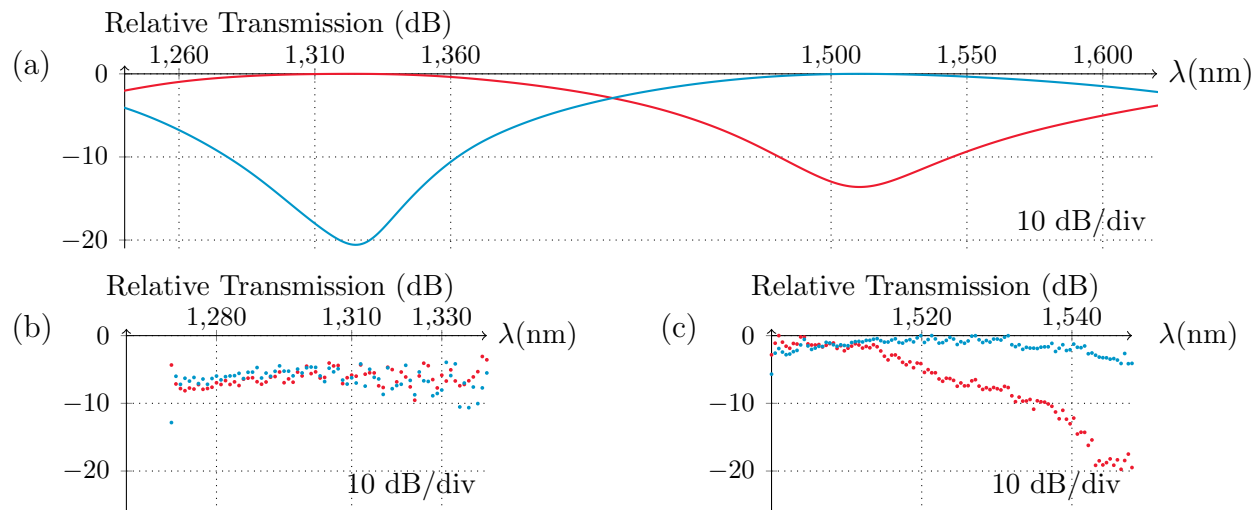


**Fig. 5.14** Simulated relative transmission for the Cross port in red and the Bar port in blue in (a) and characterized at the O-band in (b) and C-band in (c) for Design 5.

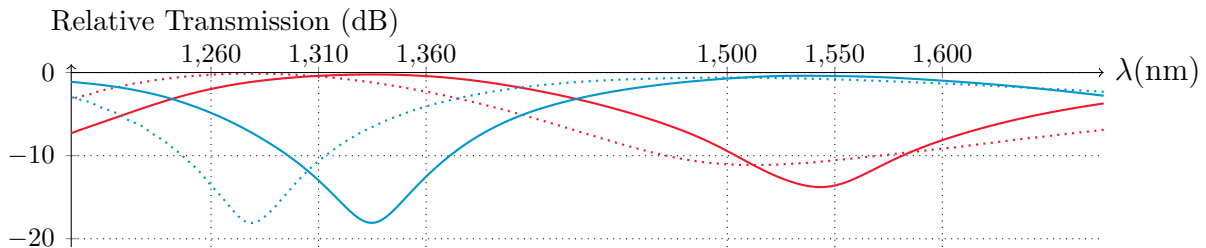


**Fig. 5.15** Transmission curves of the Cross port in red and Bar in blue for Design 5 with random SWG segments size variations. Solid line shows the ideal case, and dotted for  $\mathcal{U}(0, 10)$ .

devices show that Design 1 might be more tolerant. We believe the increased width and consequently, the increased index in Design 1 may have provided higher robustness.

None of these variations alone explain the poor performance of the compact device. A combination of these fabrication errors and possibly others are most likely responsible. We believe the increased width in the previous devices may have provided more robustness to the fabrication variations, due to a relatively smaller effective index change. In future works, another approach we can test is by optimizing the device accounting for the blue shift from

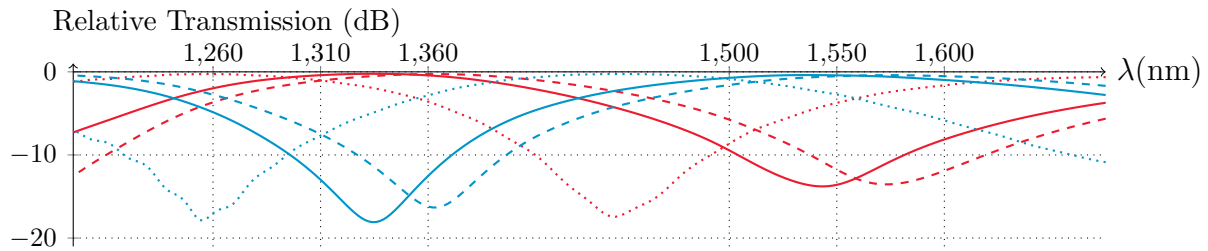


**Fig. 5.16** Sidewall angle impact on the transmission of the Cross port in red and Bar in blue for Design 5. Solid line shows the ideal case ( $\alpha = 0^\circ$ ), dashed for  $\alpha = 1^\circ$ , and dotted for  $\alpha = 5^\circ$ .

the start, namely, optimizing the devices, not for 1310 nm and 1550 nm, but for  $1310 \text{ nm} + \Delta\lambda$  and  $1550 \text{ nm} + \Delta\lambda$ , where  $\Delta\lambda$  is a pre-determined wavelength shift, instead of only shifting the parameters.

## 5.4 Summary and Conclusion

We have presented the layout, design process, and both simulated and characterized results of WDM diplexers based on a SWG SDC. By testing structures with different SWG duty cycles (and hence effective index) we found that it is possible to make the fabricated device operate at the desired wavelengths of 1310 nm and 1550 nm with much higher ERs than the design with the parameters extracted from simulations, without compromising IL or BW. This can be the focus of further design optimization, not only for this device but also for other SWG-based devices.

The footprint of our proposed device is small, but not the smallest in the literature [143]. Likewise, the ER we have achieved is comparable to the devices in the literature, although a little behind the state-of-the-art. Table 5.2 shows a comparison of this work with some of the works in the literature. All of the devices included in the table have been fabricated (we have

not included works with only simulated results) and are designed for the 1310 nm and 1550 nm channels (and 1490 nm, in the case of triplexers). The definition of these parameters, such as ER and BW, vary in the literature, so we have estimated some of them based on the reported characterized transmission curves at 1310 nm and 1550 nm, specifically. Our BW measurements were limited by the VGC response. If we allow for a small wavelength shift, the ER our device achieves is almost 25 dB and 30 dB for the Bar port (O-band) and Cross port (C-band), respectively. With a second fabrication run, we would likely put the device at the state-of-the-art level in regards to ER.

**Table 5.2** Experimental performance comparison with similar devices in the literature.

Reference	$e$ (1.31 $\mu\text{m}$ , 1.55 $\mu\text{m}$ )	3-dB BW (1.31 $\mu\text{m}$ , 1.55 $\mu\text{m}$ )	IL (1.31 $\mu\text{m}$ , 1.55 $\mu\text{m}$ )	Footprint
[138]	25 dB, 15 dB	40 nm, 70 nm	5 dB, 1 dB	128.5 $\mu\text{m} \times 15 \mu\text{m}$
[139]	25 dB, 15 dB	100 nm, 20 nm	2 dB, 2 dB	450 $\mu\text{m} \times 7 \mu\text{m}$
[143]	25 dB, 40 dB	70 nm, 20 nm	<1 dB, <1 dB	150 $\mu\text{m} \times 20 \mu\text{m}$
[141]	20 dB, 25 dB	192 nm, 123 nm	1 dB, 1 dB	55 $\mu\text{m} \times 2.5 \mu\text{m}$
[146]	30 dB, 25 dB	120 nm, >150 nm	<1 dB, <1 dB	42.2 $\mu\text{m} \times 2.3 \mu\text{m}$
[153]	25 dB, 15 dB	60 nm, 20 nm	<1 dB, <1 dB	19 $\mu\text{m} \times 31 \mu\text{m}$
<b>This work</b>	15 dB, 20 dB	>70 nm, >80 nm	<1 dB, <1 dB	44.4 $\mu\text{m} \times 2.2 \mu\text{m}$

Although the promise of negligible propagation losses in SWG is yet to be achieved [76], the compact footprint allows for small ILs in both ports. Moreover, the use of standard SWG waveguide buses to build the SDC will allow us to explore a polarization-insensitive version [134, 145]. The polarization-insensitive WDM diplexers/triplexers that have been demonstrated in the literature have required a large (20  $\mu\text{m}$  radius) 180° bent Directional Coupler [144], non-standard material deposition thicknesses and layers [154], or very large footprints (over 2 mm long) by cascading structures [155, 156]. We believe that by tilting the SWG we can achieve a polarization independent with a similar footprint to the device presented here, requiring only a single etch in fabrication.

Lastly, we have shown the simulated and characterized results for an optimized device

with narrower SWG waveguides, which would have been the smallest footprint in the literature. Although the characterized results did not achieve good performance, they show that larger SWG structures have greater robustness to fabrication variations.

# Chapter 6

## Conclusion

### 6.1 Summary

As the field of SiP keeps emerging in demand and finding new applications, it imposes the exploration of new platforms and materials. The work shown in this thesis fits into this context. Although we have focused on the design and analysis of wavelength-selective devices, the two platforms we have explored here can be used for many other applications. SiN, for instance, shows great potential for nonlinear applications because of its potential to have very low propagation losses, allowing for very high effective length structures. SWG structures can effectively control many other parameters than just effective index, such as dispersion and birefringence. Many of the analysis we have done here, such as for fabrication variations, can be used in other contexts.

In this thesis, we have explored two methods of lowering the waveguide effective index when compared to standard Si strip waveguides: using SiN and SWG-waveguides in the SOI

platform. We have updated the simulation model of SiN WBGs, designed, simulated, and characterized Sampled SWG-based WBGs, in both the uniform and random versions, and as well as a SWG-based WDM diplexer for the 1310 nm and 1550 nm channels.

### 6.1.1 SiN WBG Model Improvements

SiN offers great potential for new applications. Many challenges with the material have been overcome through the years, such as dealing with the tensile stress of the crystalline structure which caused film cracking [40]. Nonetheless, material shrinkage in the fabrication process still causes the SiN structures to significantly deviate from the designed structure. This has implications for the performance of the fabricated photonic devices that have to be taken into account.

We have considered the variations imposed by the fabrication process of SiN-based WBGs to update and improve the simulation model. We made a few assumptions in the simulation model of the device in order to keep the scope of the project feasible. As an example, we assumed that the bottom and top of the BGs are flat. We also assumed that the refractive index acquired from ellipsometry is accurate. Ellipsometry usually provides refractive index curves with reasonable accuracy, however, even a small inaccuracy can cause the simulated to significantly diverge from the fabricated device.

We used the Bragg wavelength and BW of the characterized reflection and transmission curves to infer several physical variations of the structures, simulated these variations and used the comparison between simulation and characterization to improve the model. We found that waveguide width, thickness and sidewall angle deviations can fully explain the Bragg wavelength deviation. We estimated a width increase of 49 nm (8%) and a thickness

increase of 7 nm (0.7%) in a waveguide with  $5^\circ$  sidewall angle. This is contrary to the expectation of material shrinkage, which indicates that one or more of our model assumptions is incorrect. We believe that the refractive index accuracy can have a great impact on these estimations.

We have introduced longitudinal shrinkage to the simulation model, which models one of the possible outcomes of SiN shrinkage and is an effective parameter to control the grating strength, which modulates the BW in our devices. The characterized BW due to corrugation depth curves showed higher BW for the TM mode than for the TE mode, which none of our model modifications provided. We believe that some geometric change in the fabrication variation that we might not have considered is responsible for this.

This project highlights the importance of taking into account and analyzing the variations imposed on the structures during the fabrication process. The model modifications we have proposed here are not sufficient to explain all the divergences between simulated and characterized results, yet they offer improved accuracy for future fabrications and analyses.

### 6.1.2 Sampled Subwavelength Grating Waveguide Bragg Gratings

We have demonstrated the feasibility of sampled WBG using SWG waveguides by designing, simulating and characterizing structures in both the uniform version and a random version.

The uniform Sampled SWG-WBG offers multiple reflection bands, and the number of reflection bands can be controlled by changing the sampling duty cycle. We have shown the characterization of the device with a duty cycle of 0.5, which shows three reflection bands. Unfortunately, fabrication errors severely impacted structures with a lower duty cycle (and longer total lengths), hindering the characterization of a larger number of reflection bands.

More specifically, we showed that higher propagation losses are not the cause and that random variations on the effective index, likely due to gap distance or loading segment sizes variations, are most likely responsible for the degradation. However, it is still possible to notice the reflection bands in the simulated reflection curve accounting for random variations, so further explorations on the causes of the performance degradation of the lower duty-cycle device are still necessary.

Random gratings have many applications, notably in chaotic waveform generation [74, 125], sensors [157] and random LASERs [158]. We have demonstrated the feasibility of random gratings using SWG structures. The correlation between the characterized curves can be as low as 28%.

### 6.1.3 SWG-Based WDM Diplexer for 1310 nm and 1550 nm

The ability to separate and combine signals based on their wavelengths is fundamental for WDM systems, and these WDM (de)multiplexers have been built using several techniques and platforms, including SOI. Although there have been other devices based on SWG, they are all complex structures that have SWG features, such as MMIs with photonic crystal [139]. However, we have presented the design, simulated and characterized results of a WDM (de)multiplexer using standard SWG waveguides as a basis for a SDC for the 1310 nm and 1550 nm channels. We have anticipated the effect of fabrication errors and mitigated them by varying design parameters. We have also optimized and characterized a device with a significantly smaller footprint that did not show a good improvement but shows that SWG structures with larger sizes show greater robustness to fabrication variations.

## 6.2 Future Works

### 6.2.1 Fabrication Variation Mitigation

A key point of this thesis is how prominent and impactful the fabrication variations are. We have analyzed several types of structures, WBGs in SiN, SWG-WBG and SWG-based WDM diplexer. All of them had significant deviations in their characterized results compared with simulations in ideal scenarios.

The typical way of mitigating fabrication variations is to use an iterative design and fabrication loop workflow, where we update the model parameters using characterized results. Such workflow was illustrated in Fig. 1.1. We started such a process in Chapter 3 by introducing new parameters. New fabrication runs would allow us to update the model with higher accuracy and analyze our model predictions. There have been works showing the assistance of deep learning in the parametrization and model update [159], however, they are often very complex to implement and do not yet guarantee better results.

The parameter deviation we applied in the WDM diplexer is a form of anticipation of the standard design and fabrication workflow shown in Fig. 1.1. Although we had not fabricated any of the WDM diplexers before, we knew from earlier experiences with other SWG structures that we should expect a significant wavelength shift in the characterized results (a blue shift, specifically). We applied parameter variations to the fabricated devices that could correct the expected deviations. With new fabrication runs, we could improve the simulated model by incorporating new parameters and fine-tuning the parameters to the desired performance. The same could be done for the Sampled SWG-WBG.

### 6.2.2 Sampled Subwavelength Grating Waveguide Bragg Gratings

After showing the feasibility of the device, we can explore more complex versions. For example, we can explore chirped sampling functions, and apodized BG sections, which can be achieved by applying an apodization function to the loading segments' gap distances. We can also try different configurations of loading segment positioning, in order to reduce the impact of the fabrication variations. Other forms of BGs that have been presented can also be explored in the SWG platform, such as superstructured BGs [160].

Because of the lower effective index provided by SWG structures, weak peak-reflectivity random WBGs might offer a better path for innovation. The SWG structures also offer other parameters that are also capable of randomizing the WBG devices. Also, placing a replica of one of the random devices at another place in the die, which usually increases fabrication variations, would allow us to benchmark the correlation between devices.

### 6.2.3 WDM Diplexer for 1310 nm and 1550 nm Channels

The fact that our WDM diplexer uses standard SWG waveguides for its SDCs allows us to now explore a polarization-independent version of the device by simply tilting the SWG segments [134, 145]. Tilting the segments will change the effective index of the SWG waveguide, so it will require another optimization process. Moreover, the tilting angle that allows for zero-birefringence operation in the fabricated device is expected to diverge from the one determined in simulation [134], so an optimized device will require some empirical trials.

Another possibility of building upon the diplexer is to build a triplexer by cascading another SDC. This could be done for 1490 nm or 2  $\mu\text{m}$  channels, depending on application demand.

We have also shown the optimized design with a much more compact footprint. Although its characterized results were not as good as we expected, they show that the larger SWG segments grant more robustness to fabrication variations.



## References

- [1] A. D. Bristow, N. Rotenberg, and H. M. Van Driel, “Two-photon absorption and Kerr coefficients of silicon for 850–2200 nm,” *Applied Physics Letters*, vol. 90, no. 19, p. 191104, 2007.
- [2] K. Ikeda, R. E. Saperstein, N. Alic, and Y. Fainman, “Thermal and Kerr nonlinear properties of plasma-deposited silicon nitride/silicon dioxide waveguides,” *Optics Express*, vol. 16, no. 17, pp. 12987–12994, 2008.
- [3] C. J. Krückel, A. Fülöp, T. Klintberg, J. Bengtsson, P. A. Andrekson, *et al.*, “Linear and nonlinear characterization of low-stress high-confinement silicon-rich nitride waveguides,” *Optics Express*, vol. 23, no. 20, pp. 25827–25837, 2015.
- [4] L. Tsybeskov, D. J. Lockwood, and M. Ichikawa, “Silicon photonics: CMOS going optical [scanning the issue],” *Proceedings of the IEEE*, vol. 97, no. 7, pp. 1161–1165, 2009.
- [5] R. Soref and J. Lorenzo, “All-silicon active and passive guided-wave components for  $\lambda = 1.3$  and  $1.6$   $\mu\text{m}$ ,” *IEEE Journal of Quantum Electronics*, vol. 22, pp. 873–879, June 1986.

- [6] M. Lipson, “Next-generation silicon photonics,” (New York Academy of Sciences), 7 2018. Fifth annual Blavatnik Science Symposium, at the New York Academy of Sciences. Available at [www.youtube.com/watch?v=vxkaLrltSmU](http://www.youtube.com/watch?v=vxkaLrltSmU) as of May 2019.
- [7] R. Soref, “The past, present, and future of silicon photonics,” *IEEE Journal of Selected Topics in Quantum Electronics*, vol. 12, no. 6, pp. 1678–1687, 2006.
- [8] G. Reed, L. Jinhua, C. Tang, L. Chenglu, P. Hemment, and A. Rickman, “Silicon on insulator optical waveguides formed by direct wafer bonding,” *Materials Science and Engineering: B*, vol. 15, no. 2, pp. 156–159, 1992.
- [9] F. Y. Gardes, G. T. Reed, N. Emerson, and C. Png, “A sub-micron depletion-type photonic modulator in silicon on insulator,” *Optics Express*, vol. 13, pp. 8845–8854, Oct 2005.
- [10] G. T. Reed, G. Mashanovich, F. Y. Gardes, and D. J. Thomson, “Silicon optical modulators,” *Nature Photonics 2010 4:8*, vol. 4, pp. 518–526, 7 2010.
- [11] X. Sun, J. Liu, L. C. Kimerling, and J. Michel, “Toward a germanium laser for integrated silicon photonics,” *IEEE Journal of Selected Topics in Quantum Electronics*, vol. 16, no. 1, pp. 124–131, 2009.
- [12] N. Fujioka, T. Chu, and M. Ishizaka, “Compact and low power consumption hybrid integrated wavelength tunable laser module using silicon waveguide resonators,” *Journal of Lightwave Technology*, vol. 28, no. 21, pp. 3115–3120, 2010.
- [13] X. Xiao, M. Li, L. Wang, D. Chen, Q. Yang, and S. Yu, “High speed silicon photonic modulators,” in *Optical Fiber Communication Conference*, p. Tu2H.1, Optica Publishing Group, 2017.

- 
- [14] R. Sabella, “Silicon photonics for 5G and future networks,” *IEEE Journal of Selected Topics in Quantum Electronics*, vol. 26, no. 2, pp. 1–11, 2019.
- [15] R. C. Yu and D. Pan, “Silicon photonics applications for 5G and data centers,” in *Optical Fiber Communication Conference*, pp. M3A–5, Optica Publishing Group, 2021.
- [16] X. Guan, W. Shi, J. Liu, P. Tan, J. Slevinsky, and L. A. Rusch, “Silicon photonics in optical access networks for 5G communications,” *IEEE Communications Magazine*, vol. 59, no. 6, pp. 126–131, 2021.
- [17] P. Iovanna, A. Bigongiari, F. Cavaliere, A. Bianchi, F. Testa, S. Marconi, M. Romagnoli, V. Sorianello, A. Sgambelluri, F. Denis Le Coarer, *et al.*, “Optical components for transport network enabling the path to 6G,” *Journal of Lightwave Technology*, vol. 40, no. 2, pp. 527–537, 2021.
- [18] M. Fujita, “Advanced terahertz devices and systems toward 6G and beyond,” in *2021 8th NAFOSTED Conference on Information and Computer Science (NICS)*, pp. xxiv–xxiv, IEEE, 2021.
- [19] A. E. J. Lim, J. Song, Q. Fang, C. Li, X. Tu, N. Duan, K. K. Chen, R. P. C. Tern, and T. Y. Liow, “Review of silicon photonics foundry efforts,” *IEEE Journal of Selected Topics in Quantum Electronics*, vol. 20, no. 4, pp. 405–416, 2013.
- [20] D. Marpaung, J. Yao, and J. Capmany, “Integrated microwave photonics,” *Nature Photonics*, vol. 13, no. 2, pp. 80–90, 2019.
- [21] R. Maram, S. Kaushal, J. Azaña, and L. R. Chen, “Recent trends and advances of silicon-based integrated microwave photonics,” *Photonics*, vol. 6, no. 1, 2019.

- [22] D. Zhu and J. Yao, "Dual-chirp microwave waveform generation using a dual-parallel mach-zehnder modulator," *IEEE Photonics Technology Letters*, vol. 27, no. 13, pp. 1410–1413, 2015.
- [23] S. Pan, X. Ye, Y. Zhang, and F. Zhang, "Microwave photonic array radars," *IEEE Journal of Microwaves*, vol. 1, no. 1, pp. 176–190, 2021.
- [24] O. Pfister, "Continuous-variable quantum computing in the quantum optical frequency comb," *Journal of Physics B: Atomic, Molecular and Optical Physics*, vol. 53, no. 1, p. 012001, 2019.
- [25] W. Hu and F. Li, "Scaling beyond 7nm node: An overview of gate-all-around fets," in *2021 9th International Symposium on Next Generation Electronics (ISNE)*, pp. 1–6, IEEE, 2021.
- [26] A. E. Willner, S. Khaleghi, M. R. Chitgarha, and O. F. Yilmaz, "All-optical signal processing," *Journal of Lightwave Technology*, vol. 32, no. 4, pp. 660–680, 2014.
- [27] S. Wabnitz and B. Eggleton, *All-Optical Signal Processing: Data Communication and Storage Applications*. Springer Series in Optical Sciences, Springer International Publishing, 2015.
- [28] M. I. Cheema, C. Shi, A. M. Armani, and A. G. Kirk, "Optimizing the signal to noise ratio of microcavity sensors," *IEEE Photonics Technology Letters*, vol. 26, no. 20, pp. 2023–2026, 2014.
- [29] V. Passaro, F. Dell'Olio, and F. De Leonardis, "Electromagnetic field photonic sensors," *Progress in Quantum Electronics*, vol. 30, no. 2-3, pp. 45–73, 2006.

- [30] U. Willer and W. Schade, "Photonic sensor devices for explosive detection," *Analytical and Bioanalytical Chemistry*, vol. 395, no. 2, pp. 275–282, 2009.
- [31] S. E. S. Abd El Ghany, W. M. Nouman, Z. S. Matar, Z. A. Zaky, and A. H. Aly, "Optimized bio-photonic sensor using 1D-photonic crystals as a blood hemoglobin sensor," *Physica Scripta*, vol. 96, no. 3, p. 035501, 2020.
- [32] P. Sharan, S. Bharadwaj, F. D. Gudagunti, and P. Deshmukh, "Design and modelling of photonic sensor for cancer cell detection," in *2014 International Conference on the IMPact of E-Technology on US (IMPETUS)*, pp. 20–24, IEEE, 2014.
- [33] S. A. Kolpakov, N. T. Gordon, C. Mou, and K. Zhou, "Toward a new generation of photonic humidity sensors," *Sensors*, vol. 14, no. 3, pp. 3986–4013, 2014.
- [34] C. Liao and D. Wang, "Review of femtosecond laser fabricated fiber Bragg gratings for high temperature sensing," *Photonic Sensors*, vol. 3, no. 2, pp. 97–101, 2013.
- [35] J. G. Teixeira, I. T. Leite, S. Silva, and O. Frazão, "Advanced fiber-optic acoustic sensors," *Photonic Sensors*, vol. 4, no. 3, pp. 198–208, 2014.
- [36] J. Doylend and S. Gupta, "An overview of silicon photonics for LIDAR," *Silicon Photonics XV*, vol. 11285, pp. 109–115, 2020.
- [37] J. Hecht, "LIDAR for self-driving cars," *Optics and Photonics News*, vol. 29, no. 1, pp. 26–33, 2018.
- [38] W. Stutius and W. Streifer, "Silicon nitride films on silicon for optical waveguides," *Applied Optics*, vol. 16, no. 12, pp. 3218–3222, 1977.

- [39] H. El Dirani, M. Casale, S. Kerdiles, C. Socquet-Clerc, X. Letartre, C. Monat, and C. Sciancalepore, “Crack-free silicon-nitride-on-insulator nonlinear circuits for continuum generation in the C-band,” in *2018 IEEE Photonics Conference (IPC)*, pp. 1–4, IEEE, 2018.
- [40] C. J. Krückel, *Integrated Nonlinear Optics in Silicon Nitride Waveguides*. PhD thesis, Chalmers University of Technology, 2017.
- [41] L. B. Soldano and E. C. Pennings, “Optical multi-mode interference devices based on self-imaging: principles and applications,” *Journal of lightwave technology*, vol. 13, no. 4, pp. 615–627, 1995.
- [42] P. Muñoz, G. Micó, L. A. Bru, D. Pastor, D. Pérez, J. D. Doménech, J. Fernández, R. Baños, B. Gargallo, R. Alemany, *et al.*, “Silicon nitride photonic integration platforms for visible, near-infrared and mid-infrared applications,” *Sensors*, vol. 17, no. 9, p. 2088, 2017.
- [43] J. F. Bauters, M. J. Heck, D. D. John, J. S. Barton, C. M. Bruinink, A. Leinse, R. G. Heideman, D. J. Blumenthal, and J. E. Bowers, “Planar waveguides with less than 0.1 dB/m propagation loss fabricated with wafer bonding,” *Optics Express*, vol. 19, no. 24, pp. 24090–24101, 2011.
- [44] D. J. Blumenthal, R. Heideman, D. Geuzebroek, A. Leinse, and C. Roeloffze, “Silicon nitride in silicon photonics,” *Proceedings of the IEEE Special Issue on Silicon Photonics (Invited)*, 2018.
- [45] W. Lanford and M. Rand, “The hydrogen content of plasma-deposited silicon nitride,” *Journal of Applied Physics*, vol. 49, no. 4, pp. 2473–2477, 1978.

- [46] G. Lucovsky, P. Richard, D. Tsu, S. Lin, and R. Markunas, “Deposition of silicon dioxide and silicon nitride by remote plasma enhanced chemical vapor deposition,” *Journal of Vacuum Science & Technology A: Vacuum, Surfaces, and Films*, vol. 4, no. 3, pp. 681–688, 1986.
- [47] A. E. Kaloyeros, F. A. Jové, J. Goff, and B. Arkles, “Silicon nitride and silicon nitride-rich thin film technologies: trends in deposition techniques and related applications,” *ECS Journal of Solid State Science and Technology*, vol. 6, no. 10, p. P691, 2017.
- [48] D. P. Nair and M. Ménard, “Compact and fabrication tolerant silicon strip-slot waveguide mode converter,” in *Advanced Photonics Congress*, p. ITh2B.4, Optica Publishing Group, 2022.
- [49] B. J. Eggleton, B. Luther Davies, and K. Richardson, “Chalcogenide photonics,” *Nature Photonics*, vol. 5, no. 3, pp. 141–148, 2011.
- [50] X. Gai, T. Han, A. Prasad, S. Madden, D. Y. Choi, R. Wang, D. Bulla, and B. Luther Davies, “Progress in optical waveguides fabricated from chalcogenide glasses,” *Optics Express*, vol. 18, no. 25, pp. 26635–26646, 2010.
- [51] D. Liang and J. E. Bowers, “Recent progress in heterogeneous III-V-on-silicon photonic integration,” *Light: Advanced Manufacturing*, vol. 2, no. 1, pp. 59–83, 2021.
- [52] D. Zhu, L. Shao, M. Yu, R. Cheng, B. Desiatov, C. Xin, Y. Hu, J. Holzgrafe, S. Ghosh, A. Shams Ansari, *et al.*, “Integrated photonics on thin-film lithium niobate,” *Advances in Optics and Photonics*, vol. 13, no. 2, pp. 242–352, 2021.
- [53] K. Okamoto, “Progress and technical challenge for planar waveguide devices: silica and silicon waveguides,” *Laser & Photonics Reviews*, vol. 6, no. 1, pp. 14–23, 2012.

- 
- [54] L. Chrostowski, X. Wang, J. Flueckiger, Y. Wu, Y. Wang, and S. T. Fard, “Impact of fabrication non-uniformity on chip-scale silicon photonic integrated circuits,” in *Optical Fiber Communication Conference*, pp. Th2A–37, Optical Society of America, 2014.
- [55] M. Nikdast, G. Nicolescu, J. Trajkovic, and O. Liboiron-Ladouceur, “Chip-scale silicon photonic interconnects: A formal study on fabrication non-uniformity,” *Journal of Lightwave Technology*, vol. 34, no. 16, pp. 3682–3695, 2016.
- [56] A. Mirza, F. Sunny, P. Walsh, K. Hassan, S. Pasricha, and M. Nikdast, “Silicon photonic microring resonators: A comprehensive design-space exploration and optimization under fabrication-process variations,” *IEEE Transactions on Computer-Aided Design of Integrated Circuits and Systems*, 2021.
- [57] W. Bogaerts, P. De Heyn, T. Van Vaerenbergh, K. De Vos, S. Kumar Selvaraja, T. Claes, P. Dumon, P. Bienstman, D. Van Thourhout, and R. Baets, “Silicon microring resonators,” *Laser & Photonics Reviews*, vol. 6, no. 1, pp. 47–73, 2012.
- [58] J. K. Sahota, N. Gupta, and D. Dhawan, “Fiber Bragg grating sensors for monitoring of physical parameters: a comprehensive review,” *Optical Engineering*, vol. 59, no. 6, p. 060901, 2020.
- [59] D. Lo Presti, C. Massaroni, C. S. Jorge Leitão, M. De Fátima Domingues, M. Sypabekova, D. Barrera, I. Floris, L. Massari, C. M. Oddo, S. Sales, I. I. Iordachita, D. Tosi, and E. Schena, “Fiber Bragg gratings for medical applications and future challenges: A review,” *IEEE Access*, vol. 8, pp. 156863–156888, 2020.
- [60] X. Shu, B. A. L. Gwandu, Y. Liu, L. Zhang, and I. Bennion, “Sampled fiber Bragg grating for simultaneous refractive-index and temperature measurement,” *Optics Letters*, vol. 26, pp. 774–776, Jun 2001.

- [61] J. Li, G. Chen, P. Ma, L.-P. Sun, C. Wu, and B.-O. Guan, “Sampled Bragg gratings formed in helically twisted fibers and their potential application for the simultaneous measurement of mechanical torsion and temperature,” *Optics Express*, vol. 26, pp. 12903–12911, May 2018.
- [62] L. Zhang, F. Yan, T. Feng, W. Han, Y. Bai, Z. Bai, D. Cheng, H. Zhou, and Y. Suo, “Wavelength-tunable thulium-doped fiber laser with sampled fiber Bragg gratings,” *Optics & Laser Technology*, vol. 120, p. 105707, 2019.
- [63] X. Wang, W. Shi, R. Vafaei, N. A. F. Jaeger, and L. Chrostowski, “Uniform and sampled Bragg gratings in SOI strip waveguides with sidewall corrugations,” *IEEE Photonics Technology Letters*, vol. 23, no. 5, pp. 290–292, 2011.
- [64] H. Shu, B. Shen, Q. Deng, M. Jin, X. Wang, and Z. Zhou, “A design guideline for mode (de) multiplexer based on integrated tapered asymmetric directional coupler,” *IEEE Photonics Journal*, vol. 11, no. 5, pp. 1–12, 2019.
- [65] Z. Wang, B. Taglietti, M. Ma, and L. R. Chen, “A silicon photonic optical add-drop multiplexer based on mode-selective device and Bragg grating,” in *Conference on Lasers and Electro-Optics/Pacific Rim*, pp. Th2C–3, Optica Publishing Group, 2018.
- [66] N. Kazanskiy, M. Butt, and S. Khonina, “Silicon photonic devices realized on refractive index engineered subwavelength grating waveguides—a review,” *Optics & Laser Technology*, vol. 138, p. 106863, 2021.
- [67] P. J. Bock, P. Cheben, J. H. Schmid, J. Lapointe, A. Delâge, D. X. Xu, S. Janz, A. Densmore, and T. J. Hall, “Subwavelength grating crossings for silicon wire waveguides,” *Optics Express*, vol. 18, pp. 16146–16155, Jul 2010.

- [68] C. R. Pollock and M. Lipson, *Integrated Photonics*. Kluwer Academic, 2003.
- [69] K. S. Chiang, “Performance of the effective-index method for the analysis of dielectric waveguides,” *Opt. Lett.*, vol. 16, pp. 714–716, May 1991.
- [70] L. Chrostowski and M. Hochberg, *Silicon Photonics Design*. Cambridge University Press, 2015.
- [71] S. Miller, “Coupled wave theory and waveguide applications,” *Bell System Technical Journal*, vol. 33, no. 3, pp. 661–719, 1954.
- [72] B. Eggleton, P. Krug, L. Poladian, and F. Ouellette, “Long periodic superstructure Bragg gratings in optical fibers,” *Electronic Letters*, vol. 30, no. 19, 1994.
- [73] J. Hubner, D. Zauner, and M. Kristensen, “Strong sampled Bragg gratings for WDM applications,” *IEEE Photonics Technology Letters*, vol. 10, no. 4, pp. 552–554, 1998.
- [74] Y. Huang and J. Yao, “Time-delay signature suppressed microwave chaotic signal generation based on an optoelectronic oscillator incorporating a randomly sampled fiber Bragg grating,” *International Topical Meeting on Microwave Photonics*, pp. 237–240, 2020.
- [75] P. J. Bock, P. Cheben, J. H. Schmid, J. Lapointe, A. Delâge, S. Janz, G. C. Aers, D. X. Xu, A. Densmore, and T. J. Hall, “Subwavelength grating periodic structures in silicon-on-insulator: a new type of microphotonic waveguide,” *Optics Express*, vol. 18, pp. 20251–20262, Sep 2010.
- [76] R. Halir, A. Ortega Monux, D. Benedikovic, G. Z. Mashanovich, J. G. Wangüemert Pérez, J. H. Schmid, I. Molina Fernandez, and P. Cheben,

- “Subwavelength-grating metamaterial structures for silicon photonic devices,” *Proceedings of the IEEE*, vol. 106, no. 12, pp. 2144–2157, 2018.
- [77] Z. Ruan, L. Shen, S. Zheng, and J. Wang, “Subwavelength grating slot (SWGS) waveguide on silicon platform,” *Optics Express*, vol. 25, no. 15, pp. 18250–18264, 2017.
- [78] R. Halir, A. Ortega Monux, J. H. Schmid, C. Alonso Ramos, J. Lapointe, D. X. Xu, J. G. Wangüemert Pérez, I. Molina Fernandez, and S. Janz, “Recent advances in silicon waveguide devices using sub-wavelength gratings,” *IEEE Journal of Selected Topics in Quantum Electronics*, vol. 20, no. 4, pp. 279–291, 2013.
- [79] P. T. Dang, J. Kim, and J. H. Lee, “Negative dispersion of a form birefringence in subwavelength gratings,” *Optics Express*, vol. 30, no. 11, pp. 18287–18299, 2022.
- [80] F. Bloch, “Über die quantenmechanik der elektronen in kristallgittern,” *Zeitschrift für physik*, vol. 52, no. 7, pp. 555–600, 1929.
- [81] “Sub-wavelength grating bandstructures.” <https://www.lumerical.com/learn/video/swg-bandstructures/>. Accessed: 2022-09-09.
- [82] J. Wang, I. Glesk, and L. R. Chen, “Subwavelength grating filtering devices,” *Optics Express*, vol. 22, no. 13, pp. 15335–15345, 2014.
- [83] J. Čtyroký, J. G. W. Pérez, P. Kwiecien, I. Richter, J. Litvik, J. H. Schmid, I. nigo Molina Fernández, A. O. M. nux, M. Dado, and P. Cheben, “Design of narrowband Bragg spectral filters in subwavelength grating metamaterial waveguides,” *Optics Express*, vol. 26, pp. 179–194, Jan 2018.

- [84] H. Sun, B. Taglietti, Y. Wang, and L. R. Chen, “Integrated subwavelength grating waveguide Bragg gratings for microwave photonics,” *Journal of Lightwave Technology*, vol. 40, no. 20, pp. 6636–6649, 2022.
- [85] H. Sun, Y. Wang, and L. R. Chen, “Integrated discretely tunable optical delay line based on step-chirped subwavelength grating waveguide Bragg gratings,” *Journal of Lightwave Technology*, vol. 38, no. 19, pp. 5551–5560, 2020.
- [86] Z. Du, C. Xiang, T. Fu, M. Chen, S. Yang, J. E. Bowers, and H. Chen, “Silicon nitride chirped spiral Bragg grating with large group delay,” *APL Photonics*, vol. 5, no. 10, p. 101302, 2020.
- [87] C. Husko, A. Ducharme, N. M. Fahrenkopf, and J. R. Guest, “Phase-shifted Bragg gratings in a foundry silicon nitride platform,” *OSA Continuum*, vol. 4, no. 3, pp. 933–939, 2021.
- [88] P. T. Callahan, Purnawirman, T. N. Adam, G. Leake, D. Coolbaugh, M. R. Watts, and F. X. Kärtner, “Double-chirped Bragg gratings in a silicon nitride waveguide,” in *Conference on Lasers and Electro-Optics*, p. SF1E.7, Optica Publishing Group, 2016.
- [89] Z. Zhang, D. Liu, D. de Felipe, A. Liu, N. Keil, and N. Grote, “Polymer embedded silicon nitride thermally tunable Bragg grating filters,” *Applied Physics Letters*, vol. 102, no. 18, p. 181105, 2013.
- [90] P. Primiani, F. Van Dijk, S. Boust, J. M. Fedeli, F. Duport, C. Gomez, J. F. Paret, A. Garreau, K. Mekhazni, and C. Fortin, “Silicon nitride Bragg grating with joule thermal tuning for external cavity lasers,” *2019 IEEE Photonics Conference, IPC 2019 - Proceedings*, vol. 31, no. 12, pp. 983–986, 2019.

- [91] J. Cauchon, J. St Yves, F. Menard, and W. Shi, "Silicon nitride band splitter based on multimode Bragg gratings," in *2021 Optical Fiber Communications Conference and Exhibition (OFC)*, pp. 1–3, IEEE, 2021.
- [92] R. G. F. Baets, A. Z. Subramanian, S. Clemmen, B. Kuyken, P. Bienstman, N. Le Thomas, G. Roelkens, D. Van Thourhout, P. Helin, and S. Severi, "Silicon photonics: Silicon nitride versus silicon-on-insulator," in *Optical Fiber Communication Conference*, 2016.
- [93] E. Durán Valdeiglesias, S. Guerber, D. Oser, X. L. Roux, D. Benedikovic, D. Pérez Galacho, N. Vulliet, S. Cremer, S. Monfray, E. Cassan, D. Marris Morini, C. Baudot, F. Boeuf, L. Vivien, and C. Alonso Ramos, "Dual-polarization silicon nitride Bragg filters with low thermal sensitivity," *Optics Letters*, vol. 44, no. 18, p. 4578, 2019.
- [94] K. J. Yoon, S. M. Wiederhorn, and W. E. Luecke, "Comparison of tensile and compressive creep behavior in silicon nitride," *Journal of the American Ceramic Society*, vol. 83, no. 8, pp. 2017–2022, 2000.
- [95] W. E. Luecke and S. M. Wiederhorn, "A new model for tensile creep of silicon nitride," *Journal of the American Ceramic Society*, vol. 82, no. 10, pp. 2769–2778, 1999.
- [96] R. L. Edwards, G. Coles, and W. N. Sharpe, "Comparison of tensile and bulge tests for thin-film silicon nitride," *Experimental Mechanics*, vol. 44, no. 1, pp. 49–54, 2004.
- [97] J. F. Yang, G. J. Zhang, and T. Ohji, "Fabrication of low-shrinkage, porous silicon nitride ceramics by addition of a small amount of carbon," *Journal of the American Ceramic Society*, vol. 84, no. 7, pp. 1639–1641, 2001.

- [98] W. M. Zhang, Y. G. Wang, J. Li, J. M. Xue, H. Ji, Q. Ouyang, J. Xu, and Y. Zhang, “Controllable shrinking and shaping of silicon nitride nanopores under electron irradiation,” *Applied Physics Letters*, vol. 90, no. 16, p. 163102, 2007.
- [99] T. Wakihara, H. Yabuki, J. Tatami, K. Komeya, T. Meguro, H. Hyuga, and H. Kita, “In situ measurement of shrinkage during postreaction sintering of reaction-bonded silicon nitride,” *Journal of the American Ceramic Society*, vol. 91, no. 10, pp. 3413–3415, 2008.
- [100] H. J. Kleebe, M. K. Cinibulk, R. M. Cannon, and M. Rühle, “Statistical analysis of the intergranular film thickness in silicon nitride ceramics,” *Journal of the American Ceramic Society*, vol. 76, no. 8, pp. 1969–1977, 1993.
- [101] J. Kennedy and R. Eberhart, “Particle swarm optimization,” in *Proceedings of ICNN’95-international conference on neural networks*, vol. 4, pp. 1942–1948, IEEE, 1995.
- [102] “Ansys optics – device suite – optimizations and sweeps – optimization utility – particle swarm optimization.” <https://optics.ansys.com/hc/en-us/articles/360034922953-Optimization/>. Accessed: 2023-03-29.
- [103] R. Cheng and L. Chrostowski, “Spectral design of silicon integrated Bragg gratings: A tutorial,” *Journal of Lightwave Technology*, vol. 39, no. 3, pp. 712–729, 2020.
- [104] H. Zhang, C. Li, X. Tu, J. Song, H. Zhou, X. Luo, Y. Huang, M. Yu, and G. Lo, “Efficient silicon nitride grating coupler with distributed Bragg reflectors,” *Optics Express*, vol. 22, no. 18, pp. 21800–21805, 2014.

- [105] C. R. Doerr, L. Chen, Y. K. Chen, and L. L. Buhl, “Wide bandwidth silicon nitride grating coupler,” *IEEE Photonics Technology Letters*, vol. 22, no. 19, pp. 1461–1463, 2010.
- [106] J. Hong, A. M. Spring, F. Qiu, and S. Yokoyama, “A high efficiency silicon nitride waveguide grating coupler with a multilayer bottom reflector,” *Scientific Reports*, vol. 9, no. 1, pp. 1–8, 2019.
- [107] J. C. Mikkelsen, A. Bois, T. Lordello, D. Mahgerefteh, S. Menezo, and J. K. S. Poon, “Polarization-insensitive silicon nitride Mach-Zehnder lattice wavelength demultiplexers for CWDM in the O-band,” *Optics Express*, vol. 26, pp. 30076–30084, Nov 2018.
- [108] G. Gao, D. Chen, S. Tao, Y. Zhang, S. Zhu, X. Xiao, and J. Xia, “Silicon nitride O-band (de) multiplexers with low thermal sensitivity,” *Optics Express*, vol. 25, no. 11, pp. 12260–12267, 2017.
- [109] B. Bhandari, C. S. Im, O. R. Sapkota, and S. S. Lee, “Highly efficient broadband silicon nitride polarization beam splitter incorporating serially cascaded asymmetric directional couplers,” *Optics Letters*, vol. 45, no. 21, pp. 5974–5977, 2020.
- [110] S. Guerber, C. Alonso Ramos, D. Benedikovic, E. Durán Valdeiglesias, X. Le Roux, N. Vulliet, E. Cassan, D. Marris Morini, C. Baudot, F. Boeuf, *et al.*, “Broadband polarization beam splitter on a silicon nitride platform for O-band operation,” *IEEE Photonics Technology Letters*, vol. 30, no. 19, pp. 1679–1682, 2018.
- [111] J. Feng and R. Akimoto, “A three-dimensional silicon nitride polarizing beam splitter,” *IEEE Photonics Technology Letters*, vol. 26, no. 7, pp. 706–709, 2014.

- 
- [112] J. Zhan, J. Brock, S. Veilleux, and M. Dagenais, “Silicon nitride polarization beam splitter based on polarization-independent MMIs and apodized Bragg gratings,” *Optics Express*, vol. 29, no. 10, pp. 14476–14485, 2021.
- [113] C. Wang, J. Azana, and L. R. Chen, “Efficient technique for increasing the channel density in multiwavelength sampled fiber Bragg grating filters,” *IEEE Photonics Technology Letters*, vol. 16, no. 8, pp. 1867–1869, 2004.
- [114] J. A. na, C. Wang, and L. R. Chen, “Spectral self-imaging phenomena in sampled Bragg gratings,” *Journal of the Optical Society of America B*, vol. 22, pp. 1829–1841, Sep 2005.
- [115] C. H. Wang, L. R. Chen, and P. W. E. Smith, “Analysis of chirped-sampled and sampled-chirped fiber Bragg gratings,” *Applied Optics*, vol. 41, no. 9, pp. 1654–1660, 2002.
- [116] X. F. Chen, C. C. Fan, Y. Luo, S. Z. Xie, and S. Hu, “Novel flat multichannel filter based on strongly chirped sampled fiber Bragg grating,” *IEEE Photonics Technology Letters*, vol. 12, no. 11, pp. 1501–1503, 2000.
- [117] Y. Dai, X. Chen, J. Sun, and S. Xie, “Wideband multichannel dispersion compensation based on a strongly chirped sampled Bragg grating and phase shifts,” *Optics Letters*, vol. 31, no. 3, pp. 311–313, 2006.
- [118] Y. Dai, X. Chen, X. Xu, C. Fan, and S. Xie, “High channel-count comb filter based on chirped sampled fiber Bragg grating and phase shift,” *IEEE Photonics Technology Letters*, vol. 17, no. 5, pp. 1040–1042, 2005.

- 
- [119] Z. Wang, Y. Cui, B. Yun, and C. Lu, “Multiwavelength generation in a Raman fiber laser with sampled Bragg grating,” *IEEE Photonics Technology Letters*, vol. 17, no. 10, pp. 2044–2046, 2005.
- [120] P. Petropoulos, M. Ibsen, M. N. Zervas, and D. J. Richardson, “Generation of a 40-GHz pulse stream by pulse multiplication with a sampled fiber Bragg grating,” *Optics Letters*, vol. 25, no. 8, pp. 521–523, 2000.
- [121] T. Buck, M. Müller, A. Perez Grassi, and A. Koch, “Detection of aliasing in sampled dynamic fiber Bragg grating signals recorded by spectrometers,” *Measurement*, vol. 44, no. 6, pp. 1053–1058, 2011.
- [122] I. Giuntoni, P. Balladares, R. Steingrüber, J. Bruns, and K. Petermann, “WDM Multi-Channel Filter Based On Sampled Gratings In Silicon-on-Insulator,” in *Optical Fiber Communication Conference/National Fiber Optic Engineers Conference 2011*, p. OThV3, Optica Publishing Group, 2011.
- [123] Z. Huang and Y. Wang, “Four-wavelength III-V/SOI heterogeneous integrated laser based on sampled Bragg grating for CWDM,” *IEEE Photonics Journal*, vol. 5, no. 5, pp. 1501906–1501906, 2013.
- [124] S. Liu, Y. Shi, L. Hao, R. Xiao, and X. Chen, “Experimental demonstration of the anti-symmetric sampled Bragg grating,” *IEEE Photonics Technology Letters*, vol. 29, no. 4, pp. 353–356, 2017.
- [125] H. Deng, P. Lu, S. Mihailov, and J. Yao, “Photonic generation of pseudo random microwave waveform based on a random fiber grating,” *Optical Fiber Communications Conference and Exposition (OFC)*, 2018.

- [126] M. Gagné and R. Kashyap, “Random fiber Bragg grating Raman fiber laser,” *Optics Letters*, vol. 39, pp. 2755–2758, May 2014.
- [127] H. Yin, A. Gbadebo, and E. G. Turitsyna, “Top-hat random fiber Bragg grating,” *Optics Letters*, vol. 40, no. 15, pp. 3592–3594, 2015.
- [128] M. Gagné and R. Kashyap, “Demonstration of a 3 mW threshold Er-doped random fiber laser based on a unique fiber Bragg grating,” *Optics Express*, vol. 17, no. 21, pp. 19067–19074, 2009.
- [129] N. Lizárraga, N. P. Puente, E. I. Chaikina, T. A. Leskova, and E. R. Méndez, “Single-mode Er-doped fiber random laser with distributed Bragg grating feedback,” *Optics Express*, vol. 17, pp. 395–404, Jan 2009.
- [130] W. L. Zhang, R. Ma, C. H. Tang, Y. J. Rao, X. P. Zeng, Z. J. Yang, Z. N. Wang, Y. Gong, and Y. S. Wang, “All optical mode controllable Er-doped random fiber laser with distributed Bragg gratings,” *Optics Letters*, vol. 40, pp. 3181–3184, Jul 2015.
- [131] C. Huang, X. Dong, N. Zhang, S. Zhang, and P. P. Shum, “Multiwavelength Brillouin-erbium random fiber laser incorporating a chirped fiber Bragg grating,” *IEEE Journal of Selected Topics in Quantum Electronics*, vol. 20, no. 5, pp. 294–298, 2014.
- [132] H. Sun and L. R. Chen, “Phase-shifted waveguide Bragg gratings enabled by subwavelength grating structures,” in *OSA Advanced Photonics Congress 2021*, p. IM2A.4, Optical Society of America, 2021.
- [133] H. Sun and L. R. Chen, “Polarization-dependent tuning of Bragg reflection enabled through tilted subwavelength grating waveguide Bragg gratings,” *Optics Letters*, vol. 46, no. 6, pp. 1450–1453, 2021.

- 
- [134] H. Sun and L. R. Chen, “Polarization independent waveguide Bragg gratings using tilted subwavelength grating waveguides,” in *Conference on Lasers and Electro-Optics*, p. JW3B.14, Optica Publishing Group, 2022.
- [135] H. Okayama, Y. Onawa, D. Shimura, H. Yaegashi, and H. Sasaki, “Silicon waveguide polarization rotator sampled Bragg grating,” *Optics Letters*, vol. 42, no. 11, pp. 2142–2144, 2017.
- [136] J. M. L. González, A. S. Postigo, A. H. ElHouati, A. O. Moñux, J. G. W. Pérez, J. H. Schmid, P. Cheben, Íñigo Molina Fernández, and R. Halir, “A review of silicon sub-wavelength gratings: building break-through devices with anisotropic metamaterials,” *Nanophotonics*, vol. 10, no. 11, pp. 2765–2797, 2021.
- [137] Y. Shi, J. Chen, and H. Xu, “Silicon-based on-chip diplexing/triplexing technologies and devices,” *Science China Information Sciences*, vol. 61, no. 8, pp. 1–15, 2018.
- [138] L. Xu, Y. Wang, D. Mao, E. ElFiky, Z. Xing, A. Kumar, M. G. Saber, M. Jacques, and D. V. Plant, “Broadband 1310/1550 nm wavelength demultiplexer based on a multimode interference coupler with tapered internal photonic crystal for the silicon-on-insulator platform,” *Optics Letters*, vol. 44, no. 7, pp. 1770–1773, 2019.
- [139] J. Chen, P. Liu, and Y. Shi, “An on-chip silicon compact triplexer based on cascaded tilted multimode interference couplers,” *Optics Communications*, vol. 410, pp. 483–487, 2018.
- [140] L. Liu, Q. Deng, and Z. Zhou, “An ultra-compact wavelength diplexer engineered by subwavelength grating,” *IEEE Photonics Technology Letters*, vol. 29, no. 22, pp. 1927–1930, 2017.

- [141] J. Zhang, L. Xu, D. Mao, Z. Xing, Y. D’Mello, M. Jacques, Y. Wang, S. Lessard, and D. V. Plant, “High-extinction-ratio and compact 1310/1550 nm wavelength diplexer on SOI platform based on an SWG-structured two-mode interference coupler,” *IEEE Photonics Journal*, vol. 14, no. 2, pp. 1–6, 2022.
- [142] Y. Shi, S. Anand, and S. He, “Design of a polarization insensitive triplexer using directional couplers based on submicron silicon rib waveguides,” *Journal of Lightwave Technology*, vol. 27, no. 11, pp. 1443–1447, 2009.
- [143] H. Xu and Y. Shi, “On-chip silicon triplexer based on asymmetrical directional couplers,” *IEEE Photonics Technology Letters*, vol. 29, no. 15, pp. 1265–1268, 2017.
- [144] J. Chen, L. Liu, and Y. Shi, “A polarization-insensitive dual-wavelength multiplexer based on bent directional couplers,” *IEEE Photonics Technology Letters*, vol. 29, no. 22, pp. 1975–1978, 2017.
- [145] J. M. Luque González, A. Herrero Bermello, A. Ortega Moñux, Í. Molina Fernández, A. V. Velasco, P. Cheben, J. H. Schmid, S. Wang, and R. Halir, “Tilted subwavelength gratings: controlling anisotropy in metamaterial nanophotonic waveguides,” *Optics Letters*, vol. 43, no. 19, pp. 4691–4694, 2018.
- [146] J. Chen and J. Xiao, “Compact silicon-based on-chip wavelength triplexer using directional couplers with double bridged subwavelength gratings,” *Applied Optics*, vol. 60, no. 30, pp. 9587–9593, 2021.
- [147] J. Chen, “A broadband wavelength demultiplexer assisted by SWG-based directional couplers,” *Optik*, vol. 202, p. 163602, 2020.

- [148] D. Zhu, H. Ye, Y. Liu, J. Li, and Z. Yu, “High-contrast and compact integrated wavelength diplexer based on subwavelength grating anisotropic metamaterial for 1550/2000 nm,” *IEEE Photonics Journal*, vol. 13, no. 2, pp. 1–10, 2021.
- [149] J. Liao, Y. Xie, T. Huang, and Z. Cheng, “Design and analysis of a compact subwavelength-grating-assisted 1.55/2  $\mu\text{m}$  wavelength demultiplexer,” *Applied Optics*, vol. 60, no. 16, pp. 4972–4975, 2021.
- [150] F. Zhang, H. Yun, Y. Wang, Z. Lu, L. Chrostowski, and N. A. Jaeger, “Compact broadband polarization beam splitter using a symmetric directional coupler with sinusoidal bends,” *Optics Letters*, vol. 42, no. 2, pp. 235–238, 2017.
- [151] C. Kaspar, J. Butschke, M. Irmscher, S. Martens, H. Sailer, R. Kirchner, V. A. Guzenko, H. Schiff, and J. N. Burghartz, “Adjustable sidewall slopes by electron-beam exposure layout,” *Journal of Vacuum Science & Technology B, Nanotechnology and Microelectronics: Materials, Processing, Measurement, and Phenomena*, vol. 35, no. 6, p. 06G501, 2017.
- [152] M. T. Wade, F. Pavanello, R. Kumar, C. M. Gentry, A. Atabaki, R. Ram, V. Stojanović, and M. A. Popović, “75% efficient wide bandwidth grating couplers in a 45 nm microelectronics cmos process,” in *2015 IEEE Optical Interconnects Conference (OI)*, pp. 46–47, IEEE, 2015.
- [153] J. Chen and Y. Shi, “An ultracompact silicon triplexer based on cascaded bent directional couplers,” *Journal of Lightwave Technology*, vol. 35, pp. 5260–5264, Dec 2017.
- [154] Y. Shi, S. Anand, and S. He, “A polarization-insensitive 1310/1550-nm demultiplexer based on sandwiched multimode interference waveguides,” *IEEE Photonics Technology Letters*, vol. 19, no. 22, pp. 1789–1791, 2007.

- 
- [155] Q. Zhang, S. Fu, J. Man, Z. Li, M. Cherchi, P. Heimala, M. Harjanne, S. Fei, M. Hiltunen, T. Aalto, *et al.*, “Low-loss and polarization-insensitive photonic integrated circuit based on micron-scale SOI platform for high density TDM PONs,” in *2017 Optical Fiber Communications Conference and Exhibition (OFC)*, pp. 1–3, IEEE, 2017.
- [156] D. Feng, N. N. Feng, H. Liang, W. Qian, C. C. Kung, J. Fong, and M. Asghari, “Monolithic WDM filter in silicon-on-insulator for diplexer/triplexer application,” in *Integrated Photonics and Nanophotonics Research and Applications*, p. ITuA4, Optica Publishing Group, 2008.
- [157] H. Deng, P. Lu, S. J. Mihailov, and J. Yao, “High-speed and high-resolution interrogation of a strain and temperature random grating sensor,” *Journal of Lightwave Technology*, vol. 36, no. 23, pp. 5587–5592, 2018.
- [158] M. Gagné and R. Kashyap, “Random fiber Bragg grating Raman fiber laser,” *Optics Letters*, vol. 39, no. 9, pp. 2755–2758, 2014.
- [159] S. So, T. Badloe, J. Noh, J. B. Abad, and J. Rho, “Deep learning enabled inverse design in nanophotonics,” *Nanophotonics*, vol. 9, no. 5, pp. 1041–1057, 2020.
- [160] J. S. Leng, W. Zhang, and J. A. R. Williams, “Optimization of superstructured fiber Bragg gratings for microwave photonic filters response,” *IEEE Photonics Technology Letters*, vol. 16, no. 7, pp. 1736–1738, 2004.

# Appendix A

## Bragg Gratings TMM Simulations

### A.1 Measured Refractive Indexes

Table A.1 shows samples at a few wavelengths of the refractive index obtained from ellipsometry measurements of the materials used in the devices shown in Chapter 3.

**Table A.1** Wavelength samples of the refractive index curves used in the simulations of Chapter 3 obtained from ellipsometry measurements.

$\lambda$ (nm)	Si <sub>3</sub> N <sub>4</sub>	Thermal dioxide	CVD dioxide
1400	1.9935	1.4448	1.4612
1430	1.9928	1.4445	1.4609
1460	1.9921	1.4441	1.4605
1490	1.9914	1.4438	1.4602
1520	1.9907	1.4434	1.4598
1550	1.99	1.4431	1.4595
1580	1.9893	1.4427	1.4591
1610	1.9886	1.4423	1.4587
1640	1.988	1.442	1.4584
1670	1.9873	1.4416	1.458
1700	1.9866	1.4412	1.4576

## A.2 Silicon Nitride Bragg Gratings Simulation Script

The following Matlab script applies TMM to simulate the SiN-WBGs discussed in Chapter 3. It requires loading a mat file containing a matrix named `mode_table` in which the first column defines the width of the waveguide, and the following columns are the effective index results from the FDE simulations for the corresponding mode. Loading several modes allows us to select the polarization mode.

Listing A.1 Silicon Nitride Apodized Bragg Gratings

```
1 %% Main script
2 % Apodized Bragg grating for SiN
3 % Simulates both the sinusoidal-shrunk gratings and square-profile.
4
5 global n1 n2 wl0 bg_p n_p loss wl n.matrix widths wg_width Delta_n neff
6
7 %% Loads the effective index
8 % The files Chalmers_600nm_neff.mat and Chalmers_630nm_neff.mat load the
9 % effective index vs width curves for a 600 nm thick and 630 nm thick film of
10 % SiN, respectively.
11
12 ModeStr = {'TE', 'TM'}; % Defines the polarization mode
13 neff_width_files = {'Chalmers_600nm_neff'}; % loads the neff vs W file
14 fileStr = {'standard'}; % resulting filename suffix
15 default_widths = [1000e-9]; % average waveguide width
16
17 bg_p = 438e-9; % Bragg grating period
18 DCs = [0.5 0.3 0.1]; % Duty cycle parameter introduced (longitudinal ...
    shrinkage)
```

```
19 n_p = 20000; % number of grating periods
20
21 fab_res = 1e-9; % fabrication resolution for error estimation
22 fab_var = [0, 0]; % Delta_n of random width var -- random length var;
23 resolution = 10e-12; % OSA res: 10ps
24 Dws = [20 100]*1e-9; % simulated corrugation depths
25
26 date = datestr(datetime(), 'yyyy-mm-dd');
27 dirname = ['Results/DC_' date]; % defines the results directory name
28 if ~exist(dirname, 'dir'), mkdir(dirname); end % creates the directory
29
30 for film_thickness = 1:length(neff_width_files) % runs simulations for ...
    all thicknesses
31     disp(['Starting simulations using ' neff_width_files{film_thickness}]);
32     load(neff_width_files{film_thickness});
33     widths = mode_table(:,1);
34     n_matrix = mode_table(:,2:end);
35     clear mode_table;
36     for Mode = 1:2
37         MODE = ModeStr{Mode};
38         disp(['Polarization mode: ' ModeStr{Mode}]);
39         wg_width = default_widths(film_thickness);
40
41         bw_sin = zeros(1, length(Dws)); % allocating variables
42         bw_sqr = zeros(1, length(Dws));
43         wlc_sin = zeros(1, length(Dws));
44         wlc_sqr = zeros(1, length(Dws));
45         Rsin = zeros(1, length(wl));
46         Tsin = zeros(1, length(wl));
47         Rsqr = zeros(1, length(wl));
```

```

48     Tsqr = zeros(1, length(wl));
49     for DCi = 1:length(DCs) % runs the simulation for several DC
50         DC = DCs(DCi);
51         L_shrink = (0.5 - DC)*bg_p;
52         disp(['Duty Cycle: ' num2str(DC)])
53         disp(['ON length: ' num2str((bg_p/2 - L_shrink)*1e9) ' nm'])
54         for i = 1:length(Dws) % runs for each corrugation depth
55             Dw = Dws(i);
56             disp(['Current corrugation depth: ' num2str(Dw*1e9) 'nm']);
57             bg_w1 = wg_width - Dw/2; % widths
58             bg_w2 = wg_width + Dw/2;
59             neff = interp1(widths, n_matrix(:,Mode), wg_width); % ...
60                 avg neff
61             ns = interp1(widths, n_matrix(:,Mode), [bg_w1, bg_w2]);
62             n1 = ns(1);
63             n2 = ns(2); clear ns; % interpolates neff for w1 and w2
64             ns = interp1(widths, n_matrix(:,Mode), [wg_width - ...
65                 fab_var, wg_width + fab_var]);
66             fab_var(1) = ns(2) - ns(1); % estimates the neff error ...
67                 due to fab. var.
68             Delta_n = n2 - n1;
69             n2 = neff + Delta_n/2; % centering neff instead of widths
70             n1 = neff - Delta_n/2;
71             loss = 0;
72             w10 = 2*neff*bg_p;
73             w1 = (w10 - 50e-9 : resolution : w10 + 50e-9);
74             [Rsin, Tsin] = apodized_sin(n_p, 0.35, L_shrink, fab_var);
75             [bw_sin(i), wlc_sin(i)] = fwhm(w1, Rsin);
76             [Rsqr, Tsqr] = apod_sqr(w1, 0.35, L_shrink, fab_var);
77             [bw_sqr(i), wlc_sqr(i)] = fwhm(w1, Rsqr);

```

```
75
76         filename = [dirname '/Dw_' num2str(Dw*1e9) '_' MODE '-' ...
77             neff_width_files{film_thickness} '_DC' ...
78             num2str(DC) '.mat'];
79         save(filename, ...
80             'wl', 'Rsin', 'Tsin', 'Dw', ...
81             'MODE', 'film_thickness');
82     end
83
84     filename = [dirname '/BW_wlc-' MODE '-' ...
85         neff_width_files{film_thickness} '_DC' ...
86         num2str(DC) '.mat'];
87     save(filename, ...
88         'Dws', 'bw_sin', 'wlc_sin');
89     toc;
90     end
91     end
92 end
93
94 %% Square grating profile
95 % Simulates the BGs considering:
96 % * Squared profile
97 % * Apodization: gaussian profile with parameter sigma
98 % * Longitudinal shrink: L_shrink being the amount of longitudinal
99 % shrinkage from the Bragg period bg_p
100
101 function [Ra, Ta] = apod_sqr(wl, sigma, L_shrink, n_fab_var)
102 global bg_p n_p neff Delta_n
103 l = bg_p/2;
104 x = ((0:n_p) - n_p/2)/n_p*2;
```

```

105 % Apodization profile as function of position x, n_array
106 n_array = exp(-x.^2/(2*sigma^2));
107 % normalization to make max = Delta_n
108 n_array = n_array/max(n_array)*Delta_n/2;
109
110 nL = neff - n_array + n_fab_var(1)*randn(size(x));
111 nH = neff + n_array + n_fab_var(1)*randn(size(x));
112 TF = repmat(eye(2),1,1,length(wl));
113
114 for i = 1:length(n_array) % sweeps the grating considering apodization
115     for j = 1:length(wl)
116         T_hw1 = homoWG_matrix(wl(j), l - L_shrink + ...
117             n_fab_var(2)*randn(1,1), nL(i), 0);
118         T_is12 = IndexStep_Matrix(nL(i), nH(i));
119         T_hw2 = homoWG_matrix(wl(j), l + L_shrink + ...
120             n_fab_var(2)*randn(1,1), nH(i), 0);
121         T_is21 = IndexStep_Matrix(nH(i), nL(i));
122         Tp = T_hw1*T_is12*T_hw2*T_is21;
123         TF(:, :, j) = TF(:, :, j) * Tp(:, :);
124     end
125 end
126
127 Ra = zeros(1, length(wl));
128 Ta = zeros(1, length(wl));
129
130 for i = 1:length(wl)
131     Ra = squeeze(abs(conj(TF(2,1,:)) .* TF(2,1,:)) ./ ...
132         conj(TF(1,1,:)) ./ TF(1,1,:));
133     Ta = squeeze(abs(1./(conj(TF(1,1,:)) .* TF(1,1,:))));
134 end
135 end

```

```
133
134 function T_hw = homoWG_matrix(wavelength, l, neff, loss)
135 % Calculate the transfer matrix of a homogenous waveguide
136
137 % Grating_parameters;
138 beta = 2*pi*neff/wavelength - li*loss/2; % Complex propagation constant
139 v = [exp(li*beta*l), exp(-li*beta*l)];
140 T_hw = diag(v);
141 end
142
143 function T_is = IndexStep_Matrix(n1, n2)
144 % Calculate the transfer matrix for an index step from n1 to n2
145 a = (n1+n2)/(2*sqrt(n1*n2));
146 b = (n1-n2)/(2*sqrt(n1*n2));
147 T_is = [a b; b a];
148 end
149
150 %% Sinusoidal grating profile
151 % Simulates the BGs considering:
152 % * Sinusoidal profile
153 % * Apodization: gaussian profile with parameter sigma
154 % * Longitudinal shrink: L_shrink being the amount of longitudinal
155 % shrinkage from the Bragg period bg_p
156
157 function [Ra, Ta] = apodized_sin(n_p, sigma, L_shrink, n_fab_var)
158 global wl Delta_n neff
159
160 x = ((0:n_p) - n_p/2)/n_p*2;
161 % Apodization profile as function of position x, n_array
162 n_array = exp(-x.^2/(2*sigma^2));
```

```

163 % normalization to make max = Delta_n
164 n_array = n_array/max(n_array)*Delta_n/2;
165
166 nL = neff - n_array + n_fab_var(1)*randn(size(x));
167 nH = neff + n_array + n_fab_var(1)*randn(size(x));
168
169 % TF is the 2x2 transfer matrix, one for each wavelenth point
170 TF = repmat(eye(2),1,1,length(wl));
171
172 for i = 1:length(n_array) % sweeps the grating considering apodization
173     TFt = bg_tf_sin(1, nL(i), nH(i), L_shrink + n_fab_var(2)*randn(1,1));
174     for j = 1:length(wl) % sweeps wavelength
175         TF(:, :, j) = TF(:, :, j) * TFt(:, :, j);
176     end
177     Ra = squeeze(abs(conj(TF(2,1,:)) .* TF(2,1,:) ./ ...
178         conj(TF(1,1,:)) ./ TF(1,1,:)));
179     Ta = squeeze(abs(1./(conj(TF(1,1,:)).*TF(1,1,:))));
180 end
181
182 % Computes the 2x2 transfer matrix for a sinusoidal profile Bragg grating
183 % Inputs are, respectively, number of periods, lowest neff and highest neff
184 % For equatinos, see sinusoidal_grating.pdf
185
186 function TFp = bg_tf_sin(n_p, nL, nH, L_shrink)
187 global bg_p wl
188 Lsin = bg_p*n_p - L_shrink;
189 n0 = (nH + nL)/2;
190 n1 = (nH - nL)/2;
191 Omega = -pi;
192 beta = (2*pi./wl)*n0;

```

```
193 beta0 = pi/(bg_p - L_shrink);
194 Δ = beta - beta0;
195 kappa = pi*n1./wl;
196 gamma = sqrt((-1i*Δ).^2 + kappa.^2);
197
198 F11 = (cosh(gamma.*Lsin) + 1i*Δ./gamma .*...
199     sinh(gamma.*Lsin)).*exp(1i*beta0*Lsin);
200 F12 = 1i*kappa./gamma.*sinh(gamma*Lsin).*exp(-1i*(beta0*Lsin+Omega));
201 F21 = -1i*kappa./gamma.*sinh(gamma*Lsin).*exp(1i*(beta0*Lsin+Omega));
202 F22 = (cosh(gamma*Lsin) - 1i*Δ./gamma .* ...
203     sinh(gamma*Lsin)).*exp(-1i*beta0*Lsin);
204
205 TF = zeros(2, 2, length(F11));
206 TFhw = zeros(2,2, length(F11));
207 TFp = zeros(2, 2, length(F11));
208
209 TF(1,1,:) = F11; TF(1,2,:) = F12; TF(2,1,:) = F21; TF(2,2,:) = F22;
210
211 TFhw(1,1,:) = exp(1i*beta*L_shrink);
212 TFhw(2,2,:) = exp(-1i*beta*L_shrink);
213
214 for i = 1:length(TF(1,1,:))
215     TFp(:, :, i) = TF(:, :, i) * TFhw(:, :, i);
216 end
```